INAUGURAL - DISSERTATION

zur Erlangung der Doktorwürde der

Naturwissenschaftlich-Mathematischen

Gesamtfakultät der

Ruprecht-Karls-Universität

Heidelberg

Vorgelegt von

M.Sc. Chong Yang

aus Shandong, China

Datum der mündlichen Prüfung: 29. Juni 2017

Quantum Chemical Study of Coupled Molecular Photoswitches

Supervisors: Prof. Dr. Andreas Dreuw

PD Dr. Markus Pernpointner

To my family

Contents

Preface

"A journey of a thousand miles begins with a single step"

- Laozi

Abstract

Ab initio quantum chemical methods are useful tools and widely employed for the study of excited states, which are the central quantities in photochemistry. A robust understanding of photochemical processes following electronic excitation of molecules does not only allow for the characterization of the physical and chemical properties, but also offers a solid foundation for the successful design and development of novel light-responsive molecular devices. In light of the importance of excited states in photochemical processes, appropriate quantum chemical methods for a reliable and accurate description of the electronic structure need to be chosen carefully. In practical calculations, density functional theory (DFT) and time-dependent DFT (TDDFT) can provide a good compromise between accuracy and computational effort for the treatment of ground and excited states. The algebraic diagrammatic construction (ADC) scheme for the polarization propagator, which is known to deliver accurate excited states information, is often used to benchmark TDDFT results. The basic background of quantum chemistry and several popular quantum chemical methods for the study of excited states are introduced in chapter 2. To obtain insights into novel multiphotochromic properties and the unique isomerization behavior of multiple azobenzenes, a series of linear- and non-linear multiazobenzenes are investigated with selected quantum chemical methods in chapter 3 and chapter 4. Moreover, an evaluation of the restricted-virtual-space (RVS) approximation within the algebraic diagrammatic construction (ADC) scheme for the polarization propagator for the purpose of speeding up excited state calculations of medium-sized and large molecular systems is presented in chapter 5.

In more detail, chapter 3 presents investigations of the absorption spectra and the isomerization mechanism of the parent azobenzene (AB) and linear coupled azobenzenes ((AB-(n)). The relaxed potential energy surfaces along the CNNC rotation, CNN inversion and the concerted-inversion pathways were calculated with TDDFT to explore the isomerization mechanism of linear multiazobenzenes. The results show that the order of electronically excited states changes with increasing chain length because the excitation energies of the low-lying excited states display different levels of decline.

A significant dual band appears in the π-π* absorption band of *cis*-AB-(n)s due to strong excitonic coupling between two connected sub-azo moieties. The S_1 potential energy surface of AB and the linear AB-(n)s is essentially barrierless along the rotation pathway and a conical intersection is most likely to appear in all cases of the AB-(n). Thus, it is concluded that the isomerization in the n-π* state favours the rotation mechanism. Although a large barrier was found in the S_1 potential surface along the concerted-inversion pathway, the concerted-inversion path is considered to be an energetically favorable mechanism when excitation to the S_2 state or even higher excited states occurs. Because the energy gap between the S_2 and S_1 states becomes quite small, rapid relaxation from higher excited states to the S_1 state occurs more easily, which is beneficial to overcome the potential energy barrier on the S_1 surface.

In the subsequent chapter 4, several non-linear azobenzene systems consisting of two or three azo subunits are studied. The absorption spectra of *o-, m-* and *p*-bisazobenzenes were primarily calculated using time-dependent density functional theory together with and without conductor-like polarizable continuum models (C-PCM) modelling solvation. The results show that intramolecular excitonic interaction between the azo subunits occurs in the case of the *o*-bisazobenzenes, which accounts for the two significant excitonic bands in the absorption spectrum. Strong π-conjugation extending over the two azo subunits was observed for *p*-bisazobenzene, leading to planarity of the molecule as well as low quantum yield for switching. In contrast, *m*-bisazobenzene exhibits a very similar spectral feature compared to the monomeric azobenzene and the azo subunits operate nearly independently from each other. The following investigation of *meta-tris*-azobenzene (MTA) is based on the intriguing *meta-* connection pattern. TDDFT simulations fully characterize spectral differences in the absorption spectra of MTA and various substituted MTA derivatives. It is found that the distribution of the main π-π* band of MTA is also quite similar to the monomer azobenzene, only differing in intensity, which reveals decoupling of the three sub-azo units. The auxochromic shift in the absorption spectrum can be modulated by a series of introduced functional groups. This study shows that each individual sub-azo unit of substituted MTA can be selectively and reversibly switched by specific wavelengths of light. In addition, the photophysical and photochemical properties of cyclotrisazobenzene (CTA), which shows a high stability due to its constrained ring

system, were addressed. The PES along the isomerization pathway of the azobenzene units in CTA show that isomerization is essentially impossible even though the CTA molecule is excited to higher excited states. It indicates that relaxation of excited CTA does not lead to photoisomerization. This study can be extended to relevant CTA derivatives, thereby probably revealing unexpected multiphotochromic behavior. Overall, quantum chemical investigations of coupled multiazobenzenes not only provide deeper insight into multiphotochromic properties and theirs unique isomerization behavior, but also pave the way for the design and development of novel photoresponsive applications, based on azo subunits, with different connection patterns.

In Chapter 5, the applicability and limitations of the restricted virtual space (RVS) approximation for use within the algebraic diagrammatic construction (ADC) scheme for the polarization propagator up to third order is evaluated. In RVS-ADC, not only the core but also a substantial amount of energetically high-lying virtual orbitals is disgarded in excitation energy calculations of low-lying excited states. RVS-ADC calculations are performed for octatetraene, indole, and pyridine using different standard basis sets of triple-zeta quality, i.e. 6-311G*, cc-pVTZ and def2-TZVP. The results show that freezing core and less than 30% percent of the high-lying virtual orbitals has a negligible effect on ππ* excited states within RVS-ADC(2). However, for nπ* or $\pi\sigma^*$ states, the RVS approximation is generally less reliable, whereas its accuracy is greatly improved by using the third-order ADC level. Furthermore, a unified and basis-set independent normalized virtual orbital threshold (NVT) is introduced, making the RVS approximation controllable and applicable.

Zusammenfassung

Ab-initio quantenchemische Methoden sind nützliche Werkzeuge und weit verbreitet für die Untersuchung von angeregten Zuständen, die das zentrale Thema in der Photochemie sind. Ein grundlegendes Verständnis der photochemischen Prozesse nach elektronischer Anregung von Molekülen erlaubt nicht nur die Charakterisierung der physikalischen und chemischen Eigenschaften, sondern bietet auch eine solide Grundlage für ein erfolgreiches Design und die Entwicklung neuartiger lichtempfindlicher molekularer Werkzeuge. Angesichts der Bedeutung der angeregten Zustände in photochemischen Prozessen müssen entsprechende quantenchemische Methoden zur zuverlässigen und genauen Beschreibung der elektronischen Struktur sorgfältig gewählt werden. In praktischen Berechnungen können die Dichtefunktionaltheorie (DFT) und die zeitabhängige DFT (TDDFT) einen guten Kompromiss zwischen Genauigkeit und Rechenaufwand für die Behandlung des Grundzustands und der angeregten Zustände liefern. Das vielversprechende algebraisch-diagrammatische Konstruktionsschema (ADC) für den Polarisationspropagator, von dem bekannt ist, dass es genaue angeregte Zustandsinformationen liefert, kann verwendet werden, um TDDFT-Ergebnisse zu verifizieren. Die Grundlagen der Quantenchemie sowie mehrere populäre quantenchemische Methoden für das Studium angeregter Zustände werden in Kapitel 2 vorgestellt. Um Einblicke in neuartige multiphotochrome Eigenschaften und das einzigartige Isomerisierungsverhalten von gekoppelten Azobenzolen zu erhalten, wird eine Reihe von linearen und nichtlinearen Multiazobenzolen mit den ausgewählten quantenchemischen Methoden in Kapitel 3 und Kapitel 4 untersucht. Darüber hinaus wird eine Auswertung der "restricted virtual space" (RVS) Näherung im algebraisch-diagrammatischen Konstruktionsschema (ADC) für den Polarisationspropagator zur kostengünstigeren Berechnung von angeregten Zustands mittelgroßer und großer molekularer Systeme in Kapitel 5 vorgestellt.

In Kapitel 3 werden Untersuchungen der Absorptionsspektren und des Isomerisierungsmechanismus des Azobenzols (AB) und linear gekoppelter Azobenzole (AB-(n)) vorgestellt. Die relaxierten Potentialhyperflächen entlang der CNNC-Rotation, der CNN-Inversion und die konzertierten Inversions-Reaktionspfade wurden auf der

Basis von TDDFT berechnet, um den Isomerisierungsmechanismus von linearen Multiazobenzolen zu erforschen. Die Ergebnisse zeigen, dass sich die Reihenfolge der elektronisch angeregten Zustände mit zunehmender Kettenlänge ändert und gleichzeitig die Anregungsenergien der tief liegenden angeregten Zustände unterschiedliche Absenkungsgrade aufweisen. Eine signifikante duale Bande erscheint in der π-π* Absorptionsbande von *cis*-AB-(n) aufgrund starker exzitonischer Kopplung des zwei verbundenen Azo-Subgruppen. Die S_1-Potentialfläche des AB und der linearen AB-(n) ist im wesentlichen barrierefrei entlang des Rotationsweges und eine konische Durchschneidung ist höchstwahrscheinlich in allen Fällen zu erwarten. Daraus kann geschlossen werden, dass die Isomerisierung im n-π* Zustand den Rotationsmechanismus begünstigt. Obwohl eine große Barriere auf der S_1-Potentialfläche entlang des konzertierten Inversions-Reaktionspfades gefunden wurde, wird der konzertierte Inversionsweg als ein energetisch günstiger Mechanismus betrachtet, wenn die Anregung in den S_2-Zustand oder sogar in höhere angeregte Zustände erfolgt. Da die Energielücke zwischen den S_2- und S_1-Zuständen recht klein wird, läuft die rasche Relaxation von den höheren angeregten Zuständen in den S_1-Zustand leichter ab, was vorteilhaft ist, um die Potentialbarriere auf der S_1-Potentialfläche zu überwinden.

Im folgenden Kapitel 4 wurden mehrere nichtlineare Azobenzolsysteme aus zwei oder drei Azo-Subeinheiten untersucht. Die Absorptionsspektren von *o*-, *m*- und *p*-Bisazobenzolen wurden primär mit zeitabhängiger Dichtefunktionaltheorie zusammen mit (in Lösungsmittel) und ohne (in der Gasphase) polarisierbares Kontinuumsmodell (C-PCM) berechnet. Die Ergebnisse zeigen, dass eine intramolekulare exzitonische Wechselwirkung zwischen den Azo-Subeinheiten im Falle der *o*-Bisazobenzole auftritt, was die beiden signifikanten exzitonischen Banden im Absorptionsspektrum erklärt. Starke π-Konjugation, die sich über die beiden Azo-Subeinheiten erstreckt, wurde für p-Bisazobenzol beobachtet, was zu einem planaren Molekül sowie einer niedrigen Quantenausbeute führte. Im Gegensatz dazu weist *m*-Bisazobenzol ein sehr ähnliches Absorptionsspektrum im Vergleich zum monomeren Azobenzol auf und jede der Azo-Subeinheiten ist nahezu unabhängig von den anderen. Die folgende Untersuchung des *m-tris*-azobenzols (MTA) basiert auf dem Meta-Verbindungsmuster. TDDFT Simulationen charakterisierten hierbei die spektralen Unterschiede in den

Absorptionsspektren für MTA und verschiedene substituierte MTA-Derivate. Es wurde festgestellt, dass die Verteilung der Haupt-π-π*-Bande des MTA sehr der des monomeren-Azobenzol ähnelt und sich nur in der Intensität unterscheidet, was eine Entkopplung von drei Sub-Azo Einheiten belegt. Die auxochrome Verschiebung im Absorptionsspektrum kann durch eine Reihe von eingeführten funktionellen Gruppen moduliert werden. Diese Studie demonstriert, dass jeder einzelne Sub-Azo Schalter des substituierten MTA selektiv und reversibel durch spezifische Wellenlängen des einfallenden Lichts geschaltet werden kann.

Darüber hinaus wurden die photophysikalischen und photochemischen Eigenschaften von Cyclotrisazobenzol (CTA), das aufgrund des gespannten Ringsystems eine hohe Stabilität gegenüber Isomerisierung aufweist, betrachtet. Die Ergebnisse zeigen, dass eine Isomerisierung der Azobenzol-Einheiten in CTA im Wesentlichen unmöglich ist, auch wenn das CTA Molekül in höhere angeregte Zustände angeregt wird. Es zeigt sich, dass die Relaxation des angeregten CTA nicht zu einer Photoisomerisierung führt. Diese Betrachtungen können auf andere relevante CTA Derivate erweitert werden. Insgesamt ermöglichen quantenchemische Untersuchungen von gekoppelten Multiazobenzolen nicht nur einen tieferen Einblick in die multiphotochromen Eigenschaften und das einzigartige Isomerisierungsverhalten, sondern erlauben auch die Entwicklung neuartiger photoresponsiver Anwendungen auf Basis von Azo-Subeinheiten mit unterschiedlichen Verbindungsmustern.

In Kapitel 5 werden die Anwendbarkeit und die Einschränkungen der "restricted virtual space" (RVS) Näherung für die Verwendung im algebraisch-diagrammatischen schematischen Konstruktionsschema für den Polarisationspropagator bis zur dritten Ordnung ausgewertet. In RVS-ADC werden nicht nur Kernnahe, sondern auch eine beträchtliche Menge an energetisch hoch liegenden virtuellen Orbitalen in den Berechnungen der tiefliegenden angeregten Zustände weggelassen. RVS-ADC Rechnungen werden für Octatetraen, Indol und Pyridin unter Verwendung verschiedener Standardbasissätze von Triple-Zeta Qualität, d.h. 6-311G*, cc-pVTZ und def2-TZVP durchgeführt. Die Ergebnisse zeigen, dass das Einfrieren der Kernorbitale und weniger als 30% der hoch liegenden virtuellen Orbitale eine vernachlässigbare Wirkung auf die ππ* angeregten Zustände innerhalb von RVS-ADC(2) haben. Für nπ*

oder πσ* Zustände ist die RVS-Näherung jedoch im Allgemeinen weniger zuverlässig, wobei die Genauigkeit auf dem ADC Niveau der dritten Ordnung stark verbessert ist. Darüber hinaus wird eine einheitliche und Basissatz unabhängige, normalisierte virtuelle Orbitalschwelle (NVT) eingeführt, wodurch die RVS Näherung genau einstellbar und anwendbar wird.

Chapter 1

Introduction

Azobenzene (AB) is one of the most simple aryl azo compounds composed of two phenyl rings connected via an N=N double bond, which can be reversibly switched between its two stable *trans*- and *cis*-isomers in response to irradiation by light (see Fig. 1.1) [1-6]. The metastable *cis*- isomer can readily undergo *cis*→*trans* isomerization through a thermodynamical relaxation process on a varying time scale ranging from milliseconds to days [7]. The two isomers exhibit quite distinct physical and chemical properties, such as molecular geometry, electric conductance, optical spectra, and electric dipole moment [3]. Due to the intriguing *trans-cis* photoisomerization, AB can be utilized as a light triggered molecular photoswitch for a wide variety of light-controlled organic materials [9-10] and biomolecules [11-14]. Such an outstanding photoisomerization property has been exploited to modulate material properties in many interesting and useful applications, for instance, optical switching molecular devices [3], image storage [6, 15], liquid crystals [6], photoresponsive functional nanomaterials [16], and complex biological systems [12-14]. Specifically, the photoinduced isomerization of azobenzene leads to a substantial geometrical change, where the diameter of the molecule differs from approximately 9 Å in the *trans* form to 5.5 Å in the *cis* form [14, 17]. This light-induced molecular motion is found to be useful for the

design of efficient optomechanical devices [15,18], optical manipulation of biomolecular structures [19], and the photo-orientation of functional materials [9, 20].

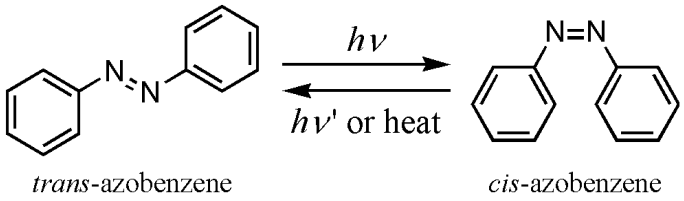

Figure 1.1: Schematic representation of the trans-cis isomerization process of azobenzene.

In addition, as a consequence of the strong conjugated π-system, azo compounds exhibit a variety of vivid colors and thus have been widely used in traditional dye industry [21-22]. So far, azobenzene dyes are still regularly applied to color various materials as dyes [21], pigments [22], and food and drug additives [23], and therefore play a crucial role in the development of modern chemical industry and analytical chemistry.

Since *Hartley* [1] first published a remarkable study of the configurational changes of azobenzene as a result of light irradiation, azobenzene and its derivatives have been extensively investigated experimentally and theoretically for the past 80 years. Due to its outstanding photoisomerization property, it is not surprising that the photoresponsive changes in the absorption spectra are expected to modulate desired optical properties and light-induced functions. In the past few decades, the physicochemical properties and the photoisomerization mechanism of azobenzene have been investigated extensively for the purpose of obtaining new and efficient optical effects for numerous potential applications [5-6, 9, 12]. For azobenzene it is pretty well known that azobenzene is a very good candidate as the photoswitch, however, a clear understanding of the isomerization mechanism is still not available.

The UV-Vis absorption spectrum of *trans*-azobenzene exhibits a strong $\pi \rightarrow \pi^*$ band in the near UV region and a low-intensity $n \rightarrow \pi^*$ band in the visible region [3]. The $\pi \rightarrow \pi^*$ absorption band of the *cis* isomer shifts to shorter wavelengths with a decreased

intensity and the n→π* band shows a significant increase in the intensity due to the allowed n→π* transition. In general, *trans→cis* photo-isomerization of azobenzene occurs after excitation into the first or the second excited state. In the reverse process, *cis*-azobenzene undergoes *cis→trans* photoisomerization when excited to the S_1 or S_2 state or by means of thermal relaxation. Previous investigations [24-34] have proposed three main isomerization mechanisms, i.e. rotation, inversion and concerted-inversion pathways in the nπ* and ππ* states. The rotation pathway refers to an out-of-plane torsion of the N=N double bond with rupture of the π bond. In contrast, the inversion pathway proceeds via two possible mechanisms involving an in-plane inversion of one NNC angle and an in-plane concerted-inversion of two NNC angles.

Many previous experimental and theoretical efforts have been made to gain insights into the isomerization mechanism and the photochromic properties [1-8, 24-36]. For example, *Rau* and *Lüdecke* [2] first proposed two competing photoisomerization pathways when azobenzene derivatives are excited to different excited states. They advocated the inversion mechanism on the basis of the determination of *trans-cis* isomerization quantum yields. *Monti* and co-workers [33] conducted configuration interaction (CI) calculations of potential energy curves of azobenzene along two isomerization pathways and provided a reasonable explanation that the isomerization occurs in the nπ* state via an inversion pathway while the rotation mechanism dominates after excitation to the ππ* state. Furthermore, a novel concerted-inversion channel has been proposed by *Diau* [34]. This new relaxation channel might only be accessible when excited to the S_2 state. *Fujino* and co-workers [24] performed a time-resolved resonance Raman study and concluded that the inversion pathway is allowed in the S_1 state and the rotation mechanism in the S_2 state can be ruled out.

With the development of *ab initio* quantum chemical methods [37-49], more and more recent calculations demonstrated that the rotation mechanism is preferred, since there is no energy barrier along the rotation pathway in the nπ* state [29, 32, 50-51]. *Inshikawa et al.* [29] performed complete active space self-consistent field (CASSCF) calculations for the two dimensional potential energy surfaces. They concluded that the isomerization of azobenzene most likely proceeds through the rotation pathway due to

the presence of a conical intersection between the ground and S_1 state. *Crecca* and co-workers [32] calculated the potential energy surfaces of azobenzene and its derivatives using time dependent density functional theory (TDDFT) [37, 48-49] and found that the rotation pathway is favorable regardless of the excitation wavelength. These isomerization mechanisms have been asserted by the following theoretical calculations and experiments as well [52-54]. In addition to the aforementioned isomerization mechanisms, a two step isomerization mechanism has emerged recently to interpret the photoisomerization process of azobenzene [55], especially in the condensed phase. *Tan et al.* [55] found that the photoisomerization proceeds along an inversion-assisted torsional pathway with a small barrier. Overall, most previous studies indicate that the isomerization of azobenzene and its derivatives in the S_1 state ($n\pi^*$) is mainly dominated by the rotation mechanism while in the S_2 state ($\pi\pi^*$) azobenzene most likely undergoes the inversion or the concerted inversion transformation. However, which isomerization mechanism dominates after being excited to different excited states has been the topic of a long-standing debate.

Currently, most interest in azo compounds has moved toward multiple azobenzenes containing two or even more sub-azo units [56-61]. This is because these mutiple azobenzene systems present unexpected photoresponsive multiphotochromic properties and unique isomerization behaviors, leading to many new photo-induced functions for macromolecular systems [62] and photoresponsive nanomaterials [63]. Thus, investigations of coupled azobenzene systems not only gain valuable insight into the physicochemical properties of multiazobenzenes but also pave the way for the incorporation of multiazobenzenes into polymers or supramolecular systems [64-66], and advanced photocontrolled materials [67-69]. Although a large amount of studies on the monomeric azobenzene have been published so far, only a few involving the connection pattern, photochemical properties, and intramolecular interaction of simple bisazobenzenes have been reported in the literature [57-61]. The intramolecular interactions between the sub-azo units is generally considered to play an important role in optical properties and the isomerization process of the multiazobenzenes due to different substitution patterns, and thus produce new multichromic properties. An

example are linear bisazobenzenes, which feature a highly conjugated π-system leading to a substantial red-shift and a much lower photoreactivity [57-58]. In particular, for some bisazobenzenes with specific connection patterns, the photoswitching efficiency can be enhanced roughly in proportion to the number of repeated sub-azo units [58-60]. Thus, such substitution patterns of bisazobenzenes are a key factor in their multiphotochromic properties. These striking differences in absorption spectra and the photoreactivity are clearly seen in different types of bisazobenzenes.

Previous experiments and quantum chemical calculations have addressed special photochemical properties and isomerization features of bisazobenzene compounds. In early 2004, *Cisnetti et al.* [60] investigated the photophysical and photochemical properties of the *meta*- and *para*-bisazobenzene derivatives. It has been shown that *m*-bisazobenzene behaves quite similarly to the parent azobenzene and *p*-bisazobenzene shows a red-shift in the π-π* absorption band as well as a reduced efficiency for *trans–cis* isomerization. Studies using the surface hopping molecular dynamics approach show a similar behavior for *m*-bisazobenzene and *p*-bisazobenzene [57]. The switching behavior and the thermochromic characteristics of the four *p*-bisazobenzene derivatives connected via an N=N linker between two azo moieties have been addressed to optimize the photoswitching efficiency of linear multiazobenzenes [58]. Also, it was found that the absorption spectra of *o*-azobenzenes are significantly affected by the substituents. Interestingly, *trans-cis* isomerization was not observed in the case of the *o-bis*, *o-tris*-, and *o-tetra*-azobenzenes. This behaviour of *o*-bisazobenzene was confimed by analysis of the ultrafast dynamics of *o-, m-* and *p*-bisazobenzenes reported by *Chavdar et al.* [59]. The authors found evidence that the photochromic properties and the quantum yields for photoswitching are closely related to the connectivity pattern of *bis*-azobenzene. Besides, other types of multiazobenzenes such as multiazobenzene dimers, cyclotrisazobenzene, multiazobenzenes on a metal surface, and coulped azobenzene oligomers have been studied and documented in the literature [70-78].

The multiphotochromic nature and photoisomerization behavior of coupled azobenzenes are still attracting a lot of attention. A thorough understanding of the physicochemical properties and the photoisomerization process of multiazobenzene is of fundamental

importance to modulate the properties of polymers, biomolecules and photoresponsive materials as mentioned above. However, current studies of the switching behavior and multiphotochromic properties were insufficient for a successful design of various invaluable photocontrollable molecular devices, especially macromolecular crystals [79], and photo-responsive functional materials [80-83].

As is well known, several low-lying electronically excited states of azobenzene play a critical role in the photoisomerization process accompanied by changes in the geometries and physicochemical properties. As a consequence of the complicated interaction caused by the external enviromental factors, such as solvent effects, temperature, pressure, and irradiation wavelength, accurate electronic structure descriptions are not likely to be easily achieved via experimental methods. In contrast, quantum chemical calculations are able to provide accurate and detailed description of low-lying electronically excited states. For most photochemical problems, electronic structure methods [37, 42, 48-49, 84-94] are considered as effective tools in the fields of theoretical and computational chemistry. They are widely used to investigate the physical and chemical properties of various molecules and complicated chemical reactions [29, 32-34, 57]. Specifically, a series of available approximate methods, such as the time-dependent density functional theory (TDDFT) [37, 48-49], the coupled cluster with single and double substitutions (CCSD) [38], the second-order approximate coupled-cluster method (CC2) [84], the configuration interaction with singles (doubles correction) (CIS(D)) [85], the algebraic diagrammatic construction scheme for the polarization propagator (ADC) [91-94], can provide fascinating insights into the electronic structure. An alternative for multi-reference problems is provided by many multi-configurational and multi-reference methods, such as the complete active space self-consistent field (CASSCF) method[43-44], the complete active space perturbation theory to second-order (CASPT2) method [45-47], and the multi-reference configuration interaction (MRCI) [89-90] method. Of course, these methods offer a relatively feasible way to solve conical intersection problems. Therefore, advanced electronic structure methods are able to explore physicochemical properties and isomerization mechanism for azobenzene compounds. Many previous theoretical

studies have proposed several possible isomeriazation mechanisms and photochemical properties based on these electronic structure methods [30-34]. However, so far, the isomerization mechanism is still being unraveled and the unique multiphotochromic behaviour of multiple azobenzenes remains to be addressed.

In this project, the main purpose is to investigate the isomerization behaviour and the multiphotochromic properties of coupled azobenzenes to guide a successful design for efficient and highly multifunctional photoswitches. Initially, this work is concerned with the influence of chain length on the vertical excitation energies as well as the isomerization mechanism of azobenzene with increasing chain length. The excitonic coupling between two moieties of linear coupled azobenzenes will be exploited to reveal the complexity of photoreactivity with varied chain length. The following work will illustrate photochromic properties of *o-, m-* and *p*-bisazobenzenes in the gas phase and in solvent using the time-dependent density functional theory with and without conductor-like polarizable continuum model (C-PCM) [95-97]. To unravel the coupling interaction between two different sub-azo units, it is thus highly desirable to fully characterize the features of the electronic absorption spectra of different types of bisazobenzenes. Similarly, the spectral features of the absorption spectrum of *m*-trisazobenzene shall be presented to discuss decoupling of individual azo subunits. Introducing various functional groups for *m*-trisazobenzene leads to an efficient separation of the main $\pi\pi^*$ absorption band. Thus, a series of substituted *m*-trisazobenzenes are expected so that each of the azo subunits can be selectively switched by different wavelengths of light. The potential energy curves of *m*-trisazobenzene will be calculated to interpret the unexpected isomerization behaviour of coupled azobenzenes.

In addition, to extensively compute excited states of multiazobenzens, an efficient restricted virtual space (RVS) approximation for ADC excitation energy calculations will be addressed to speed-up excited state calculations of large molecules.

In light of the importance of low-lying excited states in photochemistry, it is necessary to employ an appropriate approach to calculate electronically excited states. The

accurate calculation of vertical excitation energies, potential energy surfaces and molecular orbitals can be used to investigate and deliver reliable physicochemical properties of molecules as well as the photo-isomerization mechanism. Some of the above-mentioned computational methods are very well suited to study ground and low-lying excited states chemistry, while other single-reference methods [37-38] cannot provide satisfactory results for strongly distorted molecular geometries and conical intersections. However, many previous excited state calculations have been performed and still provided valuable insights into the excited state properties and the isomerization process for plenty of organic molecules. Thus, in Chapter 2, I present a brief overview of quantum chemical methods and a detailed description for the selected quantum chemical methods for studies of multiazobenzenes. Mainly, time-dependent density functional theory is applied to the following excited state calculations benchmarked with the algebraic diagrammatic construction scheme for the polarization propagator method, and thus both methods will be described in detail.

Chapter 3 focuses on the influence of the chain length on the vertical excitation energy of linear coupled azobenzenes as well as their isomerization mechanism. At the preliminary stage, the geometries and excitation energies of *trans*-AB have been calculated using different electronic structure methods ranging from configuration interaction singles (CIS) [98] to highly accurate ADC methods. It has been previously proposed that the lowest two excited states play an important role in the isomerization process of azobenzene. However, it is still unclear what the role of each low-lying excited state in the isomerization process is. Here, the two lowest excited states of linear azobenzenes were calculated with several above-mentioned *ab initio* methods, for example, TDDFT and ADC. As expected, the lowest vertical excitation energy decreases strongly with an increase in chain length. The potential energy curves along the CNNC rotation, CNN inversion and the concerted-inversion CNN inversion pathways for different lengths of linear azobenzenes have been calculated. Different twisted positions of linear azobenzene have been taken into account as well. Calculations of potential energy surfaces of linear azobenzenes will not only provide insights into the isomerization process of azobenzene but also yield a fundamental

understanding of the impact of chain length on the isomerization mechanism.

In the subsequent Chapter 4, several non-linear multiazobenzenes will be presented. The absorption spectra for AB in *trans* and *cis*-isomerization states, as well as for different types of *bis*-azobenzenes in *E,E*- and *E,Z*-isomerization states were calculated in the gas phase and in solvent. Two possible isomers for each *o-, m-*, and *p*-bisazobenzene were considered. A clear dual band in the absorption spectra was only observed in the case of *o*-bisazobenzene, which was attributed to potential intramolecular excitonic interaction between the two individual azo subunits. Interestingly, *meta*-bisazobenzene displays very similar spectral properties compared to paprent azobenzene. Such a *m*-substitution pattern in bisazobenzene allows two azo subunits to operate independently from each other, implying their decoupling. Upon this fascinating feature of *meta*-substitution pattern, a *tris*-azobenzene comprising three azobenzene units connected via a shared phenyl ring was designed. Similarly, the absorption spectra of *m*-trisazobenzene and its various derivatives were calculated. This calculation shed light on the spectral shifts with respect to different substitutional groups for the purpose of achieving efficient separation of the absorption bands with respect to different azo subunits. Substituted *m*-trisazobenzenes are believed to be multifunctional photoswitches each azo subunit of which can be switched selectively by a specific wavelength of light. Furthermore, the inertness of *trans-cis* isomerization of a typical macrocycle, cyclotrisazobenzene (CTA), which has a highly conjugated π-system, has attracted considerable interest in the past few years. At the end of this Chapter, the unique multiphotochromic behavior and properties of cyclotrisazobenzene will be described.

In Chapter 5, existing approaches such as the truncation or optimization of the molecular orbital space for coupled cluster theory are introduced. The algebraic diagrammatic construction (ADC) scheme for the polarization propagator is an accurate computational method for the treatment of excited states. However, a good compromise between accuracy and computational effort with ADC for the description of excited states of medium-sized and large molecular systems is highly challenging. Here, I report the restricted virtual space (RVS) approximation for the ADC scheme to speed up

excited state calculations without significant loss in accuracy of excitation energies and other optical properties. The RVS-ADC approximation can offer sufficient *ab initio* computational information of excited states, with high-quality calculations of excited states of an extensive range of large molecules as well as substantial computational savings.

Chapter 6 summarizes all results of the presented work. The current challenges of studies of coupled azobenzenes are presented and an outlook on further research in the fields of quantum chemical methods is given as well.

Chapter 2

Theoretical Methodology

This chapter summarizes the fundamental concepts and the popular approaches of quantum and computational chemistry [100-102]. This theoretical background will be the basis for the study of photochemical phenomena, properties and reaction processes. It is well-known when a molecule undergoes photoexcitation into an electronically excited state, it leads to unique photochemical effects and subsequent changes of physical and chemical properties. Thus, the investigation of electronically excited states is critical for the interpretation of photochemical phenomena and reactions in photochemistry. In general, the two main classes of quantum chemical methods are wavefunction based methods [38, 43-44, 89-90, 91-94, 102-105] and density based methods [37, 48-49, 106-111]. To elucidate the evolution of two types of electronic structure methods, two representative quantum chemical methods, i.e. time-dependent Denstiy Functional Theory (TDDFT) [37, 48] and the algebraic-diagrammatic construction (ADC) scheme for the polarization propagator [40-42], will be addressed in detail.

For the purpose of a disscussion of these quantum chemical methods, some essential concepts, such as the molecular *Schrödinger* equation [112], the *Born-Oppenheimer* approximation [113] and the concept of second quantization [102] need to be introduced at first in chapter 2.1. As another prerequisite for the calculation of excited states, the Hartree-Fock method (HF) [102] is described in chapter 2.2. A short overview of some

quantum chemical approaches for the description of the electronic ground and excited states, such as Møller-Plesset perturbation theory (MP) [114], the configuration interaction (CI) method [104-105], and the coupled-cluster (CC) approach [115] is provided in chapter 2.3. A detailed overview of these approaches is beyond the scope of this thesis and can be found in literature [104-105, 114-115]. Here, special focus shall be laid on the discussion of the excited state approaches which are used in chapters 3-5. Thus, a comprehensive derivation of density functional theory (DFT), time-dependent DFT [37, 48] and the algebraic-diagrammatic construction (ADC) [40-42, 91-94] scheme for the polarization propagator are described in chapter 2.4 and 2.5, respectively. Moreover, a general discussion of the conductor-like polarizable continuum model [95-97] which is applied in the calculation of excited states of solvated molecules, is given in chapter 2.6.

2.1 Basic concepts of quantum chemistry

2.1.1 The Schrödinger equation

I start with the heart of quantum chemistry, which is given by the molecular *Schrödinger* equation [112]. This equation is essential to describe the quantum mechanical behavior of a physical system. In particular, the time-dependent *Schrödinger* equation is a partial differential equation that describes how the wavefunction of a physical system changes with time *t*. It has the form

$$i\hbar\frac{\partial}{\partial t}\Psi(r,t)=\hat{H}\Psi(r,t) \tag{2.1}$$

where $\Psi(r, t)$ is the time-dependent wavefunction, which describes the quantum state of the system. $\hat{H}$ is the Hamilton operator, which describes how the system evolves with time. The Hamiltonian is given by

$$\hat{H}(r,t)=\frac{-\hbar^2}{2m}\nabla^2+V(r,t) \tag{2.2}$$

where *m* represents the "reduced mass" of all particles in a system and *V* represents the potential energy of the system.

The solution of the time-dependent *Schrödinger* equation for the ground state yields the energy of the physical system. However, for many systems, the potential energy of the system is generally considered to be independent of the time *t*. In this case, the equation can be separated into two parts: the time-dependent part and the space-dependent part. Thus, the wavefunction is written as

$$\Psi(r,t)=\psi(r)T(t) \tag{2.3}$$

Substituting this expression of the wavefunction into the time-dependent *Schrödinger* equation (2.1) gives rise to following form

$$i\hbar\frac{\partial}{\partial t}\Psi(r,t)=i\hbar*\psi(r)*T(t)*(\frac{-iE}{\hbar})=E\,\psi(r)T(t) \tag{2.4}$$

where *E* is the energy of the system. Then, the time-dependent part should be equal to a constant. Subsequently, the time-dependent *Schrödinger* equation can be divided into two separate equations:

$$[-\frac{\hbar^2}{2m}\nabla+V(r)]\psi(r)=E\,\psi(r) \tag{2.5a}$$

$$T(t)=\mathrm{e}^{-\frac{iEt}{\hbar}} \tag{2.5b}$$

Equation (2.5a) represents the spatial dependence of the wavefunction, which has the standard form of a wavefunction equation with respect to the *Schrödinger* equation. If the potential energy *V(r)* of a system does not change with time *t*, the eqution is called the time-independent *Schrödinger* equation. Therefore, when the energy *E* of the system remains constant, the equation can be used for the description of a stationary state of the system. One can also write the time-independent *Schrödinger* equation as

$$\hat{H}\Psi(r,R)=E\Psi(r,R) \tag{2.6}$$

Indeed, the wavefunction *Ψ(r, R)* is very complex and depends on numerous variables, such as the electronic and nuclear coordinates. The Hamilton operator acts on all these variables, giving rise to a multidimensional eigenvalue problem. Apparently, an exact solution of the equation (2.6) for a large system cannot be obtained due to the many-body interactions of the Hamiltonian. Therefore, it is necessary to invoke various simplifications and approximations to make the solution of the *Schrödinger* equation feasible.

2.1.2 *Born-Oppenheimer* approximation

The *Born-Oppenheimer* approximation is regarded as an assumption that is essential for solving the *Schrödinger* equation. Generally, for practical quantum mechanical calculations, the nuclei can be considered to be fixed since they are much heavier than the electrons and hence the electronic motion must be much faster. Thus, the separation of the motion of the nuclei and the motion of the electrons within the *Born-Oppenheimer* approximation [113] is possible.

Considering a system with N nuclei and n electrons, the total Hamiltonian of the system is given by

$$\hat{H}=\frac{-1}{2}\sum_{i=1}^{n}\nabla_i^2-\frac{1}{2M}\sum_{I=1}^{N}\nabla_I^2+\sum_{i=1}^{n}\sum_{j>i}^{n}\frac{1}{r_i-r_j}+\sum_{I=1}^{N}\sum_{J>I}^{N}\frac{Z_I Z_J}{R_I-R_J}-\sum_{i=1}^{n}\sum_{I=1}^{N}\frac{Z_I}{r_i-R_I} \qquad (2.7)$$

with the nuclear charge Z and the mass of the nuclei M, and the operator $\nabla=\frac{\partial}{\partial r,R}$. R and r represent nuclear and electronic coordinates.

This equation (2.7) can be briefly summed up in the following form

$$\hat{H}=\hat{T}_e+\hat{T}_n+\hat{V}_{ee}+\hat{V}_{nn}+\hat{V}_{ne} \qquad (2.8)$$

$\hat{T}_e,\hat{T}_n,\hat{V}_{ee},\hat{V}_{nn}$, and $\hat{V}_{ne}$ represent the kinetic energy oprators of the electrons and nuclei as well as the interaction potential operators of the electron-electron, electron-nuclei, and nuclei-nuclei terms, respectively.

Therefore, substituting this Hamilton operator into the *Schrödinger* equation, it can be written as

$$[\hat{T}_e+\hat{T}_n+\hat{V}_{ee}+\hat{V}_{nn}+\hat{V}_{ne}]\Psi(r,R)=E\Psi(r,R) \tag{2.9}$$

As discussed above, the electrons are lighter than the nuclei. The electrons can be imagined as moving in an electric field of frozen nuclei. Thus, invoking the *Born-Oppenheimer* approximation, a molecular wavefunction can be written in terms of electronic and nuclear coordinates

$$\Psi(r,R)=\varphi(r,R)\chi(R) \tag{2.10}$$

where $\chi(R)$ represents a nuclear wavefunction and $\varphi(r,R)$ represents an electronic wavefunction, which depends parametrically on the spatial coordinates of the nuclei.

Consequently, the *Born-Oppenheimer* approximation leads to a separation of the *Schrödinger* equation into two individual equations, one for the electrons and one for the nuclei. The corresponding electronic *Schrödinger* equation is of the form:

$$[\hat{T}_e+\hat{V}_{ee}+\hat{V}_{ne}]\psi(r,R)=E_e\psi(r,R) \tag{2.11}$$

The solution of the electronic *Schrödinger* equation gives rise to electronic eigenfunctions $\psi(r,R)$ and eigenvalues E_e, the former of which depend parametrically on the nuclear positions, R.

For the nuclei, an approximate *Schrödinger* equation is written as

$$[\hat{T}_n+\hat{V}_{nn}+E_e]\chi(R)=E\chi(R) \tag{2.12}$$

Moreover, the second and third terms on the left-hand side of equation (2.12) define the potential energy surface (PES) given by

$$V(R)=V_{nn}(R)+E_e(R) \tag{2.13}$$

In practice, one can solve the electronic *Schrödinger* equation using the approximation at a stationary point R for the fixed nuclei to obtain the electronic wavefunctions $\psi(r,R)$ and the associated energies $E_e(R)$. Therefore, collection of all possible nuclear positions yields a multi-dimensional ground-state potential energy surface.

Using the *Born-Oppenheimer* approximation, the problem in quantum chemistry reduces to the accurate treatment of the electron-electron interaction. However, the interaction is still a many-body problem and thus the solution of the electronic *Schrödinger* equation remains a great challenge. Thus, various efficient approximations have been proposed to solve the electronic *Schrödinger* equation.

2.1.3 Second quantization

Second quantization [116-117] is an extremely useful formalism for describing the interacting many-particle system. In the first quantization formulation, observables are usually represented by operators and the states can be expressed in terms of wavefunctions. However, many-particle problems remain a great challenge, such as the treatment of the antisymmetry or symmetry property of wavefunctions due to the indistinguishability of identical particles, fermions or bosons. In this work, since the many-electron problems are main objective, the fundamental concepts for fermion are thus introduced. In second quantization, the wavefunctions are also represented in terms of operators. Therefore, the antisymmetry property of the electronic wavefunction are converted into the algebraic property of certain operators, such as the creation and annihilation operators [118]. In other words, the antisymmetric many-particle states can be simplified as the representation of the set of occupation numbers for each orbital, $|n_1 n_2 \cdots n_\infty>$. Considering a linear vector space, the vectors of occupation numbers with respect to the many-particle state can be found in this space, which is referred to as Fock space. In the Fock space, the vector space of a unique vacuum state is often defined as |0>, which contains no particles. The occupation numbers for the fermionic state only have two possible values of 0 or 1. To meet the requirement of the antisymmetry of the Pauli exclusion principle, all many-electron states must be antisymmetric.

For fermions, two important operators are introduced to act on many-electron states to raise and reduce the number of particles for the system. One is the creation operator defined by the relation

$$c_p^\dagger |n_1 n_2 \cdots n_p, \cdots> = (1-n_p)(-1)^{\sum_{q<p} n_q} |n_1 n_2 \cdots n_N> \tag{2.14}$$

where the creation operator increases the occupation number of many-electron state.

The other is the annihilation operator, which is the Hermitian adjoint to $c^\dagger$

$$c_p |n_1 n_2 \cdots n_p, \cdots> = n_p (-1)^{\sum_{q<p} n_q} |n_1 n_2 \cdots n_N> \tag{2.15}$$

which reduces the occupation number by removing an electron in the respective orbital.

The antisymmetric properties of the creation and the annihilation operators have to satisfy the anticommutation relations

$$\{c_p^\dagger, c_q\} = c_p^\dagger c_q + c_q c_p^\dagger = \delta_{pq} \tag{2.16}$$

$$\{c_p, c_q\} = \{c_p^\dagger, c_q^\dagger\} = 0 \tag{2.17}$$

Here, a fundamental physical question arises, i.e. whether a general one-electron operator in first quantization can be represented in terms of creation and annihilation operators. For example, a one-particle operator is given by

$$O = \sum_{i=1}^{N} o_i \tag{2.18}$$

where o_i only acts on the ith particle.

In the formalism of second quantization, any one-particle operator takes the second quantized form

$$O = \sum_{i=1}^{N} O_{pq} c_p^\dagger c_q \tag{2.19}$$

with $$O_{pq} = <p|h|q> \tag{2.20}$$

Similarly, the two-particle operator such as the Coulomb interaction has the first quantized form

$$V = \frac{1}{2} \sum_{i \neq j}^{N} v(i,j) \tag{2.21}$$

Then, in second quantization, the two-particle operator can be represented by

$$V=\frac{1}{2}\sum_{p,q,r,s} V_{pqrs} c_p^{\dagger} c_q^{\dagger} c_s c_r \tag{2.22}$$

with $$V_{pq}=<pq|v|rs> \tag{2.23}$$

As discussed in the last section, the *Born-Oppenheimer* approximation leads to the separation of the Hamiltonian. Now, it is possible to write the electronic Hamiltonian in terms of creation and annihilation operators in second quantization. It has the following form

$$H=\sum_{p,q} h_{pq} c_p^{\dagger} c_q+\frac{1}{2}\sum_{p,q,r,s} V_{pqrs} c_p^{\dagger} c_q^{\dagger} c_s c_r \tag{2.24}$$

The first term indicates a sum of one-particle operators containing the kinetic energy and the electron-nuclear interaction, while the latter term accounts for the electron-electron interaction. Note that the electronic Hamiltonian does not depend on the number of electrons and thus can be applicable to any many-electron system.

2.2 Hartree-Fock Theory

As shown in the last section, the electronic time-independent *Schrödinger* equation is still very difficult to be solved analytically in the framework of the *Born-Oppenheimer* approximation because of the inherently complicated electron-electron interaction. Regarding the many-body problem, much effort has been made to find an efficient and accurate approximation to deal with the n-electron problem. In general, there are two classes of important electronic structure methods for solving the n-electron *Schrödinger* equation, wavefunction based methods and density based methods. In particular, the Hartree-Fock (HF) theory [102, 119] is one of the fundamental wavefunction based approximate theories for solving the many-body *Schrödinger* equation. The HF approximation does not only provide a way to tackle the many-body problems in quantum mechanics, but also lay a solid foundation for other enhanced approximate

wavefunction methods, so-called *post*-HF methods. I first give a brief introduction of HF theory in this section. A general overview of several typical post-HF methods, i.e, the configuration interaction (CI) theory [104-105], the Møller-Plesset (MP) perturbation theory [114], the coupled-cluster (CC) theory [115] will be presented in the following chapter 2.3. The ADC method, which is also based on *post*-HF approaches, will be presented in chapter 2.4. In addition to wavefunction based methods, the idea of density based methods, such as *Kohn-Sham* density functional theory (DFT) [110-111], will be discussed in chapter 2.5.

The main task of the Hartree-Fock approximation is to obtain the electronic ground state with the lowest energy based on the variational principle [120]. The Hartree-Fock approximation assumes that the ground state wave function of a system with N-electrons can be represented in terms of a set of single-electron wave functions. Let us consider a simple N-electron system with non-interacting electrons. The wavefunction can be witten as a simple Hartree product of spin orbital wavefunctions

$$\Psi_{HP}(r_1, r_2, \ldots, r_N) = \psi_1(r_1)\psi_2(r_2)\cdots\psi_N(r_N) \tag{2.25}$$

However, the Hartree product fails to satisfy the antisymmetry condition of the *Pauli* exclusion principle, which indicates that the wavefunction must be antisymmetric with respect to an interchange of any two electron positions. This is because the electrons are indistinguishable fermions and have up and down spin states. The spin orbitals are considered to be an orthonormal set. Any permutation leads to a change in sign of the wavefunction. Thus, the electronic wavefunction not only depends on the spatial positions but also on the spin coordinates. In other words, the single-electron spin orbitals can be defined by a spin coordinate $\alpha(s)$ or $\beta(s)$ and a spatial coordinate $\varphi(r)$. It has the form:

$$\psi(r) = \begin{Bmatrix} \varphi(r) & \alpha(s) \\ \varphi(r) & \beta(s) \end{Bmatrix} \tag{2.26}$$

To meet the requirement of the antisymmetry principle, a single Slater determinant of N-electron wavefunctions is introduced and given by

$$\Psi(r_1, r_2, \ldots, r_N) = \frac{1}{\sqrt{N!}} \begin{vmatrix} \psi_1(r_1) & \psi_2(r_1) & \cdots & \psi_N(r_1) \\ \psi_1(r_2) & \psi_2(r_2) & \cdots & \psi_N(r_2) \\ \vdots & \vdots & \ddots & \vdots \\ \psi_1(r_N) & \psi_2(r_N) & \cdots & \psi_N(r_N) \end{vmatrix} \tag{2.27}$$

with a normalization factor $1/\sqrt{N!}$. Note that the electrons are indistinguishable fermions. Each electron maps to each orbital in terms of the Slater determinants. Thus, the wavefunction can be obtained from the *N* single-electron functions and is antisymmetric with respect to exchanging any two of the *N* electrons. The Slater determinants satisfy the desired antisymmetry condition and thus provide the best approximation for the description of single-electron wavefunctions with the Hartree-Fock orbitals.

In order to solve the electronic Schrödinger equation, the Hartree-Fock wavefunction can be expressed in the form of a single Slater determinant. Assuming that the wavefunction is normalized, the Hartree-Fock energy has the form

$$E_{HF} = \langle \Psi | H_{el} | \Psi \rangle \tag{2.28}$$

Since the variational theorem is employed, the Hartree-Fock energy is always an upper bound to the exact energy. In order to calculate the expectation value of the Hamiltonian to minimize the Hartree-Fock energy, the best wavefunction approximating the true Ψ can be achieved via varying the parameters within the given orbital space. Therefore, the Hartree-Fock method yields the spin orbitals, which minimize the energy expression for the total energy. In general, the molecular orbital is constructed by combination of a set of given atomic obitals and quantitatively calculated within Hartree-Fock theory. Applying the variational principle, the single-electron wavefunctions are constrained to form an orthonormal and normalized set. For this, we introduce *Lagrange*'s method of undetermined multipliers to execute a constrained optimization [121]. The constraint can be written as the overlap between spin orbitals *i* and *j*,

$$\int \varphi_i^*(r) \varphi_j(r) \, dr = \langle i | j \rangle = \delta_{ij} \tag{2.29}$$

The Hartree-Fock energy E_{HF} with respect to a Slater determinant is given as

$$E_{HF}=\sum_i \langle i|h|j\rangle+\frac{1}{2}\sum_{ij}[ii|jj]-[ij|ji] \tag{2.30}$$

where the core Hamiltonian h describes the motion of one electron in the field of all nuclei and the kinetic energy of the electrons.

Adding the constraint (eq. 2.29), the Lagrange functional is defined as

$$L=E_{HF}-\sum_{ij}\lambda_{ij}(\langle\varphi_i|\varphi_j\rangle-\delta_{ij}) \tag{2.31}$$

and the variational condition is given by

$$\delta L=\delta[E_{HF}-\sum_{ij}\lambda_{ij}(\langle\varphi_i|\varphi_j\rangle-\delta_{ij})]=0 \tag{2.32}$$

Eventually, the Hartree-Fock equations defining the orbitals for the single electrons can be written as

$$f_i\varphi_i(r)=\varepsilon_i\varphi_i(r) \tag{2.33}$$

where ε_i are the Lagrange multipliers associated with the orbital energies, and f_i is the Fock operator defined by

$$f_i=-\frac{1}{2}\nabla_i^2-\sum_{A=1}^{N}\frac{Z_A}{r_A}+\sum_j^M(J_j(i)-K_j(i))=h(i)+v^{HF} \tag{2.34}$$

with

$$h(i)=-\frac{1}{2}\nabla_i^2-\sum_{A=1}^{N}\frac{Z_A}{r_A} \tag{2.35}$$

$$v^{HF}=\sum_j(J_j(i)-K_j(i)) \tag{2.36}$$

where the Fock operator includes a one-electron operator *h(i)* and the two-electron operator v^{HF}, which is called the mean-field potential generally separated into a Coulomb term *J* and an exchange term *K*.

In order to calculate numerical solutions of the Fock equations, the orbitals are expanded in a basis set to transform the Hartree-Fock equation into the Roothaan equation. The orbitals in the Roothaan expansion are given by

$$\varphi_i = \sum_k^N c_{ki}\phi_k \qquad \text{i = 1, 2, . . .,} N \tag{2.37}$$

where N is the number of atomic orbitals used. Substituting the expansion into the Hartree-Fock equation leads to a set of matrix equations for the expansion coefficients

$$f_i \sum_k c_{ki}\phi_k = \varepsilon_i \sum_k c_{ki}\phi_k \tag{2.38}$$

The expansion coefficient c_{ki} is the so-called molecular orbital (MO) coefficient. Thus, the Hartree-Fock eigenvalue problem becomes an explicitly mathematical problem, which can be solved by iterative techniques.

When both sides of the equation (2.38) are multiplied by the conjugate function of the respective basis function ϕ_t and integrated over the electronic coordinates, the equation becomes

$$\sum_k^N c_{ki} \int dr_1 \phi_t^*(r_1) f_i \phi_k(r_1) = \varepsilon_i \sum_k^N c_{ki} \int dr_1 \phi_t^*(r_1)\phi_k(r_1) \tag{2.39}$$

The canonical Hartree-Fock-Roothaan equation can be simplified in matrix form by introducing the matrix element notation

$$\sum_k F_{kt} C_{ki} = \varepsilon_i \sum_k S_{kt} C_{ki} \tag{2.40}$$

or

$$FC = \varepsilon SC \tag{2.41}$$

with two elements of matrices:

$$S_{tk} = \int dr_1 \phi_t^*(r_1)\phi_k(r_1) \tag{2.42}$$

$$F_{tk} = \int dr_1 \phi_t^*(r_1) f_i \phi_k(r_1) \tag{2.43}$$

where ε refers to a diagonal matrix of the orbital energies.

In practical calculations, since explicit electron-electron interactions are ignored, the lowest HF eigenvalue is always higher than the exact ground state energy. The energy difference between them is called correlation energy, with

$$E_{corr} = E_{exact} - E_{HF} \tag{2.44}$$

Hence, to improve the accuracy of the HF energy as far as possible, it is necessary to use appropriate *post*-HF methods to tackle the correlation energy.

2.3 *Post*-Hatree-Fock Methods

2.3.1 Configuration Interaction (CI)

In the Hartree-Fock approximation, the electronic wave function is described by a single Slater determinant and thus the explicit electron-electron interactions are neglected. Due to the electron correlation, the Hartree-Fock limit energy is always higher than the exact energy. In order to tackle the missing electron correlation energy, various post-Hartree-Fock methods have emerged for obtaining the exact solution of the nonrelativistic Schrödinger equation. In particular, configuration interaction (CI) [104-105] is the conceptually simplest *post*-Hartree-Fock method for solving the Schrödinger equation. To better describe the wavefunction, an arbitrary N-electron wavefunction in CI can be represented as a linear combination of all possible N-electron Slater determinants composed of the ground state and the excited state determinants. The excited state determinants are defined as substitutions of the occupied orbitals by virtual orbitals based on the Hartree-Fock "reference" determinant. Thus, in addition to the correlation energy of the ground state, one of the greatest strengths of configuration interaction is to calculate the electronic excitation energies and the excited state properties.

For an N-electron system, the exact ground state wavefunction is expanded in a basis of N-particle basis functions, which are expressed by a linear combination of all N-electron Slater determinants. Each Slater determinant is constructed from a complete set of N spin orbitals, which refers to the electronic configuration or states. This is the reason why this approach is called configuration interaction. Thus, the full CI

wavefunction can be written as

$$\Psi_0 = c_0 \phi_0 + \sum_{ia} c_i^a \phi_i^a + \sum_{i<j, a<b} c_{ij}^{ab} \phi_{ij}^{ab} + \ldots, \tag{2.45}$$

in which the first term is the Hartree-Fock determinant and the second term $\phi^a{}_i$ refers to the single excitation determinant obtained by exciting from the occupied orbital *i* into the virtual orbital *a*. Similarly, $\phi^{ab}{}_{ij}$ refers to a double excitation determinant in which two electrons in two occupied orbitals are excited into virtual orbitals. When all possible Slater determinants are applied in the variational procedure for the numerically exact solutions of the electronic *Schrödinger* equation, this scheme results in FCI [102], which yields a set of eigenvalues and their corresponding eigenstates of the Hamiltonian resulting from the Schrödinger equation. However, a FCI computation is challenging for larger molecules or when a larger basis set is employed. Specifically, the vast number of configurations in the full-CI expansion increases exponentially with the number of electrons and orbitals and leads to a computationally intractable problem for medium-sized molecules.

In practice, the truncation of the CI space expansion is a very common and useful method for obtaining approximate CI wavefunctions and energies, which is used to limit the number of determinants in the CI calculation and thus allows for very rapid calculations. For example, in the common CI singles and doubles (CISD) approximation [122], only those excited determinants which represent single or double excitations relative to the reference state are taken into account. Subsequently, the Hamilton operator contains only one- and two-electron terms and thus only singly and doubly excited configurations are considered for direct interaction with the reference. Thus, the computational cost for a CISD calculation is reduced greatly and CISD recovers about 95% of the correlation energy of small molecules at their equilibrium geometries compared to FCI.

However, most truncated CI approaches are not size-consistent, expect for configuration interaction singles (CIS) [37, 123-124], which only describes singly excited states of the system. In the CI wavefunction expansion, the CIS wavefunction is written as

$$\Psi_{CIS} = \sum_{ia} c_i^a \, \phi_i^a \tag{2.46}$$

where Ψ_{CIS} only contains the "singly-excited" Slater determinants. The CIS excited states do not couple to the ground state due to Brillouin's theorem [102]. Then, the wave function ansatz is substituted into the *Schrödinger* equation and the equation is multiplied from the left with $<\phi^b_j|$, which yields

$$\sum_{ia} <\phi_j^b | H | \phi_i^a> \; c_i^a = E_{CIS} \sum_{ia} c_i^a \, \delta_{ij} \, \delta_{ab} \tag{2.47}$$

Thus, an expression for the excitation energies is given as

$$\omega_{CIS} = E_{CIS} - E_0 \tag{2.48}$$

with

$$\sum_{ia} \{ (\varepsilon_a - \varepsilon_i) \, \delta_{ij} \delta_{ab} + (ia \| jb) \} \, c_i^a = \omega_{CIS} \sum_{ia} c_i^a \, \delta_{ij} \delta_{ab} \tag{2.49a}$$

$$<\phi_j^b | H | \phi_i^a> = (E_0 + \varepsilon_a - \varepsilon_i) \, \delta_{ij} \, \delta_{ab} + (ia \| jb) \tag{2.49b}$$

$$(ia \| jb) = \iint dr \, dr' \left[\frac{\phi_i(r) \phi_i(r) \phi_i(r) \phi_i(r) - \phi_i(r) \phi_i(r) \phi_i(r) \phi_i(r)}{|r - r'|} \right] \tag{2.49c}$$

where ε_a and ε_i represent the orbital energies of the single electron orbitals ϕ_a and ϕ_i, and $(ia||jb)$ refers to antisymmetrized two-electron integrals. Since doubly and higher excited determinants, which account for electron correlation, are neglected at the CIS level of theory, CIS excitation energies generally overestimate the true excitation energies. To improve the accuracy of CIS, many higher excited configurations are often considered in an accurate CI approximation, such as, doubles (CISD) and triples (CISDT) approximations [102]. Also, an efficient second-order perturbative correction to the CIS excitation energy is the so-called CIS(D) approximation [85, 125], which ensures the size-consistency of CIS.

2.3.2 Møller-Plesset Perturbation Theory (MP)

Møller-Plesset perturbation theory (MP) [114, 126] is a size-consistent *post*-Hartree-Fock *ab initio* method, which is not variational. As a special case of Rayleigh-

Schrödinger perturbation theory (RS), the MP method can be used to obtain a perturbative approximation to the electron correlation energy of an uncorrelated reference state which corresponds to the HF ground state.

In RS perturbation theory, the Hamiltonian is sepatrated into an unperturbed Hamiltonian operator and a correction perturbation

$$\hat{H} = \hat{H}_0 + \lambda \hat{V} \tag{2.50}$$

where λ is an arbitrary perturbation parameter. The first term refers to the zeroth-order Hamiltonian and the second term is a small perturbation to the ground state. The Schrödinger equation for the perturbed state is given by

$$\hat{H}\Psi_i = (\hat{H}_0 + \lambda \hat{V})\Psi_i = E_i \Psi_i \tag{2.51}$$

The perturbed wavefunction and energy can be expanded in a Taylor series in powers of λ. Thus, one can write the eigenvalue equation as

$$(\hat{H}_0 + \lambda \hat{V}) \sum_{n=0} \lambda^n \Psi_i^{(n)} = (\sum_{n=0} \lambda^{(n)} E_i^{(n)})(\sum_{n=0} \lambda^n \Psi_i^{(n)}) \tag{2.52}$$

Invoking intermediate normalization we get

$$<\phi_i^{(0)} | \Psi_i^{(n)}> = <\phi_i^{(0)} | \phi_i^{(0)}> + \lambda <\phi_i^{(0)} | \phi_i^{(1)}> + \lambda^2 <\phi_i^{(0)} | \phi_i^{(2)}> + \ldots = 1 \tag{2.53}$$

Since the zeroth-order wavefunction is normalized, it has the form

$$<\phi_i^{(0)} | \phi_i^{(0)}> = 1 \tag{2.54}$$

and thus

$$<\phi_i^{(0)} | \phi_i^{(n)}> = 0 \tag{2.55}$$

In MP perturbation theory, equation (2.50) is simplified as

$$\hat{H} = \hat{H}_0 + \lambda \hat{V} \tag{2.56}$$

where the unperturbed H_0 is defined as the Fock-operator and the perturbation V is the difference between the full Hamiltonian and the Fock-operator.

$$\hat{H}_0 = \sum_i \hat{f}(i) = \sum_i [\hat{h}(i) + \hat{v}^{HF}(i)] \tag{2.57}$$

$$\hat{V} = \hat{H} - \hat{f} = \sum_{i<j} r_{ij}^{-1} - \sum_i \hat{v}^{HF}(i) \tag{2.58}$$

where v^{HF} corresponds to the Coulomb and exchange interaction of electron i with the Hartree-Fock mean-field.

Using the zeroth-order wavefunction, the zeroth-order MP energy can be simply written as

$$E_0^{(0)} = <\phi_i^{(0)} | \hat{H}_0 | \phi_i^{(0)}> = \sum_i^n \varepsilon_i \tag{2.59}$$

where ε_i is the orbital energy of orbital i. Note that this zeroth-order perturbation energy is not the same as the Hartree-Fock energy.

The corresponding first-order correction to the energy is given by

$$\begin{aligned} E_0^{(1)} &= <\phi_i^{(0)} | \hat{V} | \phi_i^{(0)}> = <\phi_i | \sum_{i<j} r_{ij}^{-1} - \sum_i v^{HF}(i) | \phi_i> \\ &= \frac{1}{2} \sum_i \sum_j (<ii|jj> - <ij|ji>) - \sum_i <i|v^{HF}|i> \\ &= -\frac{1}{2} \sum_{i,j} <ij||ji> \end{aligned} \tag{2.60}$$

Therefore, the Hartree-Fock energy is simply the sum of the zeroth and first order energy

$$E_{HF} = E_0^{(0)} + E_0^{(1)} = E_{MP1} \tag{2.61}$$

Similarly, the second order correction in the perturbation can be expressed as

$$E_0^{(2)} = <\phi_i^{(0)} | \hat{V} | \phi_i^{(1)}> = -\sum_{i<j,a<b} \frac{|<ab||ij>|^2}{\varepsilon_a + \varepsilon_b - \varepsilon_i - \varepsilon_j} = -\frac{1}{4} \sum_{i,j,a,b} \frac{|<ab||ij>|^2}{\varepsilon_a + \varepsilon_b - \varepsilon_i - \varepsilon_j} \tag{2.62}$$

Eventually, the expression of the total MP electronic energy in second order is given as

$$E_{MP2} = E_{HF} + E_0^{(2)} = \sum_i^n \varepsilon_i - \frac{1}{2} \sum_{i,j} <ij||ji> - \frac{1}{4} \sum_{i,j,a,b} \frac{|<ab||ij>|^2}{\varepsilon_a + \varepsilon_b - \varepsilon_i - \varepsilon_j} \tag{2.63}$$

Overall, MP theory is considered to be a powerful approach for calculating the

correlation energy. This method not only provides varying MP orders of correction to the Hartree-Fock energy, but allows for an accurate description of the ground state and its properties. However, the computational cost can be expensive even at the MP2 level of theory for larger molecules, thus limiting the applicability of the canonical MP scheme at high orders.

2.3.3 Coupled Cluster Theory (CC)

The coupled cluster (CC) method [115] is a highly accurate and widely-applied post-HF method for the calculation of atomic and molecular electronic structure. Unlike the linear expansion of the wavefunction in CI, the electronic Schrödinger equation is reformulated as a nonlinear equation in CC via an exponential expansion. The CC method provides an accurate and size-extensive approximate solutions of the electronic Schrödinger equation for weakly correlated systems, but its computational cost is very high and thus it is limited to atoms and small molecules. The essential idea in CC theory is that the ground state wave function can be written in terms of an exponential expansion ansatz

$$\begin{aligned} |\Psi_{CC}> &= e^{T}|\phi_0> \\ &= (1+\mathrm{T}+\frac{T^2}{(2!)}+\frac{T^3}{(3!)}+\ \ldots\ )|\phi_0(r)> \end{aligned} \tag{2.64}$$

The cluster operator is defined as

$$T = T_1 + T_2 + T_3 + \ldots + T_n \tag{2.65}$$

with

$$T_1|\phi_0> = \sum_{i,a} t_i^a \phi_i^a \tag{2.66}$$

$$T_2|\phi_0> = \sum_{i>j,a>b} t_{ij}^{ab} \phi_{ij}^{ab} \tag{2.67}$$

where T_n refers to cluster operators that generate singly-excited, doubly-excited, and higher-order excited determinants from the reference wavefunction. In other words,

each order of the cluster operator refers to the corresponding excitation classes. For example, the popular coupled cluster singles and doubles (CCSD) model [38] only contains the singles and doubles excitations T_1 and T_2, indicating that the cluster operator is truncated: $T_{CCSD}=T_1+T_2$. However, also determinants corresponding to higher-order excitations contribute to the truncated CC wave function. Therefore, the CC method recovers much more correlation energy than the CI method at the same truncation level, i.e. CCSD compared to CISD.

The time-independent *Schrödinger* equation is written in the form

$$\hat{H}|\Psi_{CC}\rangle = \mathrm{E}|\Psi_{CC}\rangle \tag{2.68}$$

and substituting the CC wave function yields

$$\hat{H}\,e^{T}|\phi_0\rangle = E_{CC}\,e^{T}|\phi_0(r)\rangle \tag{2.69}$$

Ultimately, the final CC energy is given as

$$E_{CC} = \langle\phi_0|e^{-T}\mathrm{H}\,e^{T}|\phi_0\rangle \tag{2.70}$$

Although the CC theory is not variational, because eq. 2.69 is not multiplied from the left be $\langle\phi_0|e^{-T^{\dagger}}$ but instead with $\langle\phi_0|e^{-T}$, the CC method is frequently used in quantum chemistry due to its size-consistency. To obtain high precision, only including singles and doubles in the cluster operator at the CCSD level is not sufficient. Often, some form of triples have to be taken into account. For example, the well known CCSD(T) method [127-128], which is termed as 'gold standard' of quantum chemitry, provides an effective estimate of the triples contribution to the energy. However, the higher-order coupled-cluster methods such as CCSDT and CCSDTQ are only used for high quality calculations of small systems, since the computational cost is very high. Moreover, recent extensions to linear-response CC theory and equation-of-motion CC theory are capable of computing electronically excited states. Excited states can also be calculated by extended approximate schemes such as the coupled cluster scheme of second order (CC2) [84, 129-130] and third order (CC3) [131-132].

2.4 The Algebraic Diagrammatic Construction of the Polarization Propagator (ADC)

The algebraic diagrammatic construction scheme for the polarization propagator is a robust and useful *ab initio* method for the treatment of electronic excitation in molecules based on perturbation theory [40-42, 91-92, 133]. Due to its size-consistency and Hermitian structure, ADC schemes can be used for the theoretical investigation of excited states and properties, ranging from small to large molecules [41]. The ADC scheme was derived originally from many-body Green's function theory. A general derivation of algebraic expressions via the intermediate state representation (ISR) [93, 133-134] is briefly introduced in the context of the Møller-Plesset partitioning of the Hamiltonian. Using a specific ISR concept, the ADC method allows for the direct computation of excited states and their properties. Specifically, the ADC secular matrix is given as a representation of the shifted Hamiltonian in the basis of the ADC intermediate states, which provides a clear representation of the excited state wavefunction. Consequently, a straightforward calculation of excited state properties is possible.

2.4.1 Original derivation

Green's functions provide a way to solve inhomogeneous differential equations. In general, in many-body systems, it is difficult to construct a Green's function for a single-particle *Schrödinger* equation. However, the Green's function propagators still can generate solutions for certain problems in many-body systems. For example, the time evolution of the polarization of a many-body system can be described by polarization propagators, which work on a time-dependent ground state wavefunction of the system and thus propagate the time-dependent density fluctuations. In the spectral representation, the polarization propagator can be written as

$$\prod_{pq,rs}(\omega)=\sum_{n\neq 0}\left(\frac{<\Psi_0|c_q^{\dagger}c_p|\Psi_n><\Psi_0|c_r^{\dagger}c_s|\Psi_n>}{\omega+E_0^N-E_n^N}-\frac{<\Psi_0|c_r^{\dagger}c_s|\Psi_n><\Psi_0|c_q^{\dagger}c_p|\Psi_n>}{\omega-E_0^N+E_n^N}\right)$$

(2.71)

where Ψ_0 and Ψ_n refer to the electronic ground and n-th excited state wavefunctions with corresponding energies E^N_0 and E^N_n, respectively. The creation and annihilation operators refer to the canonical Hartree-Fock orbitals, which are expressed by $c^{\dagger}_q$ and c_p. The poles of the polarization propagator correspond to the positive and negative vertical excitation energies $\omega_n=E_n^N-E_0^N$.

The spectral representation of the polarization propagator in the eigenstates of the many-body systems can be reformulated by diagonalizing the molecular Hamiltonian, given as

$$\prod(\omega)=X^{\dagger}(\omega-\Omega)^{-1}X \tag{2.72}$$

where Ω refers to the diagonal matrix of excitation energies ω_n and X refers to the matrix of transition amplitudes. To derive approximate ADC schemes, one has to postulate equation (2.72) in a non-diagonal matrix representation based on the Feynman-Goldstone diagrammatic perturbation series

$$\prod(\omega)=f^{\dagger}(\omega-M)^{-1}f \tag{2.73}$$

where **M** refers to the non-diagonal matrix representation and **f** refers to the matrix of effective transition moments. The two matrices **M** and **f** can be expanded independently using the Møller-Plesset partitioning of the Hamiltonian:

$$M=M^{(0)}+M^{(1)}+M^{(2)}+\ldots \tag{2.74}$$

$$f=f^{(0)}+f^{(1)}+f^{(2)}+\ldots \tag{2.75}$$

Therefore, the explicit algebraic expressions for the matrix elements of **M** and **f** can be obtained from a diagrammatic analysis of the perturbation expansion of Π(ω). The *n*th order of an ADC(n) scheme determines all contributions to describe Π(ω) that is consistent with the corresponding contributions in perturbation theory. Thus, the ADC

scheme is regarded as a reformulation of the polarization propagator expressed by the diagrammatic perturbation series expansion. The polarization propagator has poles at the positive and negative vertical excitation energies, which can be gained by diagonalization of the matrix M. Now that the ADC matrix **M** is obtained, the Hermitian eigenvalue problem arises

$$MY = Y\Omega \tag{2.76}$$

where Y refers to the matrix of ADC eigenvectors y. Thus, the vertical excitation energies ω_n can be obtained. To achieve expressions for the ADC matrix and transition amplitudes, an alternative route based on the intermediate state representation (ISR) approach is available. The ISR approach is discussed in the following section.

2.4.2 Intermediate State Representation (ISR)

The ISR approach [133-134] provides a more elegant way to construct the electronic Hamiltonian in a basis of intermediate states and thus generates the ADC equations in terms of second quantization by using creation and annihilation operators. The correlated excited state, can be formally constructed by acting excitation operators on the MP ground state.

$$|\Psi_J> = \hat{C}_J |\Psi_0^{MP}> \tag{2.77}$$

with the excitation operators

$$\{\hat{C}_J\} = \{\hat{c}_a^\dagger \hat{c}_i, \hat{c}_a^\dagger a_b^\dagger \hat{c}_i \hat{c}_j, \ldots\} \tag{2.78}$$

generating singly excited, doubly excited states, and so on. Then, the orthogonalization of these correlated excited state can be obtained via Gram-Schmidt to build up the orthonormal intermediate states basis $\{\widetilde{\Psi}\}$.

Subsequently, the corresponding ADC matrix representation of the shifted Hamiltonian can be expressed in terms of the intermediate state basis as

$$M_{IJ} = <\widetilde{\Psi}_I | \hat{H} - E_0 | \widetilde{\Psi}_J> \tag{2.79}$$

where E_0 is the exact ground state energy.

Thus, the corresponding hermitian ADC secular ISR equation becomes

$$MX = X\Omega \quad \text{and} \quad X^{\dagger} X = 1 \tag{2.80}$$

with the hermitian secular matrix M and the eigenvector matrix X.

As a consequence, one can calculate the excitation energies by solving the hermitian eigenvalue equation (2.80) within the ISR formalism. The elements of the diagonal matrix $\mathbf{\Omega}$ are assigned as excitation energies ω_n

$$\omega_n = E_n - E_0 \tag{2.81}$$

The exact excited states are constructed in terms of the intermediate state basis according to

$$|\Psi_n> \; = \; \sum_J y_{nJ} |\widetilde{\Psi}_J> \tag{2.82}$$

Similarly, the transition dipole moments T_n can be expressed in terms of a one-particle operator as

$$T_n = <\Psi_n | \hat{O} | \Psi_0^{MP}> \tag{2.83}$$

with the one-particle operator

$$\hat{O} = \sum_{p,q} o_{pq} \hat{c}_P^{\dagger} \hat{c}_q \tag{2.84}$$

Inserting exact excited states in terms of the ISR form into equation (2.83), the transition moment of an excited state, represented by the dipole operator, becomes

$$T_n = \sum_{p,q,J} y_{nJ} <\widetilde{\Psi}_J | \hat{c}_P^{\dagger} \hat{c}_q | \Psi_0> \; o_{pq} \tag{2.85}$$

Note that a perturbation series expansion of the ISR basis M in Møller-Plesset perturbation theory can be truncated at a certain order n for the consistent set of ADC(n) approximation schemes with respect to the corresponding configuration space of singly, doubly, ... excited configurations. In other words, the *n*th order of ADC(n) schemes for excitation energies is consistent with the same *n*th order Møller-Plesset ground state.

2.4.3 Construction and Structure of the ADC matrix

In general, the ADC matrix M [42, 92] consists of a series of block structures, which represent different excitation configurations, such as particle-hole (p-h), the two-particle-two-hole (2p-2h) excitations and so on. To derive the ADC matrix expression explicitly, equation (2.79) has to be constructed by invoking an IS expansion with respect to the ground state. The correlated excited states can be expressed by the IS in an orthogonal form by applying the Gram-Schmidt orthogonalization procedure. For the intermediate *p-h* states, the precursor state is given by

$$|\Psi_I^{\#}\rangle = C_I|\Psi_0\rangle - |\Psi_0\rangle\langle\Psi_0|C_J|\Psi_0\rangle \tag{2.86}$$

Thus, the orthonormalized intermediate states can be expressed as

$$|\widetilde{\Psi}_I\rangle = \sum_J |\Psi_J^{\#}\rangle\,(S^{-\frac{1}{2}})_{IJ} \tag{2.87}$$

where S_{IJ} refers to the overlap between the precursor states *I* and *J*,

$$\begin{aligned} S_{IJ} &= \langle\Psi_I^{\#}|\Psi_J^{\#}\rangle = (\langle\Psi_0|C_I^{\dagger} - \langle\Psi_0|C_I^{\dagger}|\Psi_0\rangle\langle\Psi_0|)(C_J|\Psi_0\rangle - |\Psi_0\rangle\langle\Psi_0|C_J|\Psi_0\rangle) \\ &= \langle\Psi_0|C_I^{\dagger}C_J|\Psi_0\rangle - \langle\Psi_0|C_I^{\dagger}|\Psi_0\rangle\langle\Psi_0|C_J|\Psi_0\rangle \end{aligned} \tag{2.88}$$

Owing to the orthonormality, the intermediate states fulfil the following demands:

$$\langle\widetilde{\Psi}_J|\widetilde{\Psi}_I\rangle = \delta_{IJ} \quad \text{and} \quad \langle\widetilde{\Psi}_J|\Psi_0\rangle = 0 \tag{2.89}$$

Inserting the obtained intermediate states into equation (2.79), a matrix of the shifted Hamiltonian can be written as

$$(M)_{IJ} = \langle\widetilde{\Psi}_I|H - E_0|\widetilde{\Psi}_J\rangle \tag{2.90}$$

with the ADC matrix M.

The ADC secular matrix **M** can be represented by matrix block structures as shown in Figure 2.1. For example, the ADC(2) matrix comprises four different excitations blocks p-h,p-h and p-h,2p-2h as well as 2p-2h,p-h and 2p-2h,2p-2h, which can be tackled in different orders of perturbation theory.

Notably, two different versions ADC(2)-s [42, 133] and ADC(2)-x [91, 118] are available at second order. The latter is an extension of the ADC(2)-s scheme. While the matrix elements of the 2p-2h,2p-2h block can be expanded up to first order, those of ADC(2)-s only are treated in zeroth order of perturbation theory.

$M^{(n)}$	p-h	2p-2h
p-h	(n=2):0-2 (n=3):0-3	(n=2):1 (n=3):1-2
2p-2h	(n=2):1 (n=3):1-2	(n=2)s:0 (n=2)x:0-1 (n=3):0-1

Figure 2.1: The block structure of the ADC matrix $M^{(n)}$ at different truncation levels of perturbation theory. The n-th order ADC matrix corresponds to the blocks involving the contributing terms in perturbation theory at different truncation levels.

2.4.4 Derivation of the ADC Matrix

At first, the block-terms can be expanded in terms of perturbation theory as

$$\left(M\right)_{IJ}^{(k+l+m)}\lambda^{(k+l+m)}=\sum_{K,L}\left(S_{IK}^{-\frac{1}{2}}\right)^{(k)}\lambda^{(k)}\left(<\Psi_K^{\#}|H-E_0|\Psi_L^{\#}>\right)^{(l)}\lambda^{(l)}\left(S_{LJ}^{-\frac{1}{2}}\right)^{(m)}\lambda^{(m)} \tag{2.91}$$

where λ refers to an auxiliary index.

Accordingly, inserting the perturbation expansions for the precursor states into equation (2.88), the overlap matrix is given by

$$\begin{aligned} S_{IJ}=\sum_n \lambda^{(n)}S_{IJ}^{(n)}=\sum_{k,l}\lambda^{(k+l)}<\Psi_0^{(k)}|C_I^{\dagger}\,C_J|\Psi_0^{(l)}> \\ -\sum_{k,l,m,n}\lambda^{(k+l+m+n)}<\Psi_0^{(k)}|C_I^{\dagger}|\Psi_0^{(l)}><\Psi_0^{(m)}|C_J|\Psi_0^{(n)}> \end{aligned} \tag{2.92}$$

Based on Rayleigh–Schrödinger perturbation theory, the expansion of the ground state

wavefunction is written as

$$|\Psi_0\rangle = \sum_{n=1}^{\infty} |\Psi_0^{(n)}\rangle \tag{2.93}$$

For the zeroth order, the overlap S_{IJ} becomes

$$S_{IJ}^{(0)} = \langle \Psi_0^{(0)} | C_I^{\dagger} C_J | \Psi_0^{(0)} \rangle = \delta_{IJ} \tag{2.94}$$

The expression of the overlap matrix in first order is given by

$$S_{IJ}^{(1)} = \langle \Psi_0^{(1)} | C_I^{\dagger} C_J | \Psi_0^{(0)} \rangle + \langle \Psi_0^{(0)} | C_I^{\dagger} C_J | \Psi_0^{(1)} \rangle = 0 \tag{2.95}$$

Thus, the contributions of the first order terms of the overlap S_{IJ} are considered to be negligible.

Similarly, the second order terms of the overlap matrix S_{IJ} can be formulated as

$$S_{IJ}^{(2)} = \langle \Psi_0^{(1)} | C_I^{\dagger} C_J | \Psi_0^{(1)} \rangle \tag{2.96}$$

Ultimately, the elements of the overlap matrix S can be expressed as

$$S_{IJ} = \delta_{IJ} + S_{IJ}^{(2)} + O(3) \tag{2.97}$$

where O(3) refers to the third and higher order contributions. The contribution of the elements within the first order block vanishes.

To derive the expression of the intermediate states, the explicit expression of $S^{-½}$ is required and can be expanded in a Taylor series. The second order expression of S_{IJ} can be regarded as a function

$$S(x) = \mathbb{1} + x \tag{2.98}$$

where $x = S^{(2)} + O(3)$

Then, an expression of $S^{-½}$ in a Taylor series is obtained

$$\begin{aligned} S^{-\frac{1}{2}}(x) &= S^{-\frac{1}{2}}(0) + \left(S^{-\frac{1}{2}}(0)\right)'(x-0) + \dots \\ &= \mathbb{1} - \frac{1}{2}x \\ &= \mathbb{1} - \frac{1}{2}S^{(2)} + O(3) \end{aligned} \tag{2.99}$$

Eventually, the expression of $S_{IJ}^{-\frac{1}{2}}$ in the second order is given by

$$S_{IJ}^{-\frac{1}{2}}(x) = \delta_{IJ} - \frac{1}{2}\left(S_{IJ}^{(2)} + O(3)\right) \tag{2.100}$$

Now that the expressions for the overlap matrix **S** are derived, the explicit matrix representation of the shifted Hamiltonian can be reformulated as

$$M_{IJ}^{\#} = <\Psi_I^{\#}|H - E_0|\Psi_J^{\#}> = <\Psi_0|C_I^{\dagger}(H - E_0)C_J|\Psi_0> \tag{2.101}$$

The expressions of the shifted Hamilton matrix are expanded in terms of perturbation theory. As a consequence, the expressions up to second order have the following forms

$$\begin{aligned} \left(M_{IJ}^{\#}\right)^{(0)} &= \left(<\Psi_I^{\#}|H - E_0|\Psi_J^{\#}>\right)^{(0)} = <\Psi_0^{(0)}|C_I^{\dagger}H^{(0)}C_J|\Psi_0^{(0)}> - <\Psi_0^{(0)}|C_I^{\dagger}E_0^{(0)}C_J|\Psi_0^{(0)}> \\ \left(M_{IJ}^{\#}\right)^{(1)} &= \left(<\Psi_I^{\#}|H - E_0|\Psi_J^{\#}>\right)^{(1)} = <\Psi_0^{(0)}|C_I^{\dagger}H^{(1)}C_J|\Psi_0^{(0)}> - <\Psi_0^{(0)}|C_I^{\dagger}E_0^{(1)}C_J|\Psi_0^{(0)}> \\ \left(M_{IJ}^{\#}\right)^{(2)} &= \left(<\Psi_I^{\#}|H - E_0|\Psi_J^{\#}>\right)^{(2)} = <\Psi_0^{(1)}|C_I^{\dagger}H^{(1)}C_J|\Psi_0^{(0)}> + <\Psi_0^{(0)}|C_I^{\dagger}H^{(1)}C_J|\Psi_0^{(1)}> \\ &\quad + <\Psi_0^{(1)}|C_I^{\dagger}H^{(0)}C_J|\Psi_0^{(1)}> - <\Psi_0^{(0)}|C_I^{\dagger}E_0^{(2)}C_J|\Psi_0^{(0)}> - <\Psi_0^{(1)}|C_I^{\dagger}E_0^{(0)}C_J|\Psi_0^{(1)}> \end{aligned} \tag{2.102}$$

Next, the zeroth and first order terms of the p-h,p-h block are evaluated by invoking explicit expressions of the excitation operators $\{C_J\}$ and Wick's theorem [135].

Thus, the matrix element for the zeroth order p-h,p-h block is given by

$$M_{IJ}^{(0)} = \sum_{K,L} \left(S_{IK}^{-\frac{1}{2}}\right)^{(0)} M_{IJ}^{\#(0)} \left(S_{LJ}^{-\frac{1}{2}}\right)^{(0)} \tag{2.103}$$

Introducing the explicit expressions of the excitation operators yields

$$M_{ai,bj}^{(0)} = \sum_{ckdl} (S_{aick}^{-\frac{1}{2}})^{(0)} (<\Psi_{ck}^{\#} | H - E_0 | \Psi_{dl}^{\#}>)^{(0)} (S_{dlbj}^{-\frac{1}{2}})^{(0)}$$
$$= \sum_{ckdl} \delta_{ac}\delta_{ik} <\Psi_0^{(0)} | c_i^{\dagger} c_a H^{(0)} c_b^{\dagger} c_j | \Psi_0^{(0)}> - <\Psi_0^{(0)} | c_i^{\dagger} c_a E_0^{(0)} c_b^{\dagger} c_j | \Psi_0^{(0)}> \delta_{bd}\delta_{jl}$$
$$= \sum_{ckdl} \sum_{p} \delta_{ac}\delta_{ik}\varepsilon_p <\Psi_0^{(0)} | c_i^{\dagger} c_a c_p^{\dagger} c_p c_b^{\dagger} c_j | \Psi_0^{(0)}> - <\Psi_0^{(0)} | c_i^{\dagger} c_a E_0^{(0)} c_b^{\dagger} c_j | \Psi_0^{(0)}> \delta_{bd}\delta_{jl}$$

(2.104)

Using Wick's theorem, the expectation value of the zeroth order Hamilton matrix can be obtained as

$$\sum_p \varepsilon_p <\Psi_0^{(0)} | c_i^{\dagger} c_a c_p^{\dagger} c_p c_b^{\dagger} c_j | \Psi_0^{(0)}> = (\sum_{pi} \varepsilon_{pi}\delta_{ac}\delta_{ik}) + \varepsilon_a\delta_{ij}\delta_{ab} + \varepsilon_i\delta_{ij}\delta_{ab} = \delta_{ij}\delta_{ab}(E_0^{(0)} + \varepsilon_a - \varepsilon_i)$$

(2.105)

Therefore, the zeroth matrix element for the p-h,p-h block can be reformulated as

$$M_{ai,bj}^{(0)} = \sum_{ckdl} \delta_{ac}\delta_{ik} <\Psi_0^{(0)} | c_i^{\dagger} c_a H^{(0)} c_b^{\dagger} c_j | \Psi_0^{(0)}> - <\Psi_0^{(0)} | c_i^{\dagger} c_a E_0^{(0)} c_b^{\dagger} c_j | \Psi_0^{(0)}> \delta_{bd}\delta_{jl}$$
$$= \delta_{ij}\delta_{ab}(E_0^{(0)} + \varepsilon_a - \varepsilon_i) - \delta_{ij}\delta_{ab}E_0^{(0)}$$
$$= \delta_{ij}\delta_{ab}(\varepsilon_a - \varepsilon_i)$$

(2.106)

In a similar way, the first order term of the p-h,p-h block is written as

$$M_{IJ}^{(1)} = \sum_{K,L} (S_{IK}^{-\frac{1}{2}})^{(0)} M_{IJ}^{\#(1)} (S_{LJ}^{-\frac{1}{2}})^{(0)} = <\Psi_0^{(0)} | C_I^{\dagger} H^{(1)} C_J | \Psi_0^{(0)}> - <\Psi_0^{(0)} | C_I^{\dagger} E_0^{(1)} C_J | \Psi_0^{(0)}>$$

(2.107)

The expectation value of the first order Hamilton matrix can be evaluated as

$$\begin{aligned} <\Psi_0^{(0)} | C_I^{\dagger} H^{(1)} C_J | \Psi_0^{(0)}> &= <\Psi_0^{(0)} | c_i^{\dagger} c_a H^{(1)} c_b^{\dagger} c_j | \Psi_0^{(0)}> \\ &= -\sum_{pq}\sum_{k} <\mathrm{pk}||\mathrm{qk}> <\Psi_0^{(0)} | c_i^{\dagger} c_a c_p^{\dagger} c_q c_b^{\dagger} c_j | \Psi_0^{(0)}> \\ &\quad + \frac{1}{2}\sum_{pqrs} <\mathrm{pq}||\mathrm{rs}> <\Psi_0^{(0)} | c_i^{\dagger} c_a c_p^{\dagger} c_q^{\dagger} c_r c_s c_b^{\dagger} c_j | \Psi_0^{(0)}> \end{aligned} \quad (2.108)$$

These terms can be simplified using the definition of Wick's theorem

$$<\Psi_0^{(0)} | C_I^{\dagger} H^{(1)} C_J | \Psi_0^{(0)}> = <\Psi_0^{(0)} | c_i^{\dagger} c_a H^{(1)} c_b^{\dagger} c_j | \Psi_0^{(0)}> = \delta_{ij}\delta_{ab} E_0^{(1)} - <\mathrm{aj}||\mathrm{bi}> \quad (2.109)$$

Ultimately, the first order matrix elements for the p-h,p-h block are given as

$$\begin{aligned} M^{(1)}_{ai,bj} &= \sum_{K,L} \left(S^{-\frac{1}{2}}_{IK}\right)^{(0)} M^{\#(1)}_{IJ} \left(S^{-\frac{1}{2}}_{LJ}\right)^{(0)} = \langle \Psi^{(0)}_0 | C^{\dagger}_I H^{(1)} C_J | \Psi^{(0)}_0 \rangle - \langle \Psi^{(0)}_0 | C^{\dagger}_I E^{(1)}_0 C_J | \Psi^{(0)}_0 \rangle \\ &= \sum_{ckdl} \delta_{ac}\delta_{ik} (\langle \Psi^{(0)}_0 | c^{\dagger}_i c_a H^{(1)} c^{\dagger}_b c_j | \Psi^{(0)}_0 \rangle - \langle \Psi^{(0)}_0 | c^{\dagger}_i c_a E^{(1)}_0 c^{\dagger}_b c_j | \Psi^{(0)}_0 \rangle) \delta_{bd}\delta_{jl} \\ &= \delta_{ac}\delta_{ik} E^{(1)}_0 - \langle aj||bi \rangle - \delta_{ac}\delta_{ik} E^{(1)}_0 \\ &= - \langle aj||bi \rangle \end{aligned}$$

(2.110)

In view of all contributions to the second order ADC(2) matrix, not only the second order terms for the p-h,p-h block but also the first order matrix elements for the coupling 2p-2h,p-h and p-h,2p-2h blocks as well as the zeroth order term for the 2p-2h,2p-2h block need to be considered. Here, only the explicit expressions are presented and detailed derivations can be found in literature [42, 133]. Eventually, the final second order matrix elements for the p-h,p-h block are given by

$$\begin{aligned} M^{(2)}_{ai,bj} = {} & \frac{1}{4}\delta_{ij} \sum_{ckl} (t_{ackl} \langle kl||bc \rangle + t_{klbc} \langle kl||ac \rangle) + \frac{1}{4}\delta_{ab} \sum_{cdk} (t_{cdik} \langle jk||cd \rangle + t_{jkcd} \langle cd||ik \rangle) \\ & - \frac{1}{2} \sum_{ck} (t_{acik} \langle jk||bc \rangle + t_{jkbc} \langle ac||ik \rangle) \end{aligned}$$

(2.111)

where $t_{abij} = t^{ij}_{ab} = \dfrac{\langle ab||ij \rangle}{\varepsilon_a + \varepsilon_b - \varepsilon_i - \varepsilon_j}$.

Accordingly, the explicit expressions for the first order 2p-2h,p-h block, p-h,2p-2h block and the zeroth order 2p-2h,2p-2h block are summarized as

$$M^{(1)}_{ia,kcld} = \langle kl||id \rangle \delta_{ac} - \langle kl||ic \rangle \delta_{ad} - \langle al||cd \rangle \delta_{ik} + \langle ak||cd \rangle \delta_{il} \tag{2.112a}$$

$$M^{(1)}_{iajb,kc} = \langle kb||ij \rangle \delta_{ac} - \langle ka||ij \rangle \delta_{bc} - \langle ab||cj \rangle \delta_{ik} + \langle ab||ci \rangle \delta_{jk} \tag{2.112b}$$

$$M^{(0)}_{iajb,kcld} = (\varepsilon_a + \varepsilon_b - \varepsilon_i - \varepsilon_j) \delta_{ac}\delta_{bd}\delta_{ik}\delta_{jl} \tag{2.112c}$$

2.5 Density Functional Theory (DFT) and time-dependent DFT (TDDFT)

2.5.1 Density Functional Theory

Density functional theory (DFT) [110-111, 136] is one of the most popular and successful quantum mechanical approaches to calculate the electronic structure of the ground state for many-body systems in quantum chemistry, quantum physics and materials science. The basic concepts underlying density functional theory are introduced and the formalism of ground state DFT is briefly described. DFT provides an alternative approach to solve the electronic *Schrödinger* equation of many-electron systems, which is different from the traditional solution of the Schrödinger equation with the Hartree-Fock-Slater model as mentioned in chapter 2.2. The central idea of DFT originates from the first Hohenberg-Kohn (HK) theorem [110], which states that for non-degenerate ground states the ground-state electron density ρ(r) determines the external potential $v_{ext}(r)$ and hence the Hamiltonian H as well as the electronic wavefunction $\Psi(r)$. Consequently, all ground-state properties of the electronic system can be identified in terms of the ground state electron density $\rho(r)$. The second Hohenberg-Kohn theorem establishes a variational principle for the ground state density functional E[ρ] that can be derived from minimizing a functional of the electron density. For a given ground-state density ρ(r), the number of electrons N can be expressed as

$$\int \rho(r)dr = N \tag{2.113}$$

Subsequently, the total energy functional for an N-electron ground state can be minimized by the ground-state electron density as

$$E(\rho) = T(\rho) + V_{ee}[\rho] + V_{ext}(\rho) \tag{2.114}$$

where V_{ext} refers to an external potential. The Hamiltonian is composed of $T+V_{ee}+V_{ext}$.

Applying the variational theorem for the Schrödinger equation of the N-electron system,

the minimum value of the energy functional E[ρ] is given by

$$E[\rho]=T[\rho]+\int \rho(r)V_{ext}[\rho]dr \geq E_0 \tag{2.115}$$

where E_0 refers to the exact ground state electronic energy.

Kohn and Sham [111] proposed an intelligent approach to the kinetic and electron-electron functionals for minimizing the energy directly. This approach assumes that the wavefunction of a many-electron system of non-interacting electrons can be described by a single determinant in N single-electron orbitals $\psi_i(r)$. Since the ansatz corresponds to a non-interacting system, the energy contributions of correlation interactions might be neglected. Nevertheless, for a fictitious system of non-interacting electrons, the true ground state density can be written as

$$\rho(r)=\sum_i |\psi_i(r)|^2 \tag{2.116}$$

where ψ_i refers to the single-electron orbitals according to the Kohn-Sham (KS) ansatz.

Then, the exact kinetic energy of a non-interacting system can be written as

$$T_0=-\frac{1}{2}\sum_i \int \psi_i^* \nabla_i^2 \psi_i \tag{2.117}$$

Using the variational principle with respect to the single-electron orbitals for the modified Hamiltonian yields the Kohn-Sham equations

$$\left(-\frac{1}{2}\nabla_i^2+v_{eff}(r)\right)\psi_i^{KS}(r)=\varepsilon_i^{KS}\psi_i^{KS}(r) \tag{2.118}$$

with an external potential v_{eff}, the Lagrangian multiplier ε_i for the corresponding orbital energies, and the Kohn-Sham orbitals ψ_i. The term v_{eff} includes all many-particle interaction effects such as the mean-field Coulomb repulsion of all other electrons and nuclei, the electron-nuclear attraction as well as an introduced so-called exchange-correlation (xc) interaction, which describes the deviation between the interacting and non-interacting systems. Thus, the external potential is given as

$$v_{eff}(r)=v_{en}+v_{ee}+v_{xc}=-\sum_i \frac{Z_i}{|r-R_i|}+\int dr' \frac{\rho(r)'}{|r-r'|}+\frac{\delta E_{xc}[\rho(r)]}{\delta\rho(r)} \tag{2.119}$$

Eventually, the ground state electronic energy within the Kohn-Sham formalism is written as

$$E[\rho]=E_T[\psi]+E_V[\rho]+E_J[\rho]+E_{xc}[\rho] \tag{2.120}$$

where E_T refers to the kinetic energy, E_V refers to the electron-nuclear interaction energy, E_J refers to the Coulomb interaction of the electron density and E_{xc} refers to the exchange correlation energy.

Therefore, an accurate solution of the Kohn-Sham equation depends on the exchange-correlation functional $E_{xc}[\rho]$ with respect to the ground state electron density. However, the remaining issue of DFT is that the exact exchange-correlation functional is unknown and thus must be approximated. Many approximations have been made in the treatment of the *xc* functionals to correct the energy error, providing good performance for the calculations of certain physical and chemical properties ranging from small molecules to bulk materials at various levels of accuracy. Currently, the most commonly and widely applied approximations used for $E_{xc}[\rho]$ in electronic structure calculations are the local density approximation (LDA)[137], generalized gradient approximation (GGA) [138], hybrid functionals approximations (BLYP [139], B3LYP [140], BHLYP [141], etc.) and so on.

2.5.2 Time-Dependent Density Functional Theory (TDDFT)

Time-dependent density functional theory (TDDFT) [37, 48-49, 142] is a common approach for excited state calculations. Similar to DFT based on the Hohenberg-Kohn theorems [110], the Runge-Gross theorem [48] is the time-dependent analogue to the Hohenberg-Kohn theorem and constitutes the cornerstone of TDDFT. It states that the complicated many-body time-dependent Schrödinger equation can be transformed to a set of time-dependent single-particle equations and the exact time-dependent electron density determines the time-dependent external potential of a system. In other words, there is a one-to-one mapping between the time-dependent external potential and the time-dependent density and hence the time-dependent potential can be expressed as a

functional of the time-dependent electron density. Similar to the time-independent Kohn-Sham equations, the time-dependent one-particle Kohn-Sham equation can be written as

$$i\frac{\partial}{\partial t}\psi_i^{KS}(r,t)=(-\frac{1}{2}\nabla_i^2+v_{KS}(r,t))\psi_i^{KS}(r,t) \qquad (1.121)$$

with

$$v_{KS}(r,t)=v_{en}(r,t)+v_{ee}+v_{xc}=v_{en}(r,t)+\int d^3r'\frac{\rho(r,t)'}{|r-r'|}+\frac{\delta A_{xc}[\rho(r,t)]}{\delta\rho(r)} \qquad (1.122)$$

where $v_{en}(r,t)$ is the time-dependent external potential. The second term refers to the electron-electron repulsion. The third term is the unknown xc functional. The exchange-correlation action functional A_{xc} refers to the xc part of the action integral. Since the exact time-dependent exchange-correlation action functional is unknown, this xc kernel of the Kohn-Sham potential for the non-interacting system has to be approximated. The time-dependent Kohn-Sham equations describe the evolution of non-interacting electrons in a time-dependent Kohn-Sham potential. Thus, once a reasonable approximation for the exchange correlation functional is obtained, the required interacting time-dependent Schrödinger equation can be tackled with the propagation of the Kohn-Sham equations.

The most popular application of TDDFT is to calculate excitation energies and oscillator strengths with two common methods using the time-dependent Kohn-Sham equations. One is the so called “real time TD-DFT” [143-144], which propagates the time-dependent Kohn-Sham wave function in time. The other one is linear-response TD-DFT [37, 145-146], which is a widely applied approach in quantum chemistry. Here, only the linear-response time-dependent DFT equation is introduced in detail.

The exciation energies within linear-response TD-DFT arise from the linear time-dependent response of the time-independent ground state electron density to a time-dependent external electric field. When the external electric field is considered as a weak perturbation, linear-response TD-DFT can accurately reproduce excitation energies and many properties of electronically excited states such as oscillator strengths.

A density-matrix formalism is introduced to conveniently express the time-dependent Kohn-Sham equations in matrix notation for linear-response TD-DFT.

Thus, the time-dependent Kohn-Sham wavefunction can be expressed

$$\psi_P(r,t)=\sum_j^M c_{pj}^{(t)}\varphi(r) \tag{2.123}$$

Conseqently, the time-dependent Kohn-Sham equation is written as

$$i\frac{\partial}{\partial t}C=F^{KS}C \tag{2.124}$$

where **C** refers to the matrix of the time-dependent expansion coefficients and $\mathbf{F}^{KS}$ refers to the matrix representation of the time-dependent Kohn-Sham operators. Then, the density matrix $\mathbf{P}_{pr}$ can be expressed in terms of the electron density via the following form

$$\rho(r,t)=\sum_i \psi_i(r,t)\psi_i^*(r,t)=\sum_i\sum_{p,q}^M c_{ip}(t)c_{iq}^*(t)\varphi_p(r)\varphi_q^*(r)=\sum_{p,q}^M P_{pq}\varphi_p(r)\varphi_q^*(r) \tag{2.125}$$

Multiplication of the equation (2.124) from the right with $C^{\dagger}$ and substituting the expression of the matrix **C** with the density matrix **P** into the equation yield the following form of the time-dependent Kohn-Sham equation in density matrix form

$$i\frac{\partial}{\partial t}P_{pr}(t)=\sum_q\{F_{pq}P_{qr}-P_{pq}F_{qr}\} \tag{2.126}$$

Assuming that the time-dependent electric field is relatively small, the system can be regarded as in the electronic ground state and hence the time-independent Kohn-Sham equation in the density matrix formulation leads to

$$\sum_q\{F_{pq}^{(0)}P_{qr}^{(0)}-P_{pq}^{(0)}F_{qr}^{(0)}\}=0 \tag{2.127}$$

with the idempotency condition

$$\sum_q P_{pq}^{(0)}P_{qr}^{(0)}=P_{pr}^{(0)} \tag{2.128}$$

where $P_{pq}^{(0)}$ refers to the Kohn-Sham density matrix and $P_{pq}^{(0)}$ refers to the Kohn-Sham Hamiltonian based on the unperturbed ground state DFT formalism.

For the excited state calculations, an oscillating time-dependent external field is applied to the system and the first order response to this perturbation is taken into account. Just like in perturbation theory, the perturbed wavefunction is written as the sum of the time-independent unperturbed ground state and the first order time-dependent perturbed term.

$$P_{pq} = P_{pq}^{(0)} + P_{pq}^{(1)} \tag{2.129}$$

Similarly, the time-dependent Kohn-Sham Hamiltonian can be regarded as the sum of the ground state Kohn-Sham Hamiltonian and the first order change

$$F_{pq} = F_{pq}^{(0)} + F_{pq}^{(1)} \tag{2.130}$$

Inserting the equations (2.129) and (2.130) into the time-dependent Kohn-Sham equation (2.126) yields

$$i\frac{\partial}{\partial t}P_{pq}^{(1)}(t) = \sum_{q}\{F_{pq}^{(0)}P_{qr}^{(1)} - P_{pq}^{(1)}F_{qr}^{(0)} + F_{pq}^{(1)}P_{qr}^{(0)} - P_{pq}^{(0)}F_{qr}^{(1)}\} \tag{2.131}$$

where $F_{pq}^{(1)}$ refers to the first order change of the Kohn-Sham Hamiltonian composed of the applied time-dependent electric field itself, g_{pq}, and the response of two-electron part of the Kohn-Sham Hamiltonian to the changes of the density matrix. Thus, the first order change of the Kohn-Sham Hamiltonian is given by

$$F_{pq}^{(1)} = g_{pq} + \Delta F_{pq}^{(0)} \tag{2.132}$$

with

$$g_{pq} = \frac{1}{2}[f_{pq}e^{-i\omega t} + f_{qp}^{*}e^{-i\omega t}] \tag{2.133}$$

$$\Delta F_{pq}^{(0)} = \sum_{st}\frac{\partial \Delta F_{pq}^{(0)}}{\partial P_{st}}P_{st}^{(1)} \tag{2.134}$$

where g_{pq} is the a one-electron operator.

Ultimately, the first order Hamiltonian becomes

$$F_{pq}^{(1)} = \frac{1}{2}[d_{pq}e^{-i\omega t} + d_{qp}^{*}e^{-i\omega t}] \tag{2.135}$$

where d_{pq} represents the perturbation densities.

Substituting equations (2.132-2.135) into the time-dependent Kohn-Sham equation (2.126) leads to the following form

$$\omega d_{pq} = \sum_{q} \{ F_{pq}^{(0)} d_{qr} - d_{pq} F_{qr}^{(0)} + (f_{pq} + \sum_{st} \frac{\partial \Delta F_{pq}^{(0)}}{\partial P_{st}} P_{st}^{(1)}) P_{qr}^{(0)} - P_{pq}^{(0)} (f_{qr} + \sum_{st} \frac{\partial \Delta F_{qr}^{(0)}}{\partial P_{st}}) \} \tag{2.136}$$

Due to the idempotency condition eq. (2.128), the first-order change of the density matrix can be expressed as

$$P_{pr}^{(1)} = \sum_{q} [P_{pq}^{(0)} P_{qr}^{(1)} + P_{pq}^{(1)} P_{qr}^{(0)}] \tag{2.137}$$

which only restricts the matrix d_{pq} to the occupied-virtual (d_{ia}) and virtual-occupied (d_{ai}) blocks in equation (2.136), whereas the remaining occupied-occupied (d_{ii}) and virtual-virtual (d_{aa}) blocks are zero.

Since the unperturbed Kohn-Sham Hamiltonian and density matrix are diagonal, the time-dependent Kohn-Sham equation gives rise to two equations [37]

$$\omega x_{ai} = F_{aa}^{(0)} x_{ai} - x_{ai} F_{ii}^{(0)} + (f_{ai} + \sum_{bj} \{ \frac{\partial \Delta F_{ai}}{\partial P_{bj}} x_{bj} + \frac{\partial \Delta F_{ai}}{\partial P_{jb}} y_{bj} \}) P_{ii}^{(0)} \tag{2.138}$$

$$\omega y_{ai} = F_{ii}^{(0)} y_{ai} - y_{ai} F_{aa}^{(0)} + P_{ii}^{(0)} (f_{ia} + \sum_{bj} \{ \frac{\partial \Delta F_{ia}}{\partial P_{bj}} x_{bj} + \frac{\partial \Delta F_{ia}}{\partial P_{jb}} y_{bj} \}) \tag{2.139}$$

Assuming that f_{ai} and f_{ia} are equal to zero due to a negligible time-dependent perturbation, the time-dependent Kohn-Sham equation [37] can be constructured in form

$$\begin{pmatrix} A & B \\ B^{*} & A^{*} \end{pmatrix} \begin{pmatrix} X \\ Y \end{pmatrix} = \omega \begin{pmatrix} 1 & 0 \\ 0 & -1 \end{pmatrix} \begin{pmatrix} X \\ Y \end{pmatrix} \tag{2.140}$$

where the matrix elements of **A** and **B** have the form

$$A_{ia,jb}=\delta_{ij}\delta_{ab}(\varepsilon_a-\varepsilon_i)+(ia|jb)+(ia|f_{xc}|jb) \tag{2.141}$$

and

$$B_{ia,jb}=(ia|bj)+(ia|f_{xc}|bj) \tag{2.142}$$

Here, f_{xc} refers to the so-called xc kernel, which is defined by

$$f_{xc}=\frac{\delta^2 E_{xc}}{\delta\rho(1)\delta\rho(2)} \tag{2.143}$$

The Tamm-Dancoff approximation (TDA) [147] to time-dependent density functional theory negelects the matrix **B** and provides a computationally simple method for molecular excited states with a negligible error compared to TDDFT. Generally, TDDFT can provide a relatively accurate description of low-lying excited states if an appropriate xc functional is employed [139-141, 148]. Therefore, it is an extremely useful and efficient method that is successfully employed for many large chemical and biochemical systems due to its simple construction and the moderate computational cost. However, TDDFT faces an enormous challenge to give a correct description of Rydberg states and charge transfer [37, 149-153]. The former is because standard xc-functionals reproduces the wrong long-range behavior for large electron-electron distances. The resulting incorrect asymptotic behavior corresponding to the distance between the positive and negative charges generated in an excited CT state accounts for the failure in the description of charge transfer states.

2.6 Continuum solvation models

In computational chemistry, a variety of *ab initio* methods provide an accurate description of electronic ground and excited states, and the transition states that occur during chemical reactions for the investigation of gas-phase molecular properties. However, external enviromental factors such as temperature, pressure and interactions

between solute and solvent may have an important influence on molecular free energies, structural changes, physical and chemical properties of atomic or molecular systems [154-155]. In practice, many experiments are carried out in water or other solvents and thus liquid solutions play an important role in chemistry. Specifically, for some polarized molecules in polar solvents the electronic structures and molecular properties are strongly affected by solvation effects. For comparison with experimental data, there is a high motivation for the development of solvent models to include solvation effects in quantum chemical calculations. Currently, several different implicit and continuum solvent models [155-164] are available for this purpose. Implicit models [158-160] are generally time-saving methods and allow a reasonable description of the solvent behaviour, but fail to tackle local fluctuations in the solvent density with an embedded solute molecule. Thus, the real environment is extremely complex and a suitable model of solvation is undoubtedly a requirement for reliable results. Well-established continuum solvation models [155-157, 161-164] were introduced and proved to be significantly important methods to account for long-range interactions for the description of solvent effects in computational chemistry. The polarizable continuum model (PCM) [155-157, 163] is one of the most commonly used and typical continuum solvation methods which employ a molecule-shaped cavity and the full molecular electrostatic potential. This model is based on the apparent surface charge (ASC) method [155], which defines an apparent surface charge distributed on the cavity surface. In such models, different defintions of the apparent surface charge σ(s) on the cavity surface lead to a series of different types of PCM models, such as the dielectric PCM (D-PCM) [155, 165], in which the continuum is polarizable, the closely-related conductor-like PCM (C-PCM) [155-157], which is similar to the conductor-like screening model (COSMO) [155,166-167], and the integral equation formalism PCM (IEFPCM) [155, 157, 168-175].

The conductor-like polarizable continuum model, C-PCM, is an efficient and reliable continuum solvation procedure, which has been implemented into many popular computational programm packages [176-177] to account for solvent effects for ground and excited state calculations. In such approaches, the COSMO model with a small

modification on the dielectric screening factor was implemented in the framework of the PCM formalism by Barone and Cossi [156]. Specifically, the solute molecule is embedded in a cavity and the solvent can be expressed as a dielectric polarizable continuum. Just like the COSMO model, the electrostatic problem related to solute-solvent interactions within the C-PCM model can be solved with a simpler dielectric model as well. The solvent reaction field is constructed approximately by the polarization charges on the surface of the cavity. The cavity surface is generated by a surface-building formalism, known as GEPOL cavity[155], using a solvent-excluding or solvent-accessible surface. The cavity surface is smoothly separated into small regions, which is called tesserae. The tesserae can be represented by the position of its center. The detailed derivations of this C-PCM model can be found in literature [156-157]. Here, only a brief overview of this model is introduced.

A solvent potential is introduced as an additional term into the Hamiltonian.

$$\hat{H} = \hat{H^0} + \hat{V} \tag{2.144}$$

where $\hat{H}$ refers to the Hamiltonian of the solute and $\hat{V}$ refers to the electrostatic solute-solvent interactions.

Applying a variational minimization procedure for the Hartree-Fock (HF) or the Kohn-Sham (KS) equations yields the free energy in solution.

$$G = <\psi| \hat{H^0} |\psi> + \frac{1}{2} <\psi|V|\psi> \tag{2.145}$$

with the conductor-like boundary condition

$$V(r) + \sum_{i}^{tesserae} V_{q_i}(r) = 0 \tag{2.146}$$

where V represents the electrostatic potential arising from the solute charges and V_q refers to the electrostatic potential owing to the polarization charges. In general, the polarization charge can be represented via finite point charges appearing in each tessera. In the COSMO and C-PCM models, the dielectric screening factor has the form

$$f_\varepsilon = \frac{\varepsilon - 1}{\varepsilon + x} \tag{2.147}$$

When ε=+∞, the solvation charges q can be expressed in the following equation:

$$Sq = -V \tag{2.148}$$

with the matrix S elements

$$\begin{aligned} S_u &= 1.0694\sqrt{4\frac{\pi}{a_i}} \\ S_{ij} &= \frac{1}{|r_i - r_j|} \end{aligned} \tag{2.149}$$

where V refers to total electrostatic potential due to the solvation charges and a_i represents the area of tessera i.

In real solvents, the dielectric constant is not infinite, and thus eq. (2.148) is written as

$$Sq = -f_\varepsilon V \tag{2.150}$$

In the original COSMO derivation the value X=0.5 is recommended, whereas the value X=0 is used for the C-PCM model due to the valid observance of Gauss' law.

$$\sum_i^{tesserae} q_i = -\frac{\varepsilon - 1}{\varepsilon} Q_{solute} \tag{2.151}$$

where Q_{solute} refers to the solute charge.

Considering the electrostatic interactions (es) in solution, the expression of the molecular free energy eq. (2.145) becomes

$$\begin{aligned} G^{es} &= \langle\psi| H^0 |\psi\rangle + \frac{1}{2}\sum_i^{tesserae} q_i V_i \\ &= E[\rho] + V_{NN} + \frac{1}{2}\sum_i^{tesserae} q_i V_i \end{aligned} \tag{2.152}$$

where V_{NN} represents the nuclear repulsion energy and ρ refers to the electronic density perturbed by the solvent. V_i is the value of the electrostatic potential on the tessera i.

Further, when the nonelectrostatic interactions (non) are considered, the expression of the free energy is given by

$$G^{non} = G^{es} + G_{cav} + G_{dis} + V_{rep} \quad (2.153)$$

where G_{cav} refers to the free energy corresponding to the formation of the cavity . G_{dis} and G_{rep} represent the dispersion and repulsion terms, respectively. The detailed expressions for free energy derivatives and the treatment of electronic properties can be found in ref [157]. The molecular relaxation perturbed by the solvent can be calculated in standard optimization procedures invoking the implementation of the free energy derivatives (eq. 2.153) for the theoretical study of many chemical systems and processes.

The polarizable continuum models have been successfully implemented in several quantum chemistry program packages [176-177] for calculating geometry optimizations, energies and frequency calculations at different levels of theory. Such models yield accurate theoretical predictions that agree well with experimental data and thus provide improved understanding of chemical properties and reaction processes that take place in solution. To effectively treat the effects of equilibrium solvation on the ground and excited states of molecules, the C-PCM model is used throughout this work.

Chapter 3

Linear Multiazobenzenes (AB-(n)): Excitation Energies, Excitonic Coupling and Isomerization Mechanisms

3.1 Background and Motivation

In the past decades, the absorption spectrum and photoisomerization of azobenzene (AB) and its derivatives have attracted growing attention and have been extensively investigated experimentally and theoretically [1-36], since *Hartley* [1] first reported a remarkable study of configuration changes of azobenzene resulting from light irradiation. In particular, with the development of *ab initio* quantum chemical methods [37-42], the accurate absorption spectra of azobenzene and a series of substituted

azobenzenes have been calculated by various theoretical approaches [30, 178-181]. Many previous calculations agree well with experimental data in gas phase and in solvents measured by means of femtosecond time resolved spectroscopy [3, 28, 30-32, 36]. With respect to the photoisomerization mechanism of AB, in fact, several possible isomerization pathways, for instance, rotation, inversion and concerted inversion pathways, have been proposed (Figure 3.1). Early in 1982, two photoisomerization pathways of AB, the rotation path of the N=N double bond for the n-π* excitation and the inversion path for the π-π* transition, were explored by *Rau* and *Lueddecke* [2]. Further theoretical evidence has been delivered by *Monti* [33] *et al*., who calculated the potential energy curves of azobenzene along the rotation pathway and the inversion pathway via configuration-interaction (CI) calculations. The potential curves clearly exhibited a large barrier for the rotation path as well as no barrier for the inversion pathway. In addition, *Diau* [34] exploited a new concerted-inversion mechanism involving the inversion of both of the CNN angels in the molecular plane. He introduced a new concerted-inversion path for the S_1 state and this way may be opened after excitation to the S_2 state. His theoretical results have been successfully proven by subsequent experimental femtosecond laser spectroscopy observations [35]. However, most recent theoretical and experimental investigations challenged the inversion mechanism and suggested that the rotation mechanism dominates the isomerization process, which mainly takes place in the S_1 state [29-30, 32, 50-51]. Apparently, the photoisomerization mechanism of azobenzene remains a subject of debate and the dominance of the isomerization mechanism in the n-π* and π-π* excited state is not fully clarified yet.

More recently, with the development of large scale photoresponsive materials and optical devices, a growing number of theoretical and experimental works [56-61, 63-65] of azobenzene have been exploited for supramolecular systems, linear macromolecules and polymers, such as bisazobenzene, multiazobenzene and azopolymers where the parent azobenzene is incorporated into macromolecular systems.

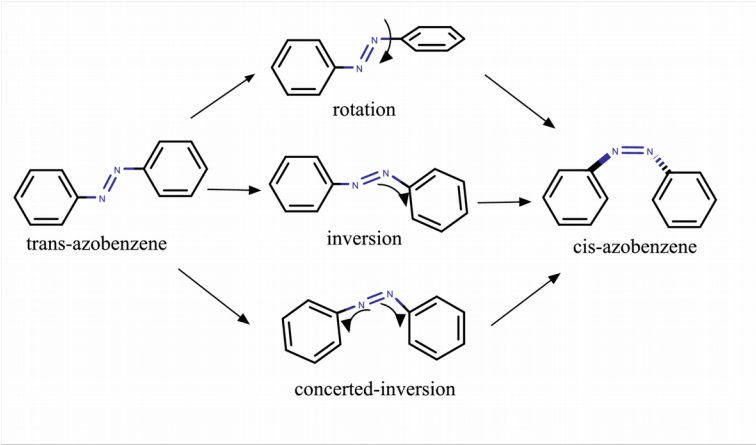

Figure 3.1: Schematic description of three isomerization mechanisms of azobenzene.

The incorporation of photochromic azobenzene or multiazobenzenes in macromolecules and polymers has been used to develop new photoresponsive molecular electronics and multiphotochromic devices [65-66]. However, so far, in contrast to the extensive research on the parent azobenzene, only a few studies [56-66] focused on photochemical properties and the isomerization mechanism of multiazobenzenes. Previously, *Blége et al.* demonstrated that in multiazobenzene the individual switches become independent of each other when the N=N double bonds are attached to the *meta* position of the phenyl rings [58]. *Floss* and *Saalfrank* [57] studied the photoinduced *trans*→*cis* isomerization of *meta*- and *para*-bisazobenzene by employing a surface hopping molecular dynamics approach. The quantum yields for photoswitching of *p*-bisazobenzene decrease because of the electronic coupling of both individual AB-units, while *meta*-bisazobenzene displays significantly decoupled electronic subsystems, thereby improving the quantum yields of multiazobenzene switches. Recently, *Slavov* and co-workers [59] investigated the ultrafast dynamics of *ortho-, meta-* and *para*-bisazobenzenes by femtosecond transient absorption spectroscopy and time-dependent density functional theory (TDDFT). The transient absorption spectra of *m-bis*(AB) indicated a similar behavior comparing to the monomeric AB, and the two AB units isomerized nearly completely independently from each other. In contrast, a unique interaction between the two individual AB units was observed in the case of the *o-bis*(AB) due to the intramolecular exciton coupling. As expected, *p-bis*(AB) presented a

highly conjugated π-system extending over the whole molecule, leading to strong planarity of the molecule and consequently low isomerization quantum yields. Not surprisingly, azo-based conjugated systems are expected to have potential use in various research areas, e.g, as π-conjugated semiconductors with narrow energy gaps and conducting materials [10]. However, a clear understanding of the isomerization process of multiazobenzenes is still not available.

Although many previous experimental and theoretical results are available for the isomerization process, an explicit interpretation of the isomerzation mechanism in the nπ* and the ππ* excited states is a long-standing debate. So far, only a few theoretical calculations and experiments involved the photoresponsive properties and the isomerization mechanism of multiazobenzenes. At present, it is possible to make a hypothesis of possible isomerzation pathways for multiazobenzenes on the basis of existing studies of the parent azobenzene. Naturally, a new viewpoint on the isomerization mechanism of multiazobenzene shall be beneficial to further understanding of the isomerization mechanism of the parent azobenzene. Thus, to study and unravel the photochemical behavior and the isomerization mechanism of multiazobenzenes will not only provide a deeper insight into the photoisomerization process of azobenzene, but also meet the demand for various invaluable photo-responsive macromolecular electronics, light-controlled molecular devices and optomechanical devices or photoresponsive polymers.

In this chapter, I will show a detailed study of the absorption spectra of linear multiazobenzenes with different lengths and scans of the potential energy surfaces of the relevant excited states for a fundamental understanding of the isomerization process. An accurate calculation of the electronic spectra of linear multiazobenzenes provides a better understanding of how the chain length affects excitation energies and how the combination of azo groups lowers excitation energies. With respect to the accuracy of the excitation energy, I evaluated the TDDFT [37, 48-49] excitation energies of low-lying excited states and the corresponding excitation energies agree well with results obtained from the algebraic diagrammatic construction (ADC) [40-42, 91-94] calculations as well as the experimental data. Consequently, I performed DFT

calculations to optimize the geometry of the ground state and carried out TDDFT calculations for excited states of AB-(n) with different chain lengths along three different reaction pathways, *e.g.* the CNN bending (inversion), the CNNC torsion (rotation), and the concerted CNN bending (the concerted inversion*)* pathways. Such investigations of the potential energy surface are able to provide remarkable insight in which isomerization mechanism accounts for the isomerization process and show whether an energy barrier is involved along the reaction coordinate. Based on my calculations, the photochromic behavior and the preferred photoisomerization pathway in the ground and excited state of AB-(n) with different lengths are discussed. In addition, the comparison of isomerization mechanisms of the same multiazobenzene with different twisted geometries along different reaction pathways will be addressed in the following section.

3.2 Computational Methods

To identify an effective and practical excited state method, several different electronic structure methods ranging from time-dependent Hartree Fock theory (TDHF) [182-184] to the highly accurate ADC [40-42] method were evaluated in conjunction with a series of basis sets developed by *Pople* [185-186]. The ground state geometry optimizations were performed employing density functional theory. Then, the vertical excitation energies of the stable *trans*- and *cis*-isomers of azobenzene were calculated using various quantum chemical methods to make a comparison with experimental data as well as other previous theoretical calculations [3, 26, 29]. Based on my calculations and the comparative analysis, my choice was to use the computationally practical and reliable BHHLYP [141] functional together with the 6-31G* basis set [185], which was found to be able to reproduce excitation energies with sufficient accuracy.

Hence, the geometries of the ground state and the S_1 excited state of AB-(n) were optimized at the TDDFT/BHHLYP level of theory using the 6-31G* basis set. TDDFT

calculations were performed for simulations of the potential energy surface along different isomerization pathways of the AB-(n)s, aiming at robust explanations of the isomerization mechanism and novel isomerization features. Thus, the relaxed potential energy surface starting from the optimized S_1 geometry were performed by scanning different reaction coordinates.

It should be noted that different twisted positions may lead to different favorable isomerzation pathways. A numbering system of the AB-(n) is shown in Fig. 3.2 and possible twisted positions in the chain are marked with T1, T2 and T3, respectively. Thus, the influence of the twisted position of AB-(n) on the isomerization mechanism will be addressed. Taking the AB-(3) as example, I present the difference of the AB-(3) twisted positions by means of the PES along different pathways to provide an illustrative diagram of the isomerization process between two torsional AB-(3) models as well as to understand the coupling interaction of two azo moieties.

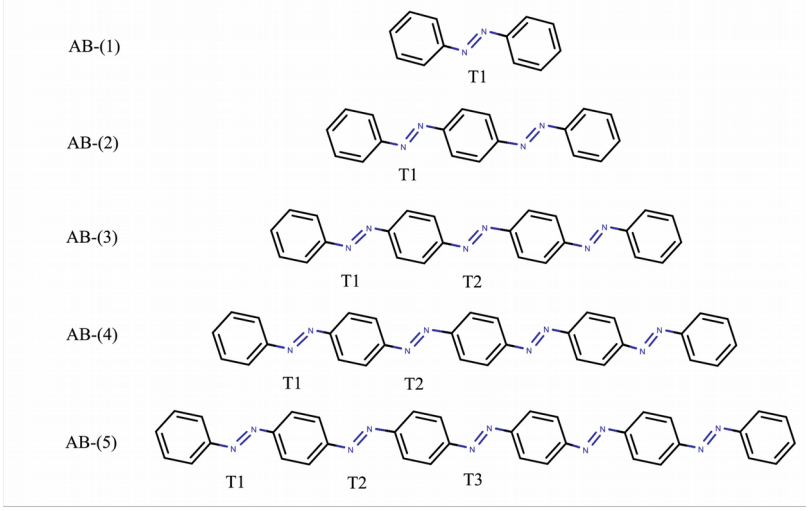

Figure 3.2: Structure and numbering system of AB-(n)s. AB-(n) represents the number of N=N double bonds included in the azobenzene chain.

In addition, it is commonly known that an accurate description of the seam space of a conical intersection of excited states is considered to be a bottleneck for single-reference

methods in quantum chemistry. However, the conical intersection as well as accurate excitation energies are here obtained by TDDFT calculations which have thus proven to deliver qualitatively correct results compared to experimental data and other theoretical calculations [3, 26, 57-60]. Specifically, the geometry optimization and the excitation energy calculations employing TDDFT in this work are quite accurate and reliable. Therefore, the absorption spectra calculations of AB-(n) were performed with TDDFT calculations. The *Tamm-Dancoff* approximation (TDA) technique [147] was employed for PES calculations based on the TDDFT method. All *ab initio* calculations for AB and AB-(n) were carried out with the Orca 3.0 package [176] and the Q-Chem 4.3.0 package [177].

3.3 Vertical excitation energies of linear azobenzenes

For comparison, the geometry optimization of the ground state and the vertical excitation energies of azobenzene were calculated with the B3LYP functional and a series of different *Pople* basis sets as presented in Table 3.1. It is found that in all cases the 6-31G* basis set yields remarkably accurate excitation energies in accordance with larger basis sets, and thus I adopted the smaller but more efficient basis set to perform the subsequent geometry optimizations and excitation energy calculations for AB and AB-(n).

The vertical excitation energies of the ground state equilibrium structures of trans- (TAB) and cis-azobenzene (CAB) evaluated at different theoretical levels of theory are listed in Table 3.2 together with the experimental values. In addition, calculations based on the TDDFT and the TDHF methods with a conductor-like polarizable continuum model (C-PCM) [95-97] for ethanol (dielectric constant ε=24.5) have been considered as well. Moreover, some excitation energies of *trans*- and *cis*-azobenzene from other theoretical calculations as reference (e.g CASSCF [29, 43-44]) are quoted to compare them to the TDDFT results. As proposed in literature [29, 32], the first excited state can

be characterized as a n-π* state while the second transition is assigned to an π-π* transition. Due to the important role of the first n-π* and π-π* states in the isomerization process of azobenzene, their vertical excitation energies have been calculated for benchmarking purposes with various electronic structure methods in comparison with the experimental data.

As clearly shown in Table 3.2, it is found that the first and second excitation energies of *trans*- and *cis*-AB calculated via the TDHF approach are all too large in both gas phase and solution compared with the experimental data. On the contrary, the BLYP [139, 148] functional yields relatively low excitation energies for the S_1 and S_2 states. This is clearly implying that both approaches are not suited. On the other hand, excitation energies computed with CCSD [38] are very close to the experimental values. Particularly, ADC(2) tends to provide accurate results for *trans*- and *cis*-AB in excellent agreement with the experimental data in the gas phase.

However, calculations with both latter approaches are rather expensive from a computational point of view. In contrast, both conventional hybrid functionals B3LYP [44, 140, 187] and BHHLYP provide not only accurate vertical excitation energies for *trans*- and *cis*-AB, and offer a time-saving computational strategy. Specifically, BHHLYP seems to be more balanced for vertical excitation energies of the two isomers in the gas phase and in solution. Moreover, one notices that CASSCF [29] yields a reasonable S_1 excitation energy compared to the experimental data while a larger deviation is found for the S_2 excitation energy in both isomers. Although CASSCF is confirmed to be able to describe the conical intersection well, however, it is not likely to offer a good compromise between accurate excitation energies and computational effort. According to the comprehensive analysis above, the BHHLYP/6-31G* scheme can provide accurate and reliable vertical excitation energies with respective to the experimental data for optimizing the excited state geometry and relaxed PES scans in the S_1 excited state.

Basis set	S_1		S_2		S_3		S_4	
	gas	ethanol	gas	ethanol	gas	ethanol	gas	ethanol
6-31g	2.3286	2.3845	3.7853	3.5696	4.0993	3.9762	4.1023	3.9762
6-31g*	2.5541	2.5945	3.7724	3.5740	4.1070	4.0055	4.1086	4.0064
6-31g**	2.5520	2.5912	3.7739	3.5728	4.1114	4.0074	4.1129	4.0085
6-311g	2.3662	2.4220	3.7606	3.5508	4.0871	3.9668	4.0886	3.9679
6-311g*	2.5477	2.5866	3.7632	3.5643	4.1011	3.9994	4.1011	4.0017
6-311g**	2.5396	2.5811	3.7630	3.5689	4.1069	4.0082	4.1073	4.0106
6-31+g	2.3961	2.4550	3.6906	3.4700	4.0330	3.8947	4.0336	3.8962
6-31+g*	2.5716	2.6138	3.6707	3.4670	4.0354	3.9196	4.0366	3.9228
6-31+g**	2.5684	2.6103	3.6714	3.4651	4.0384	3.9209	4.0397	3.9240
6-31++g	2.3969	2.4556	3.6912	3.4700	4.0331	3.8948	4.0331	3.8963
6-31++g*	2.5716	2.6139	3.6715	3.4671	4.0358	3.9193	4.0366	3.9227
6-31++g**	2.5677	2.6103	3.6691	3.4663	4.0363	3.9211	4.0374	3.9241
6-311+g	2.3948	2.4510	3.7097	3.4930	4.0548	3.9211	4.0549	3.9229
6-311+g*	2.5554	2.5964	3.6991	3.4990	4.0565	3.9463	4.0582	3.9504
6-311+g**	2.5474	2.5899	3.6992	3.5000	4.0613	3.9517	4.0635	3.9553
6-311++g	2.3952	2.4512	3.7103	3.4929	4.0544	3.9211	4.0547	3.9226
6-311++g*	2.5557	2.5966	3.6985	3.4992	4.0561	3.9462	4.0580	3.9497
6-311++g**	2.5477	2.5901	3.6991	3.4996	4.0611	3.9516	4.0634	3.9553
cc-pVDZ	2.5371	2.5769	3.7629	3.5737	4.1031	4.0126	4.1033	4.0149
cc-pVTZ	2.5343	2.5806	3.7652	3.5674	4.1197	4.0169	4.1216	4.0207
aug-cc-pVDZ	2.5436	2.5880	3.6618	3.4644	4.0282	3.9206	4.0306	3.9250
aug-cc-pVTZ	2.5247	2.5701	3.7204	3.5214	4.0903	3.9831	4.0927	3.9877
Expt.1	2.82	2.79	4.12	3.95				
Expt.2		2.81		3.94				

Table 3.1:The first four vertical excitation energies of trans-azobenzene at TDDFT/B3LYP level with a series of Pople basis sets. Expt.1 and Expt.2 are taken from references 3, 26 and 59.

TDHF		B3LYP		BHHLYP		BLYP		CCSD		ADC(2)S		CASSCF		Expt.	
GAS	C-PCM	GAS	C-PCM	GAS	C-PCM	GAS	C-PCM	GAS	C-PCM	GAS	C-PCM	GAS[a]	C-PCM	GAS[b]	solution[c]
T-AB															
3.22	3.25	2.56	2.63	2.91	2.95	2.22	2.31	3.05	/	2.96	/	2.85	/	2.79	2.81
4.62	4.46	3.90	3.72	4.28	4.09	3.58	3.41	4.79	/	4.50	/	7.62	/	3.95	3.94
C-AB															
3.15	3.22	2.62	2.69	2.85	2.92	2.43	2.49	3.09	/	3.01	/	3.65	/	2.82	
5.53	5.41	4.25	4.10	4.96	4.81	3.59	3.48	4.98	/	4.88	/	8.62	/	4.77	

[a] *Taken from reference 29.* [b] *Taken from reference 3.* [c] *Taken from reference 59.*

Table 3.2: Comparison of the vertical excitation energies (eV) of trans- and cis-azobenzene using different approaches in the gas phase and in solution (ethanol).

The ground state structures of AB-(n) were optimized at the DFT/ BHHLYP/6-31G* level of theory followed by the calculation of the lowest n-π* and π-π* singlet excitation energies. The calculated vertical excitation energies of TAB-(n) and CAB-(n) are summarized in Table 3.3. The vertical excitation energies of all excited states of *trans*- and *cis*-AB-(n) decrease with increasing chain length. Specifically, the excitation energy steeply declines at the beginning from AB-(1) to AB-(2) and continues with a minor decrease in the excitation energy when going from AB-(2) to longer chains. This behavior implies that the π-π* transition is more affected by the enhanced conjugated π-system than the n-π* transition. When the conjugated π-system is extended, the excitation energies are lowered. Also, the oscillator strengths of the π-π* state of TAB-(n) and CAB-(n) become larger and the magnitude of the oscillator strength is roughly linearly dependent on the number of n, particularly in the case of TAB-(n). This is because the lowest π-π* transition is delocalized over the whole molecule and the conjugated π systems are strengthened by an increase in chain length. As a result, the overall intensity of the π-π* transition AB-(n) (n>1), which contains a number of sub-azo units, exhibits a superposition of the π-π* transition intensities of different sub-azo units, thus indicating dependence on the chain length. In addition, it should be noted

that the order of the electronically excited states of TAB is not conserved and the first lowest π-π* excited state shifts to the higher excited state with growing chain length. The change of the order is also consistent with the fact that the overlap of the intensity of the π-π* transition of several azo units occurs in TAB-(n) while it possesses a certain number of individual low-lying n-π* states simultaneously.

	T-AB-(1)	T-AB-(2)	T-AB-(3)	T-AB-(4)	T-AB-(5)	Expt.[a]
$n - \pi^*$	2.91 (0.0000)	2.83 (0.0000)	2.79 (0.0000)	2.77 (0.0000)	2.77 (0.0001)	2.79
$\pi - \pi^*$	4.28 (0.8351)	3.63 (1.6608)	3.32 (2.4796)	3.15 (3.2766)	3.05 (4.0709)	3.95
	C-AB-(1)	C-AB-(2)	C-AB-(3)-T1	C-AB-(4)-T1	C-AB-(5)-T1	
$n - \pi^*$	2.86 (0.0257)	2.80 (0.0790)	2.78 (0.1562)	2.77 (0.2518)	2.77 (0.2944)	2.82
$\pi - \pi^*$	4.97 (0.1957)	4.01 (1.0008)	4.00 (1.7557)	3.27 (2.4804)	3.13 (3.1660)	4.77
			C-AB-(3)-T2	C-AB-(4)-T2	C-AB-(5)-T2	
$n - \pi^*$			2.73 (0.1540)	2.72 (0.2458)	2.71 (0.3367)	
$\pi - \pi^*$			3.86 (1.0992)	3.50 (1.7400)	3.26 (2.4148)	
					C-AB-(5)-T3	
$n - \pi^*$					2.70 (0.3425)	
$\pi - \pi^*$					3.43 (1.7454)	

[a] *taken from reference 3 for T-AB.*

Table 3.3: Comparison of vertical excitation energies (eV) of trans- and cis-azobenzene chain with different lengths at the TDDFT/BHHLYP/6-31G level of theory. Oscillator strength is given in parentheses.*

To explore the effect of the trans-cis isomerization on the excitation energies of CAB-(n) in more detail, the lowest n-π* and π-π* vertical excitation energies of different CAB-(n) isomers were calculated. As shown in Table 3.3, both n-π* and π-π* excitation energies decrease as the N=N double bonds of CAB-(n) are twisted at the

same position $\mathbf{T_x}$, where x refers to the *x*-th isomerized N=N double bonds in the chain. In addition to the case of CAB-(3), the n-π* excitation energies of CAB-(n) decrease slowly and the π-π* excitation energies increase steadily with isomerized position from one side to the center of the chain. Notably, the intensity of the π-π* band in the case of CAB-(5) decreases when the twisted position moves from one side to the center, accompanying a significant decline of the conjugated π-electron system. Moreover, a drastic rise of the intensity in the π-π* band with increasing chain length is generally observed in CAB-(n), which can be ascribed to the contribution of the larger *trans*-segment of longer CAB-(n).

3.4 Absorption spectra and Excitonic coupling

The absorption spectra of TAB-(n) with different chain lengths up to AB-(5) are shown in Fig. 3.3. The spectrum of TAB-(2) shows a strong π-π* absorption band at ~342 nm, and its oscillator strength is twice higher than that of the parent TAB. The π-π* absorption band is significantly red-shifted by ~50 nm with respect to ~295 nm of AB due to an increase in the conjugation of the π-system. Apparently, the red-shift and the oscillator strength of the π-π* band of a series of TAB-(n) is drastically increased with growing chain length. On one hand, this can be explained by the lengthened conjugated π-system extending over the entire molecule. Such a conjugated π-system immediately leads to a lower π-π* excitation energy. On the other hand, the oscillator strength of the strongest π-π* absorption peak rises roughly in proportion to the increase in chain length, which accounts for the presence of several repeated AB units as well as a superposition of the absorption intensity. Moreover, the red-shift in the π-π* band of AB-(2) was found to be in agreement with other theoretical and experimental data [57-58]. All theoretical results once again confirm that the chosen approach provides convincing excitation energy calculations for absorption spectra and it is reasonable to expect also accurate results for longer AB-(n).

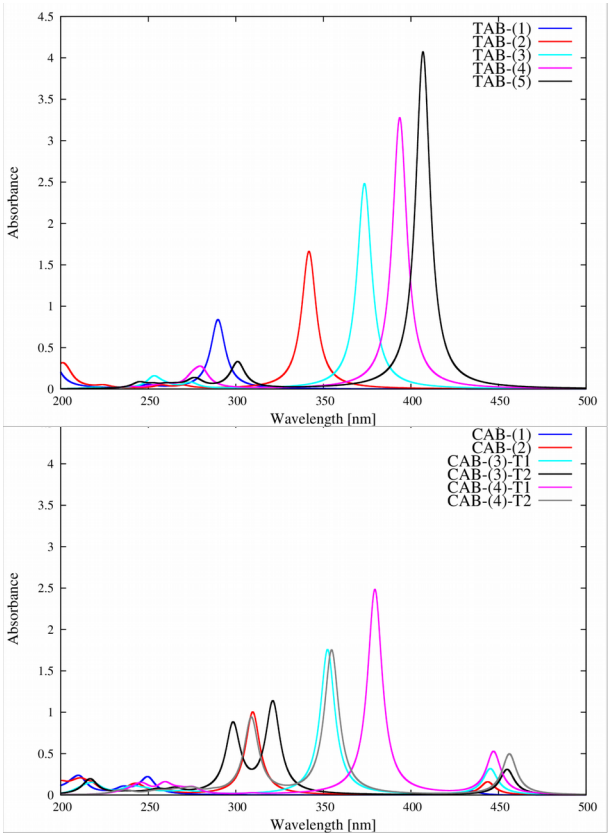

Figure 3.3: Absorption spectra of the trans- and cis-azobenzene chains (TAB-(n) and CAB-(n)) with increasing lengths n at the TDDFT/BHHLYP/6-31G level of theory.*

More interestingly, in addition to a minor red-shift of the n-π* excitations of CAB-(n)s, a strong π-π* absorption band with increasing chain length was observed as a result of the existence of the TAB moiety in the chain as shown in the Fig. 3.3 (bottom). The red-shift of the π-π* band of CAB-(n) displays a similar behavior as that of the TAB-(n), differing in intensity. Furthermore, some significant spectral features are observed in the n-π* and π-π* transition bands due to different twisted positions, which have not been reported previously. The spectral displacement of the n-π* band shows a strong dependence on the position of the isomerized N=N bond. That is, when the *cis*-bond is at the end of the chain, represented by **T1,** the spectrum of the CAB-(n) always exhibits a slight red-shift in the n-π* absorption band with respect to the parent CAB. In contrast, the red-shift is relatively large in comparsion with that of CAB-(n)-**T1** as the twisted position is close to the center of the chain. Essentially, this difference in the n-

π* band relates to the conjugated π system of CAB-(n). Aside from the spectral shift, the oscillator strength of the n-π* band increases steadily with increasing chain length as well. Moreover, it should be noted that an interesting dual band appears in the π-π* absorption band, which may be ascribed to the electronic interactions of two neighboring AB units as well as the strong excitonic coupling between the interacting transition dipole moments oriented along two axes of the molecule. Obviously, when the twisted position gets closer to the center of a chain, the excitonic coupling between the π-π* and n-π* transition dipole moments of two neighboring moieties becomes stronger, leading to a higher and a lower transition. According to the excitonic coupling theory developed by *Kasha* [189], interactions of the transition dipole moments lead to a lower energy transition and a higher energy transition. At this point, it makes sense to interpret the spectral changes as caused by excitonic coupling when the isomerization occurs at different position of AB-(n). The magnitude of the coupling is proportional to the increase in the square of oscillator strengths, which provides an opportunity to determine the spectral change introduced by excitonic coupling [189-192]. I will clarify the effect of excitonic coupling on the spectral change taking CAB-(5) as an example in the following section.

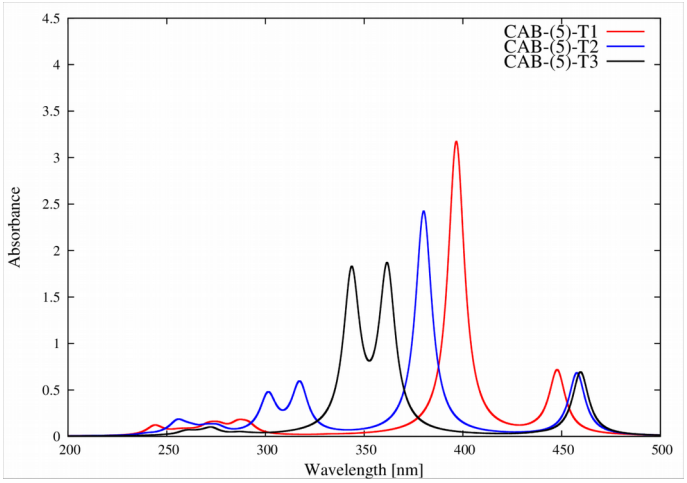

Figure 3.4: Absorption spectra of the three different cis-AB-(5) isomers at the TDDFT/BHHLYP/6-31G level of theory.*

The spectra of the n-π* and π-π* absorption bands of CAB-(5) with the isomerized N=N bond at **T1**, **T2** and **T3**, are shown in Fig. 3.4, respectively. The spectra of CAB-(5) with **T1** and **T2** have no direct evidence of splitting in the π-π* absorption band, even though the twisted position **T2** gets closer to the center of the chain. This is because the π-π* transition dipole moment of the shorter moiety is too small compared to that of the longer moiety. As expected, the absorption spectrum of CAB-(5) at **T3** shows a prominent dual π-π* band with roughly identical intensity, revealing a strong exciton coupling between two closely connected AB-(n) units. In addition, the similar spectral changes of CAB-(5) between **T1** and **T3** were also found in the case of CAB-(3) and CAB-(4) between **T1** and **T2**. Apparently, such difference in the π-π* absorption band between **T1** and **T3** twisted isomers relates to the chain length of the two AB-(n) moieties. As seen in Fig. 3.4, the spectral feature of **T1** and **T2** demonstrates the superposition of the π-π* absorption bands of two individual AB-(n) moieties, which implies a weak excitonic interaction between two moieties, since the two distinct transition dipole moments only present J-type interaction behavior along the longer molecular axis. In contrast to the splitting in the π-π* band of CAB-(3)-**T2** and CAB-(4)-**T2**, the feature of the dual band is more obvious in the case of CAB-(5)-**T3.** This suggests the exciton interaction to be dominated by the structural change and the chain length of the two individual AB-(n) moieties. Once two identical transition dipole moments along two molecular axes within one molecule are coupled to each other, the main π-π* absorption band will split into an allowed lower energy transition and a higher energy transition, that is, a red-shifted band and a blue-shifted band. In general, the excited state is considered to be equally delocalized over the two AB-(n) moieties when the intramolecular exciton coupling occurs. However, it should be noted that the exciton coupling mechanism between the two adjacent AB moieties of the CAB-(n) is only valid if both moieties are approximately equal. Otherwise, no significant dual band appears in the π-π* absorption spectrum of CAB-(n). In addition, by increasing the chain length, the absorption peak of the π-π* band of the TAB-(n) gradually gets closer to that of the n-π* band of CAB-(n). In this sense, AB-(n) seems not suitable for normal photo-switches relative to the parent AB, but fit for the

development of optical sensors, photo-detectors, conducting materials and semiconductor molecules, due to its highly linear π conjugated system.

3.5 Potential energy surfaces along three isomerization pathways

In this section, the potential energy surfaces based on optimized geometries of the first excited state for AB-(n) along rotation, inversion, and concerted-inversion coordinates were performed using TDDFT. For a better understanding of the influence of isomerized position on the mechanism of azobenzene chains, the relaxed potential energy surfaces of AB-(3) have been calculated at the two different positions (**T1** refers to the position of the double N=N bond on one side of the AB-(3) chain and **T2** represents the middle N=N double bond of the chain).

3.5.1 Rotation pathway

The torsional potential energy curves computed for the ground state and the first four excited states along the CNNC dihedral angle are shown in Figure 3.5. The optimization of the lowest S_1 state has been performed at each value of the CNNC angle, followed by subsequent excitation energy calculations. The calculated potential energy surface of AB is found to be in good general agreement with many previous calculations. The most stable geometry of all values of CNNC dihedral angles was found to be at 180° in all cases. The peak of the energy barrier along the rotation pathway is located at a dihedral angle of 100° as seen in Fig. 3.5. The graph indicates that the highest point on the potential energy surface of the ground state is close to a conical intersection of the ground state and the S_1 state at about 90°.

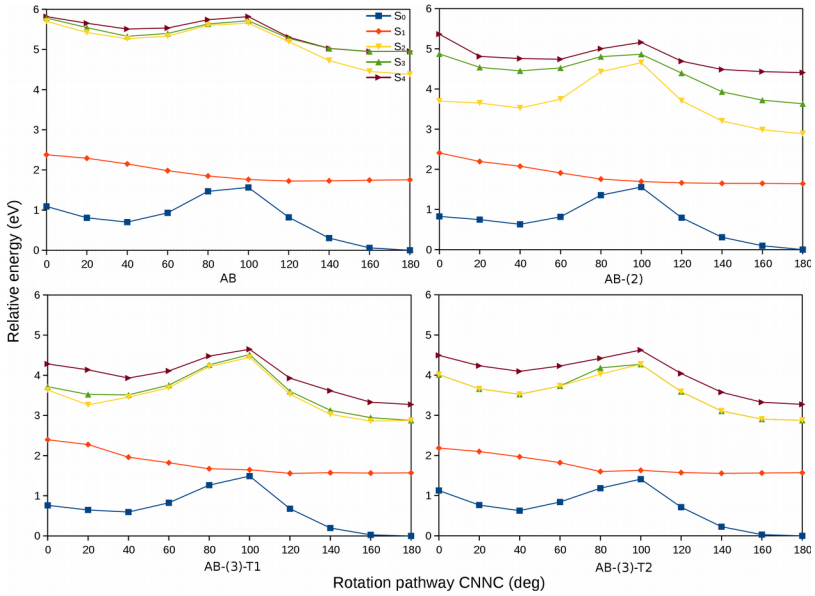

Figure 3.5: PES of the azobenzene chains (AB-(n)) along the CNNC dihedral angles at the optimized geometry of the S_1 state.

As can be seen in Fig. 3.5, all S_1 potential energy curves of AB-(n) exhibit a very similar behavior as the parent AB. Specifically, there is no energy barrier on the S_1 surface along the rotation pathway for all AB-(n), which is also in line with previous theoretical and experimental results. Subsequent n-π* excitation readily leads to a direct relaxation though a conical intersection from the first excited state to the ground state. The conical intersection between S_1 and S_0 along the rotation reaction coordinate can generally not be obtained since vertical excitations cannot be well described by TDDFT in the vicinity of conical intersections. However, the overall shape of the relaxed S_1 curves are quite similar for all AB-(n) and a conical intersection between the S_1 and the S_0 state is most likely to appear between a dihedral angle of 80° and 100° along the rotation pathway, even if the chain length is increased. It has been proposed [29, 31-32] that the S_1 PES along the rotation pathway has a conical intersection between the S_1 and S_0 as well as a barrierless S_1 potential surface, indicating that the isomerization takes place easily on the S_1 surface. Moreover, it is observed that the S_1 surface at the cis side in the first excited state is slightly higher in energy than at the trans side. Thus, after n-π* excitation, a rapid relaxation on the S_1 surface leads to the conical intersection from

the cis side faster than from the trans side, consequently leading to higher quantum yields for the trans isomer in the ground state. In addition, it is found that both the PES of AB-(3)-**T1** and AB-(3)-**T2** exhibit a similar trend with respect to AB, whereas the excitation energies of higher excited states decrease with increasing the chain length. Increasing chain strengthens the conjugated π-system, naturally lowering the excitation energy of higher excited states. Overall, my theoretical results suggest the isomerization mechanism to be in favor of the rotation pathway after excitation to the S_1 state.

3.5.2 Inversion pathway

Fig. 3.6 shows the potential energy curves of the ground state and the first four low-lying excited states along the inversion pathway for the AB-(n). The S_1 potential energy surface has a small energy barrier along the inversion reaction coordinate and no substantial difference among all cases of AB-(n) as shown in Fig. 3.6. Although the first excited state and the ground state potential energy curves get closer towards larger CNN angles, a conical intersection between the S_1 and the S_0 surfaces was not confirmed along the inversion pathway in all PES of AB-(n). I found that a shallow minimum of the S_1 potential surface is located above the minimum point of the ground state at a CNN angle of ~130°. The potential energy curves of the higher excited states S_2, S_3 and S_4 decline with increasing chain length. In particular, the potential surfaces of these higher excited states descend above the area of the shallow minimum of the S_1 surface leading to a small energy gap between the S_1 and S_2 surfaces. That is, the relaxation of the S_2 excited state to the S_1 state occurs in the vicinity of this deep minimum of the S_2 surface, which can help the molecule to get over the potential barrier on the S_1 surface. However, there is no easily accessible conical intersection between the ground and the first excited state along the minimum energy inversion pathway for all AB-(n). Therefore, the inversion pathway seems to be less energetically favorable compared to the rotation pathway.

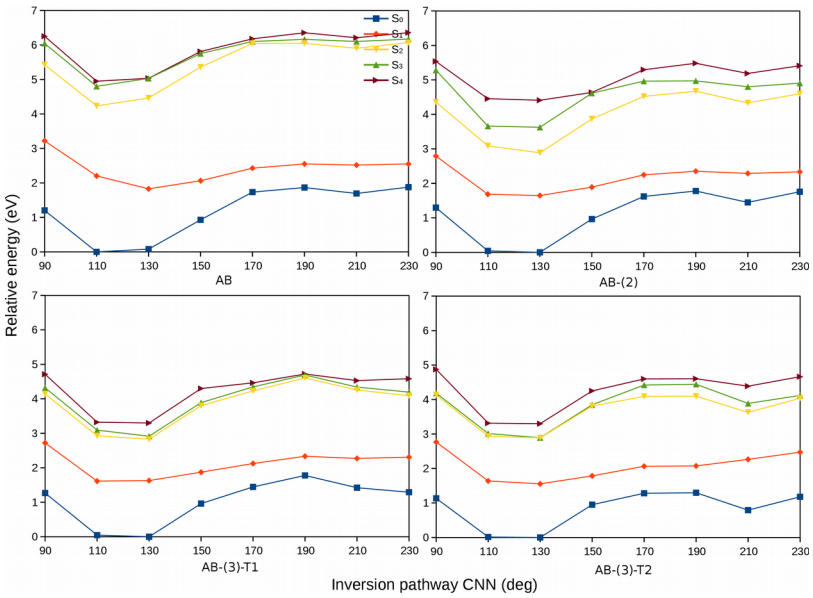

Figure 3.6: Inversion PES of the azobenzene chains (AB-(n)) along the CNN angle at the optimized geometry of the S_1 state.

3.5.3 Concerted-inversion pathway

The relaxed potential energy surfaces along the concerted-inversion CNN angle of the ground state and the first four excited states of AB-(1), AB-(2) and AB-(3) are presented in Fig. 3.7. The potential curves of the AB-(n) were obtained by scanning both CNN angles as well as relaxing the geometry in the S_1 state. As seen in Fig. 3.7, the minor energy gap at concerted CNN angles, between 170° and 190°, significantly indicates the presence of a conical intersection between the ground and the S_1 state in all cases. Interestingly, a higher potential energy barrier along the concerted-inversion pathway was observed compared to the inversion pathway.

Similarly, the excitation energies of higher excited states decrease with an increase in chain length. The global minimum of the S_2 potential surface is found at the region of concerted CNN angles between 110° and 130°. At this region, the energy gap between the S_2 and the S_1 surfaces becomes smaller with increasing chain length. As a consequence, the rapid relaxation from high-lying excited states to the S_1 state can take place easily. Although there remains a relatively large potential energy barrier on the S_1

surface along the concerted-inversion pathway, the relaxation of the S_2 state to the S_1 state may introduce sufficient energy to overcome the potential barrier on the S_1 surface. Subsequently, the S_1 state spontaneously decays to the ground state through a conical intersection between the S_1 and the S_0 state. Eventually, once excited to the S_2 state, the concerted-inversion channel may be opened in the photoisomerization process. In particular, the potential energy surfaces of the higher excited states decrease steeply at the global minimum of the S_2 surface with increasing chain length. This is, when excited to these higher excited states, longer AB-(n) have a higher probability to relax to the lowest S_1 state, probably undergoing vibrational transitions already in the Franck-Condon region [193], and rapid relaxation from these higher excited states to the S_1 state helps to overcome the potential barrier on the S_1 surface. Nevertheless, my calculations indicate that the concerted-inversion pathway should be highly favored when the molecule is excited to the S_2 or even higher excited states.

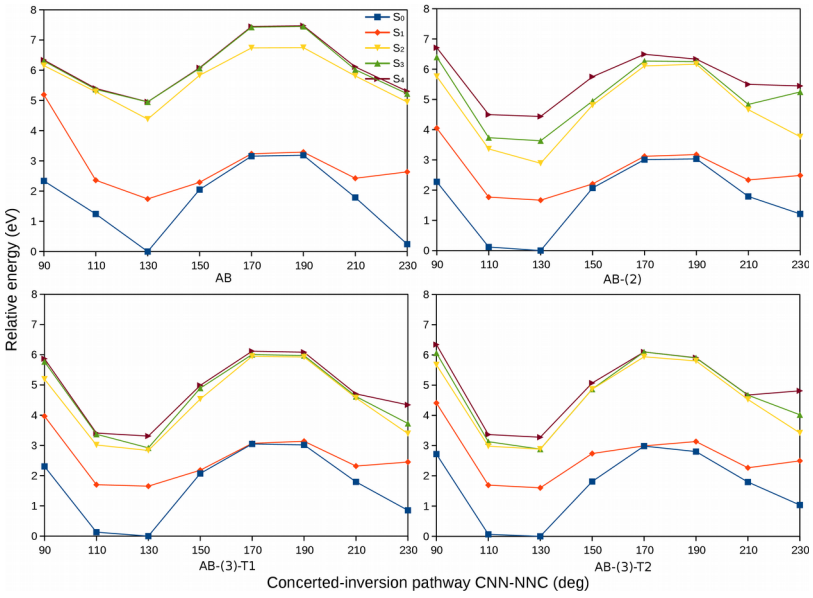

Figure 3.7: Concerted inversion PES of the azobenzene chains (AB-(n)) along the concerted CNN angles at the optimized geometry of the S_1 *state.*

3.6 Conclusion

Herein, the vertical excitation energies of the lowest n-π* and π-π* states and the potential energy surface of azobenzene chains in the first excited state have been investigated using TDDFT. First, I benchmarked TDDFT calculations compared with several reliable *ab initio* wavefunction methods. By comparing the theoretical and experimental data, the TDDFT method using the BHHLYP functional and the 6-31G* basis set turned out to be efficient and accurate enough for the desired excitation energy calculations. It was found that the order of the low-lying excited states is changed by increasing chain length while all excitation energies decrease, but to different degrees.

Next, the absorption spectra of AB-(n) provide interesting insight into the excitonic coupling mechanism of twisted AB-(n). The strong excitonic coupling between two equally connected AB-(n) moieties appears in twisted AB-(n)s, leading to a significant dual band in the π-π* absorption band. In addition, the red-shift in the π-π* band of a series of AB-(n) including not only TAB-(n) but CAB-(n) gradually increases with increasing chain length, since with increasing chain length the conjugated π-system of AB-(n) becomes larger.

Furthermore, potential energy curves along the rotation pathway, inversion pathway and the concerted-inversion pathway have been computed for the AB-(n)s to explore the isomerization mechanism of AB and AB-(n). The results show that the S_1 potential surface of AB-(n) is essentially barrierless along the rotation pathway and a conical intersection is most likely to appear near the area between a dihedral angle of 80° and 100°. In general, the rotation mechanism was found to dominate the isomerization in the n-π* state. Athough a large potential barrier was found in the S_1 potential energy surface along the concerted-inversion pathway, rapid relaxation to S_1 state is expected to help overcome the potential energy barrier when originally excited to the S_2 state or higher excited states. However, the energy gap between the S_2 state and the S_1 state becomes relatively small with increasing chain length. Overall, the concerted-inversion

pathway is considered to be an energetically favorable mechanism when excited to the π-π* state. Moreover, the relaxed potential energy curves along three different pathways of AB-(n) indicate that the concerted-inversion isomerization mechanism is significantly affected by the chain length in contrast to the other two mechanisms.

In short, studies of absorption spectra and potential energy surfaces of linear azobenzenes not only provide a comprehensive insight into photochromic properties and the isomerization mechanism, but also are of importance for a successful design of photo-responsive functional materials and biomolecules.

Chapter 4

Non-linear Multiazobenzene Compounds

4.1 Motivation and background

In the last chapter, aborption spectra and isomerization mechnism of a series of linear azobenzenes AB-(n) were studied. However, prospective multiphotochromic properties and an unique cooperative isomerzation behavior of non-linear coupled azobenzenes have only recently been exploited for potential applications in areas of nonlinear optics, liquid crystals, chemosensors and photochemical molecular switches [57-58]. It is worthwhile to note that bisazobenzenes comprised of two sub-azo units via a shared phenyl ring exhibit varying degrees of photoswitching efficiency between their *trans* and *cis* states in response to irradiation [57, 60]. Some recent studies have shown that *bis*-azobenzenes and their derivatives present fascinating multiphotochemical properties and isomerization behaviors compared to the parent azobenzene [56-61].

For example, the photoswitching and the photochromic characteristics of four *para*-bisazobenzene derivatives connected by an aryl-aryl linker between two azo moieties have been addressed in detail [58]. *Cisnetti* found that the spectral properties of the *meta*-bisazobenzene derivatives are quite similar to the single azobenzene while the *para*-bisazobenzene derivatives have a significant red-shift in the π-π* absorption band as well as a reduced efficiency for the light-driven *trans-cis* isomerization [60]. A similar behavior for *meta*-bis-azobenzene and *para*-bis-azobenzene has been demonstrated by *Floß* using surface hopping molecular dynamics [57]. One possible explanation for the spectral changes and the decreased photoreactivity in the case of *p*-bisazobenzene is the strongly conjugated π-system. The electronic coupling between two azo subunits may lead to the suppression of switching. More recently, an analysis of the ultrafast dynamics of *o-, m-* and *p*-bisazobenzenes reported by *Chavdar* et al. [59] revealed the photochromic properties and the quantum yields of bisazobenzenes to be closely related to the connectivity pattern of bisazobenzene. Interestingly, *ortho*-bis-azobenzene exhibits a significant dual band in the absorption spectrum, which is probably due to intramolecular excitonic coupling between its two azo subunits.

In addition to examples of substitued and unsubstituted *bis*-azobenzenes, a series of multiazobenzenes and their derivatives such as cyclotrisazobenzene [70-71], azobenzene dimer [72], *tris*-[4-(phenylazo)-phenyl]-amine [73-74] on a metal surface, and other oligomultiazobenzenes [75-78] have been theoretically and experimentally addressed. All above-mentioned work involved various types of multiple azobenzenes, simply for the sake of studying new multiphotochromic properties and the cooperative photochemical behavior of non-linear multiazobenzenes. However, absence of the switching behavior and multiphotochromic properties limits the development and wide spread application of photoswitchable multiazobenzenes in polymers [64], surface materials[10], and other macromolecular systems[62].

In the following sections, a robust understanding of the multiphotochromic properties and isomerization processes of non-linear multiazobenzenes, such as, *bis*-azobenzenes and *tris*-azobenzenes, will be developed. Similar to the calculations of the last chapter, a systematic investigation of spectral properties of various *bis*-azobenzenes to discuss the

photoswitching efficiency using the TDDFT method [37, 48] in conjunction with the conductor-like polarizable continuum model (C-PCM) [95-97] will be presented. Furthermore, I show an interesting triple multiazobenzene structure with threefold symmetry and study the absorption spectra of *tris*-azobenzene to explore its high photoswitching efficiency. A series of functional groups are chosen to be used for substituted *tris*-azobenzenes, aiming at an efficient separation of the absorption spectra with respect to each different individual azo subunit. Moreover, cyclotrisazobenzene (CTA) serves as an interesting class of azobenzenophanes and exhibits remarkably prospective multiphotochromic properties as well [70-71]. Here, explicit theoretical calculations using time-dependent density functional theory are performed to explain why no *trans-cis* isomerization of CTA was observed in the experiment [70].

4.2 *Bis*-azobenzene (*bis*(AB))

4.2.1 Computational method

Bis(AB)s, which contain two azobenzene units connected by a shared phenyl ring linker at the *ortho*, *meta,* and *para* position, show varied photochemical properties due to their different connection patterns. Following previous studies [56-61] of *bis*(AB) compounds, six possible structures were designed for *o-, m-* and *p*-bis(AB), taking the structural symmetry of the N=N double bond into account (See Fig. 4.1). However, only part of them are selected and investigated in detail to explore the multiphotochromism and unexpected interactions between two azo subunits of bisazobenzenes. In this section, the absorption spectra of AB and the *bis*(AB) structures have been calculated using time-dependent density functional theory (TDDFT) [37, 48] with and without a conductor-like polarizable continuum model (C-PCM) [95-97] for the gas phase and ethanol solvation (dielectric constant of ε=24.5).

To identify an appropriate approach for excited state calculations, the vertical excitation

energies of *trans*-azobenzene were evaluated using the TDDFT method at different theoretical levels of theory (BLYP [139,148], BHHLYP [141], B3LYP [140,187], TDHF [182-184]). TDDFT is frequently used to calculate excited states and also has been proven successful in calculating accurate excitation energies for azo compounds [32, 179]. For benchmark purposes, calculations with the algebraic diagrammatic construction scheme for the polarization propagator of second order (ADC(2)) [91-94] are used to evaluate TDDFT results.

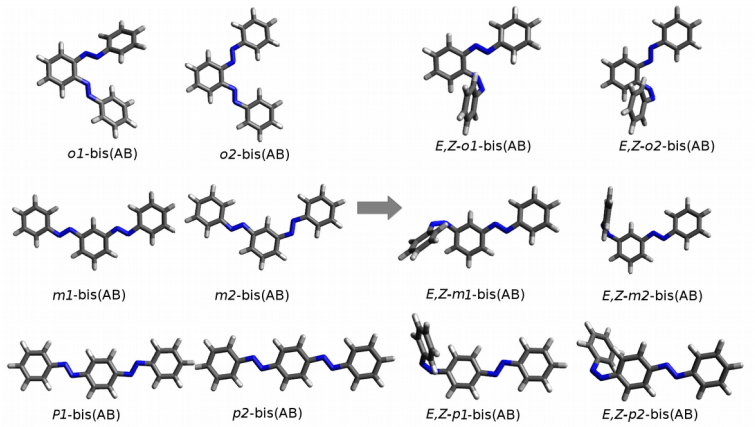

Figure 4.1: Structures of the investigated bis(AB)s (left) and their twisted bis(AB) isomers (right). The o1-, m1, p1-bis(AB) and o2-, m2, p2-bis(AB) are two different possible bis(AB) isomers, respectively. The singly twisted bis(AB) structures are labeled by E,Z-bis(AB).

The calculated vertical excitation energies for *E*-AB are shown in Table 4.1. It is found that the first (S_1) and second excitation energies (S_2) calculated using the BHHLYP functional in the gas phase and in ethanol are all quite close to the experimental values as well as previous theoretical data [3, 26, 32]. Meanwhile, it is demonstrated that TDDFT calculations in combination with the BHHLYP functional yield accurate excitation energies in good agreement with ADC(2) benchmark results. Therefore, TDDFT using the BHHLYP functional and the 6-31G* basis set [185] can provide

accurate and reliable excitation energy calculations regardless of calculations in the gas phase or in solvation.

Therefore, the ground state optimizations for AB and all *bis*(AB) models were performed using BHHLYP hybrid DFT method and excited state calculations were carried out at the TDDFT(BHHLYP/6-31G*) level together with the C-PCM model. All calculations have been performed with the Q-Chem 4.3.0 program package [177].

E-AB	BLYP		B3LYP		BHHLYP		TDHF		ADC(2)		EXPT.	
	GAS	C-PCM	GAS	C-PCM	GAS	C-PCM	GAS	C-PCM	GAS	C-PCM	GAS	Solution
S_1	2.23	2.29	2.56	2.60	2.91	2.93	3.25	3.26	2.99	/	2.82[a]	2.79[b]
S_2	3.36	3.19	3.78	3.58	4.28	4.09	4.80	4.65	4.35	/	4.12[a]	3.95[b]

[a] *Reference [26], in gas phase.* [b] *Reference [3], in ethanol.*

Table 4.1: Comparison of the vertical excitation energies of the lowest two excited states of E-AB using different approaches. The values are given in eV.

It has to be noted here that some of the information presented in this section has been previously published as:

Chavdar Slavov, Chong Yang, Luca Schweighauser, Chokri Boumrifak, Andreas Dreuw, Hermann A. Wegner, Josef Wachtveitl.

Connectivity matters - ultrafast isomerization dynamics of bisazobenzene photoswitches. Phys. Chem. Chem. Phys., **2016**, 18, 14795

4.2.2 Theoretical absorption spectra

The possible *E,E-* and *E,Z-bis(AB)* isomers are shown in Fig. 4.1, respectively. The theoretical absorption spectra of AB and *bis*(AB) structures in *E-* and *Z*-isomerization states are illustrated in Fig. 4.2. The absorption spectra of the *E,E-bis*(AB) for two different possible isomers were calculated. However, only the spectral feature of the *o-*

bis(AB) exhibits a significant difference between its two possible isomers. In contrast, the absorption spectrum of two possible isomers in the case of *m*- and *p-bis*(AB) behave very similarly. Hence, I will choose both structures of *o-bis*(AB) and one isomer of *m*- and *p-bis*(AB) to be discussed in this section. According to my calculations, it is found that the absorption spectra of AB and the *bis*(AB)s are consistent with the experimental data (see Fig. 4.3) [56, 59, 60]. One can easily observe that the positions of the theoretically calculated π-π* transition band of *E,E-bis*(AB) compounds are indeed fairly similar to the positions of the same transition in the experimental absorption spectra. The attachment and detachment densities for the four lowest singlet states of the different *bis*(AB)s indicate the character of the electronic transitions (Fig. 4.4 and 4.5).

The theoretical absorption spectra of *E,E-o-bis*(AB) show a large deviation in comparison with *E*-AB. A significant dual band was observed in the absorption spectra of *E,E-o-bis*(AB) in the π-π* transition range (at 278 nm and 313 nm for *E,E-o1-bis*(AB), and at 293 nm and 336 nm for *E,E-o2-bis*(AB)). The dual band of *o1-bis*(AB) exhibits two different π-π* bands with unequal height, whereas the two π-π* bands of *o2-bis*(AB) have roughly identical absorption peaks. This remarkable spectral feature of *o-bis*(AB) could possibly be considered to be due to the interaction between the two AB moieties. The *o-bis*(AB) model can be regarded as a combination composed of two identical and non-conjugated azo subunits. The transition dipole moments oriented along two different axes of the molecule strongly interact with each other. As a consequence, intramolecular exciton coupling may occur between the π-π* transition dipole moments of two azo subunits. Due to the exciton coupling, the original π-π* transition band splits into a higher and a lower transition band represented as splitting bands in the absorption spectrum. This might be the main reason why both isomers of *o-bis*(AB) have a significant dual band feature in the π-π* transition band.

However, the dual band of two possible isomers of *E,E-o-bis*(AB) behave differently. This is because the non-planar configuration of *E,E-o1-bis*(AB) has a more parallel orientation of the transition dipole moments along two axes of azo subunits, generating two excitonic bands with an upper and a lower intensity. This effect might be intensified by the presence of interactions between the electron clouds of two neighbouring N=N

groups. Conversely, the orientations of two π-π* transition dipole moments in the planar configuration of *o2*-bis(AB) are less parallel, which accounts for a more equal intensity of the two excitonic bands. The planar configuration enhances the conjugated π-system and thereby also contributes to the large red-shift of the lower π-π* transition band. Overall, the excitonic coupling interaction between two nearly equal transition dipole moments along orientation of two *o-bis*(AB) azo subunits results in the splitting of the π-π* transition band. Furthermore, the absorption spectra of *E,Z-o-bis*(AB) for the two possible isomers are obviously different if one of the azo subunits is switched by irradiation. The *trans-cis* isomerization of *E,Z-o-bis*(AB) destroys the excitonic coupling between the two azo subunits, leading to the presence of the typical π-π* transition band (~310 nm) and n-π* transition band (~425 nm) of AB instead of the corresponding dual excitonic band. In addition, it is shown that the absorption spectrum of *E,Z-o2-bis*(AB) resembles the sum of the monomeric *trans*- and *cis*-AB absorption spectra.

Apparently, the theoretical absorption spectra of *m-bis*(AB) are in excellent agreement with the experimental data (see Fig. 4.2 and 4.3). The position of the calculated main π→π* transition band of the *E,E-m-bis*(AB) for both isomers coincides roughly with the position of the same transition for monomeric AB. Note that the intensity of the π-π* transition band in the *m-bis*(AB) spectra at ~305 nm is roughly twice the one in the *E*-AB spectra, which accounts for the presence of two isolated azo subunits. This can be explained by a superposition of two identical π-π* absorption bands of two individual *E*-AB isomers. As previous studies proposed [57, 60], the two azo subunits of *m-bis*(AB) are largely decoupled from each other, and thus break the *π*-conjugation system. The *m-bis*(AB) has two weak optically forbidden n-π* transitions at ~424 nm while the parent *E*-AB only exhibits one forbidden n-π* band at ~422 nm. The *trans-cis* transformation of one azo subunit of the *m-bis*(AB) leads to the an increase of the intensity of the *cis*- isomer n-π* transition band at ~424 nm as well as a decrease in the intensity of the π-π* transition band (Fig. 2). In fact, the intensity of the π-π* transition band of the *E,Z-m-bis*(AB) at ~305 nm only reaches half of that of the *E,E-m-bis(AB)*. Most notably the band does not disappear completely. It further supports the two azo

subunits in the *m-bis*(AB) to be largely decoupled from each other. The computed spectral trend therefore agrees well with the experimental data in the case of the π-π* transition of *m-bis*(AB) (see Fig. 4.2 and 4.3). Note that *E,Z-m*-bis(AB) has two significant spectral features of π-π* and n-π* transition bands simultaneously. The spectrum of *E,Z-m-bis*(AB) resembles a sum of the *E*- and *Z*-AB spectra. Overall, the theoretical data indicates that the *m-bis(AB)* apparently may have a high photoswitching efficiency compared to the parent AB.

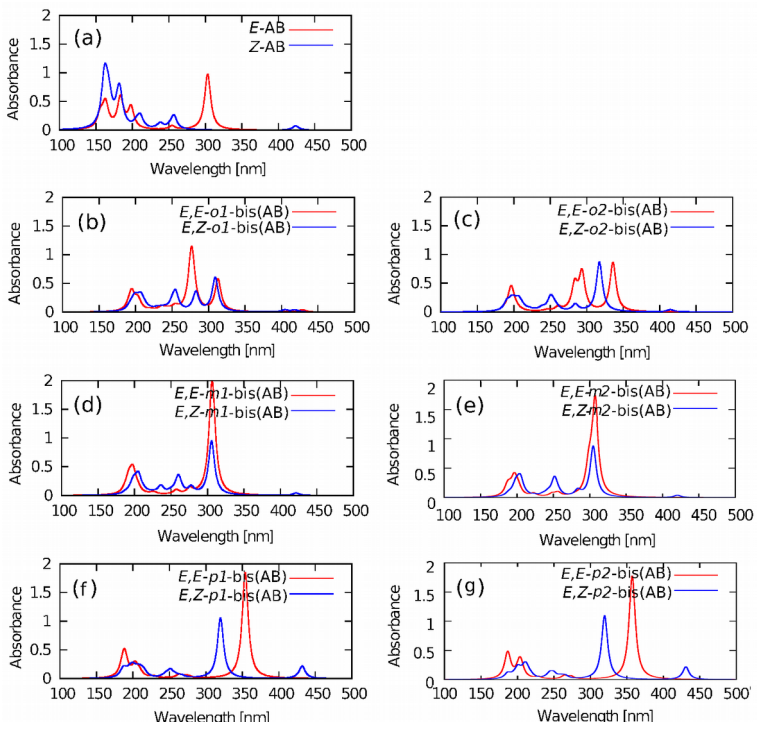

Figure 4.2: The absorption spectra of E-, Z-AB , E,E-bis(AB)s and E,Z-bis(AB)s in ethanol at the BHHLYP/6-31G level of theory using a PCM model for ethanol. The curves of E-AB and all E,E-bis(AB) forms are drawn by red lines, whereas Z-AB and all E,Z-bis(AB)s are indicated by blue lines.*

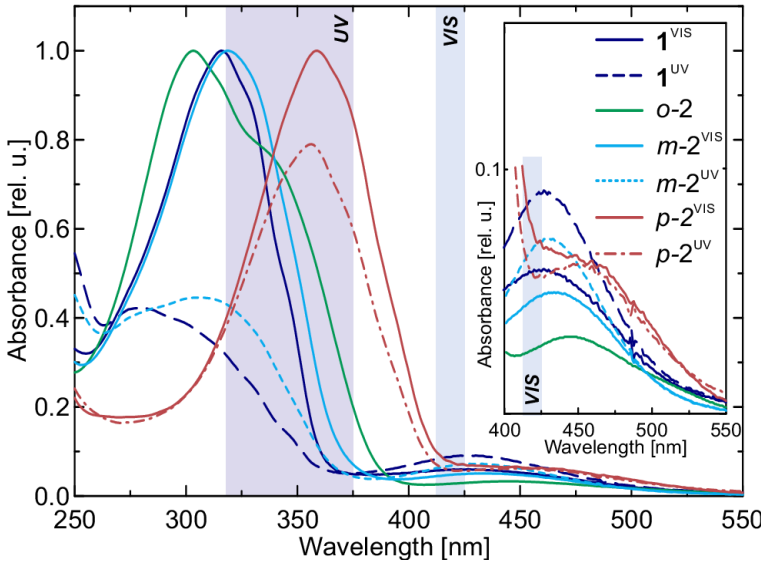

Figure 4.3: Eexperimental absorption spectra of the investigated bis(AB)s at the photo-stationary states (PSS) after VIS and UV irradiation (taken from reference 59).

Furthermore, the π-π* transition band of *E,E-p-bis*(AB) at ~355 nm shows a strong red-shift (~50nm) compared to *E*-AB (Fig. 4.2). Similar to *m*-bis(AB), the intensity of the π-π* transition band of *p-bis*(AB) is twice as high as that of *E*-AB, indicating the presence of two independent azo subunits. Here, the electronic π-conjugation of *p-bis*(AB) extends over the whole molecule, which decreases the excitation energy regarding the π-π* transition, and the electronic coupling between the two azo subunits weakens the photoreactivity of *p-bis*(AB) [58, 60]. The *trans-cis* isomerization of *E,Z-p-bis*(AB) produces a blue-shifted π-π* transition band as well as an increase in the absorption peak of the n-π* transition band compared to the original absorption spectrum of *E,E-p-bis*(AB). However, the absorption peak of the π-π* band at ~320 nm exhibits a small red-shift compared to *E*-AB. Apparently, the intensities of the π-π* transition band and the n-π* transition band of *E,Z-p-bis*(AB) are higher than that of *E,Z-o-bis*(AB) and *E,Z-m-bis*(AB). This implies that a certain level of conjugation between the two sub-azo units remains even after the *trans-cis* isomerization of one sub-azo unit. Although the twisted conformation of *E,Z-p-bis*(AB) destroys the planar structure as well as the conjugated π-system, weak electronic coupling between two sub-azo units may still play a role in the π-π* and n-π* transition bands. Eventually, the

absorption spectra of both *E,Z-p-bis*(AB)s are quite similar, which can almost be regarded as a sum of the *trans*-and *cis*-AB spectra. The *trans*- and *cis*-AB moieties of *E,Z-p-bis*(AB) behave like two isolated AB units with the corresponding contributions to the π-π* and n-π* transition bands, respectively.

According to the well-known Boltzmann distribution [194], the Boltzmann population for two *bis*(AB) forms in the ground state is given as:

$$\frac{P_2}{P_1} = e^{(E_1 - E_2)/kT} \tag{4-1}$$

where P_1, P_2 are the probabilities of state 1 and 2, E_1 and E_2 represent the energies of state 1 and 2, k is the Boltzmann constant, and T is the temperature of the system.

To determine which isomer dominates the absorption spectra, the Boltzmann population for the two possible isomers of three types of *bis*(AB)s were calculated using DFT/BHHLYP together with the 6-31G* basis set. The results show that the energy difference between the two possible isomers in the case of *m-bis*(AB) and *p-bis*(AB) is almost negligible and thus they have an approximately equal occupation probability, accounting for their spectral difference. However, the total energy of the *E*,*E-o2*-bis(AB) isomer is lower by roughly 0.05 eV than the *E*,*E-o1*-bis(AB) isomer. The data confirms that the occupation probability of *E*,*E-o2*-bis(AB) is roughly 87% while *E*,*E-o1*-bis(AB) has a lower probability of being occupied (13%). Therefore, the absorption spectrum of *E*,*E-o*-bis(AB) is most likely attributed to the planar isomer (~87%) with a minor contribution of the twisted isomer (~13%).

Moreover, the attachment and detachment densities [195-196] for the four lowest excited states of *E*,*E-o1-bis*(AB) and *E*,*E-o2-bis(*AB) are shown in Fig. 4.4 and 4.5. Apparently, the first and second excited states show an n-π* transition character while the third and fourth excited states are characterized as π-π* transitions. As expected, the

coupling interaction between two azo subunits is affected by the configuration of the *o-bis(*AB) and can be seen in the absorption spectra. As shown in Fig. 4.4 and 4.5, the detachment densities of the π-π* transition of *E*,*E-o2*-bis(AB) are located at two azo subunits and are more uniform compared to *E*,*E-o1*-bis(AB). This explains the spectral difference of the two *o*-bis(AB) isomers. The twisted *E,E-o1*-bis(AB) breaks the planarity of the molecule. This implies that the transition dipole moments oriented along two axes of the molecule interact with each other but make different contributions. The results also indicate that the excitoni interaction of two identical transition dipole moments of *o-bis*(AB) is significant, leading to the splitting of the π→π* transition band as previously discussed. The changes of the dual band in the absorption spectrum depend on the coupling interaction between the two azo subunits.

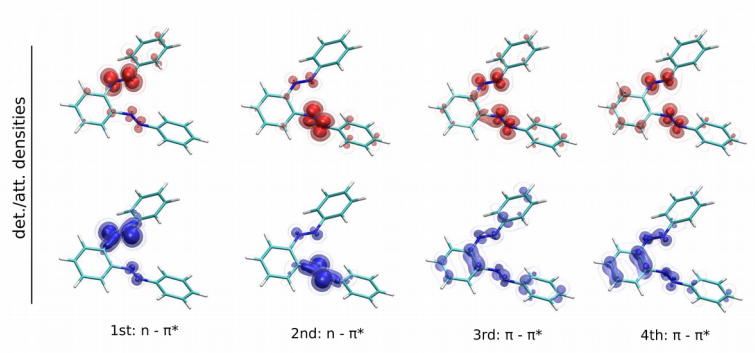

Figure 4.4: Isosurfaces for attachment and detachment densities for the four lowest excited states of the E,E-o1-bis(AB) at the BHHLYP/6-31G level of theory.*

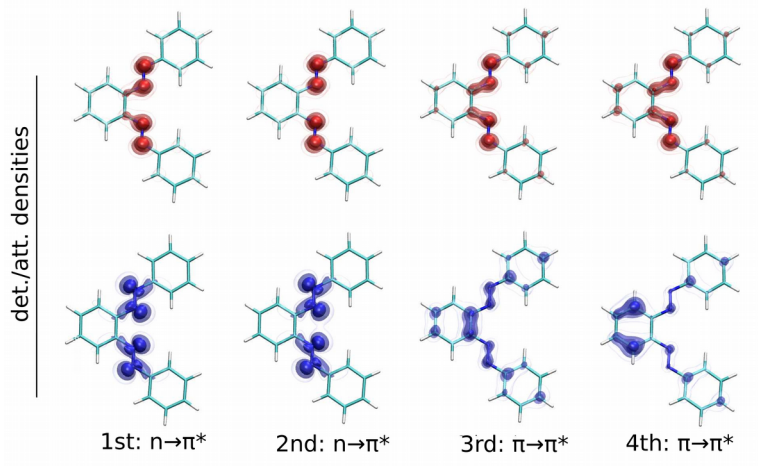

Figure 4.5: Isosurfaces for attachment and detachment densities for the four lowest excited states of the E,E-o2-bis(AB) at the BHHLYP/6-31G level of theory.*

4.2.3 Summary

The absorption spectra of *o-, m-* and *p-bis*(AB)s have been studied using TDDFT with the BHHLYP functional and the 6-31G* basis set. The calculations were performed both in gas phase and employing the C-PCM model for ethanol solvation. The results show that the spectral properties of two *o-bis*(AB) isomers are different. The absorption spectra of two *o-bis*(AB) isomers demonstrate the intramolecular excitonic interaction between the two azo subunits due to the geometry of the *ortho*-substitution pattern. In contrast, *m-bis*(AB)s and *p-bis*(AB)s show a very similar behavior in that the intensity is roughly twice higher than that of the monomeric AB. However, the two azo subunits in case of *m-bis*(AB)s are decoupled while the *p-bis*(AB)s have the highest degree of π-conjugation extending over the whole molecule, which leads to the planarity of the molecule. Overall, the photoswitching efficiency of *m-bis*(AB)s seems greatly increased without coupling interaction between the two sub-azo units, and can be expected to be applicable for highly efficient photoswitches in biomolecular systems and functional nanomaterials.

4.3 Tris-Azobenzene (tris(AB))

4.3.1 Motivation

In this section, I will further investigate the multiphotochromic properties of *meta*-tris-azobenzene (MTA) comprised of three azo subunits connected via a shared phenyl ring. MTA shows a triply symmetric molecular shape with a unique threefold symmetry. In a pure MTA structure without any additional susstituent the coupling interaction between the neighbouring azo subunits can be expected to be minimal, possibly enhancing the photoswitching efficiency of multiple azobenzenes. Furthermore, a structural expansion in the *ortho*-, *meta*- and *para*-position of the outer phenyl rings replaced by selective substituents generates a set of different auxochromic shifts in the π-π* absorption band leading to a useful separation of the absorption spectra. It would be expected that each of the azo subunits of substituted MTA can be trigged reversibly and selectively by choosing appropriate wavelengths of light, as shown in Fig. 4.6. That is, when substituted MTA is irradiated by a laser with a specific wavelength of light, only the sub-azo unit with a certain functional group can be switched independently undergoing *trans-cis* isomerization between two conformational states.

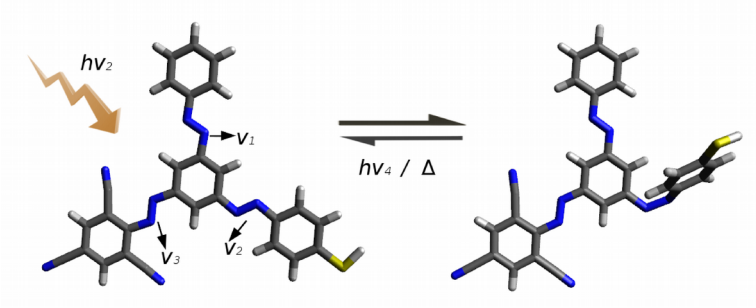

Figure 4.6: Photochromism of substituted MTA for the controllable switching process.

4.3.2 Computational methods

As discussed in last section, time-dependent density functional theory has successfully reproduced accurate vertical excitation energies as well as experimental values for many organic compounds. Using TDDFT combined with and without conductor-like polarizable continuum model (C-PCM) [95-97], the absorption spectra of the parent AB, the *meta-bis*(AB) and *meta*-tris(AB) molecules in the gas phase and in ethanol were calculated. As shown in Fig. 4.7, several substituted MTA structures have been calculated to optimize the efficient separation of the π-π* absorption band, as adding F, Cl, Br, Me, CN, NH2, OH, SH groups in the *ortho-, meta-, and para*-positions of the outer phenyl rings. According to my calculations, three azo subunits with appropriate functional groups can be considered as three isolated units, giving rise to three well-separated π-π* bands, respectively. Furthermore, the excited state potential energy surfaces along three isomerization pathways were calculated for the purpose of gaining an understanding of cooperative isomerization behavior of coupled azobenzenes. All initial structure optimizations in the ground state were calculated at the TDDFT/BHHLYP level of theory with the 6-31G* basis set [185]. The random phase approximation (RPA) technique [197-198] was employed in the excited state optimizations. All TDDFT calculations were carried out with the Q-Chem 4.3 [177] and the Orca 3.0 [176] program packages.

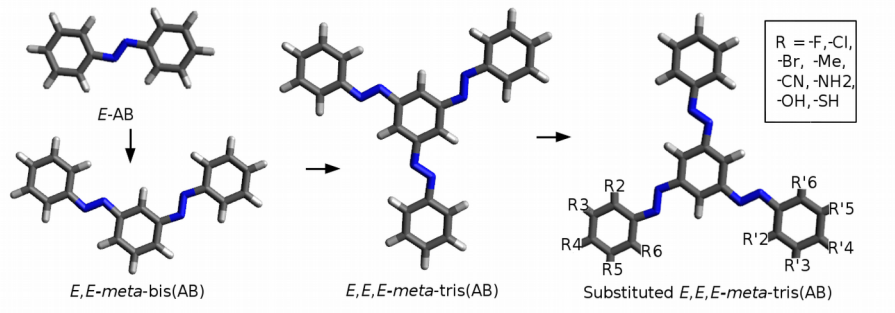

Figure 4.7. Schematic representation of unsubstituted and substituted MTA. Rn represents a series of functional groups and the numbering system.

4.3.3 Absorption spectra of MTA

The absorption spectra of the *E*- and *Z*-isomers of the monomeric aozbenzene (AB), the *E,E-, E,Z-, Z,Z*-isomers for the *meta*-bis-azobenzene (*m*-bis(AB)), as well as the *E,E,E-, E,E,Z-, E,Z,Z-, Z,Z,Z*-isomers for the *meta*-tris-azobenzene (MTA) in the gas phase and in ethanol are shown in Figure 4.8, respectively. As previous studies indicated [57, 60], the spectra of *m*-bis(AB) show similar spectra as the parent AB, differing only in the π-π* absorption intensity and showing a minor red-shift. It is found that the absorption spectra of MTA also exhibit similar multiphotochromic properties compared to the parent AB and *m*-bis(AB). Note that the intensity of the main π-π* absorption band of *m*-bis(AB) is roughly the same as the superposition of intensities of two isolated azobenzene spectra (three in the case of MTA). There is a relatively stable and substantial proportion relation between an increase in intensity of the π-π* absorption band and the number of the isomerized azo subunits. Specifically, the photoswitching efficiency of *m*-bis(AB) and MTA can be enhanced by a factor of approximately two for *m*-bis(AB) and three for MTA after both compounds undergo *trans-cis* isomerization completely. In a sense, the significant photoswitching efficiency is most likely attributed to two decoupled azo subunits in *m*-bis(AB) and three decoupled azo subunits in MTA, which reveals a lack of interaction between the different azo subunits in MTA. In consequence, each of the azo subunits can be operated independently, which means that it is possible to design a single-molecule photoswitch with three selectively and reversibly light-induced azo subunits by means of introducing a set of functional groups attached to the outer phenyl rings.

Moreover, it is worthwhile to note that the intensity in the π-π* band of the *E,Z-m*-bis(AB) and the *E,E,Z*-MTA after *trans-cis* isomerization of the first azo subunit decreases much more than that of the second azo subunit. This is in good agreement with *Cisnetti's* conlusion that the presence of one *cis*-azo unit in *m*-bis(AB) hinders the isomerization of the second azo subunits= [60]. Interestingly, switching of the first two azo subunits does not influence the isomerization of the third azo subunit in MTA. Therefore, it is supposed that an asymmetry in the torsional potential energy surface is introduced by the first cis-azo unit of *E,Z-m*-bis(AB) and *E,E,Z*-MTA. Hence, the

isomerization of the third azo subunit means that *Z,Z,Z*-MTA probably possesses a new form of symmetry again.

Besides, it has been observed that the computed features of the absorption spectra in ethanol are consistent with spectra obtained in the gas phase. By comparison to the spectra in the gas phase, the absorption maxima of the π-π* band is a little red-shifted by approximately 11 nm and a slight blue-shift of the n-π* absorption band was observed in ethanol for all AB, *m*-bis(AB) and MTA isomers, which can be attributed to the fact that the absorption properties of these azo compounds are solvent dependent.

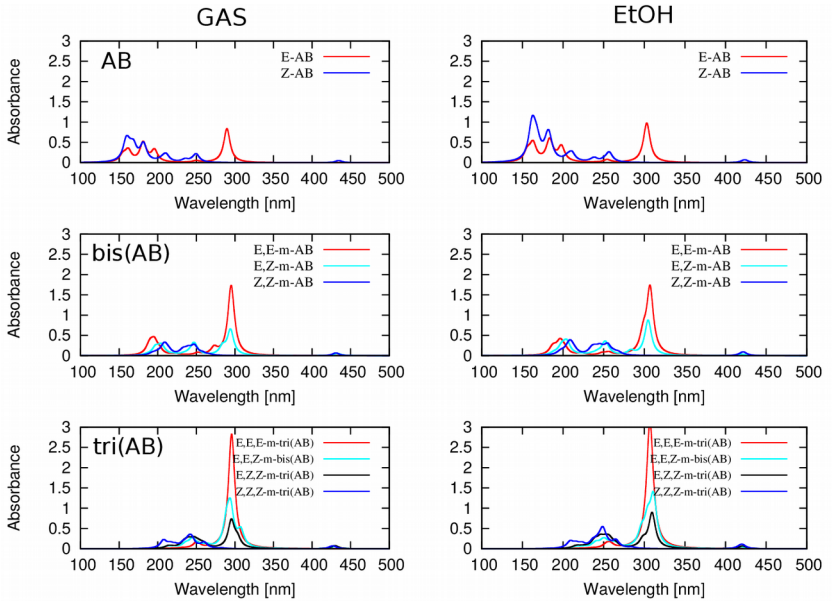

Figure 4.8: Comparison of the absorption spectra of different twisted isomers at optimized AB, bis-(AB), and tris-(AB) geometries in the gas phase and in ethanol.

To address essentially multiphotochromic features and the chemical behavior of coupled azobenzene compounds, a set of different types of MTA derivatives are expected to deliver new light-induced functions to be used in the fields of photochemistry, nanomaterials and biomolecular science. Here, a strategy to optimize the efficient separation of the absorption spectrum with respect to different azo subunits is presented, aiming at control of the photoswitching states of different azo subunits separately with

specific wavelengths of light. In view of the known effect of electron-donating and withdrawing groups on the absorption spectrum, I have designed a series of mono-substituted MTA, di-substituted MTA and multi-substituted MTA with a series of substituents such as F, Cl, Br, Me, CN, NH_2, OH, SH groups in the *ortho-, meta-* and *para*-positions of the outer phenyl rings.

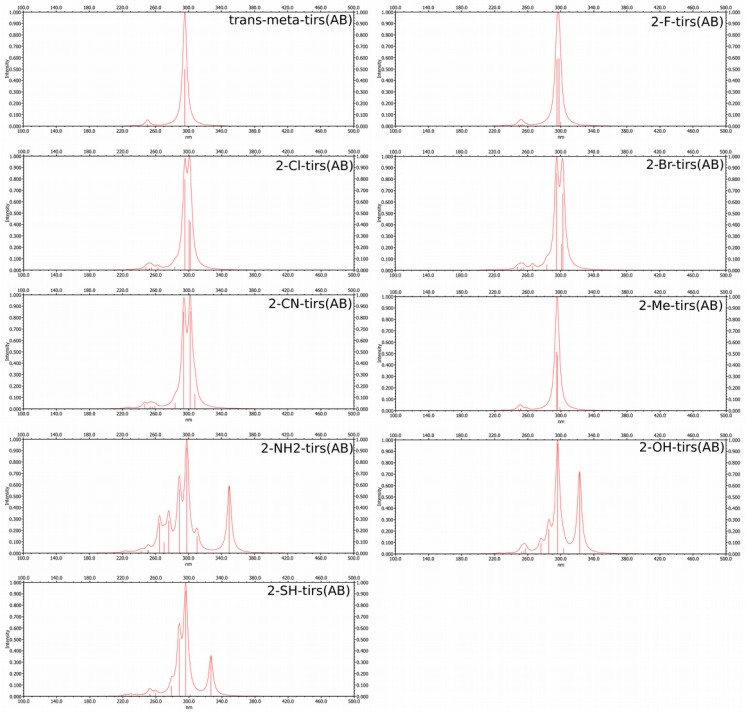

Figure 4.9: Comparison of the absorption spectra of ortho-substituted tris(AB).

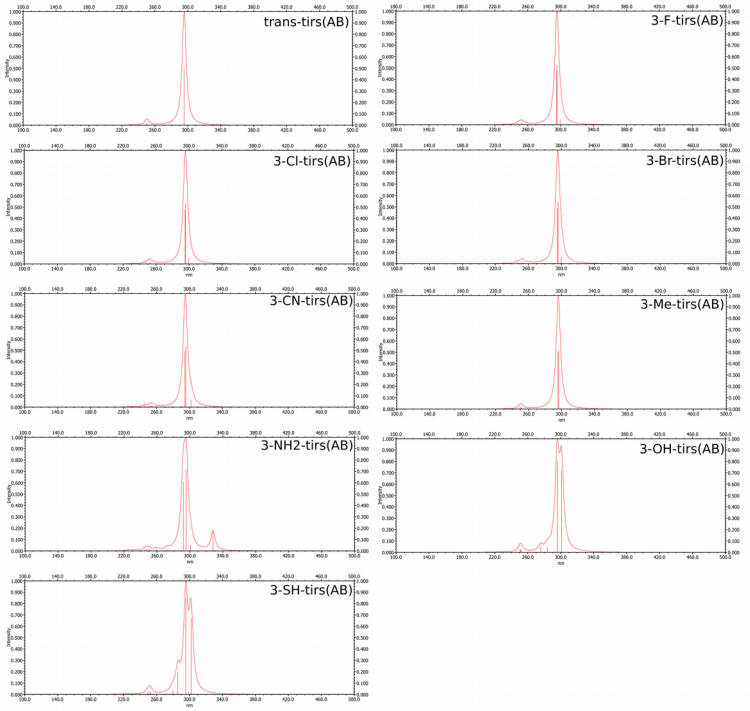

Figure 4.10: Comparison of the absorption spectra of meta-substituted tris(AB).

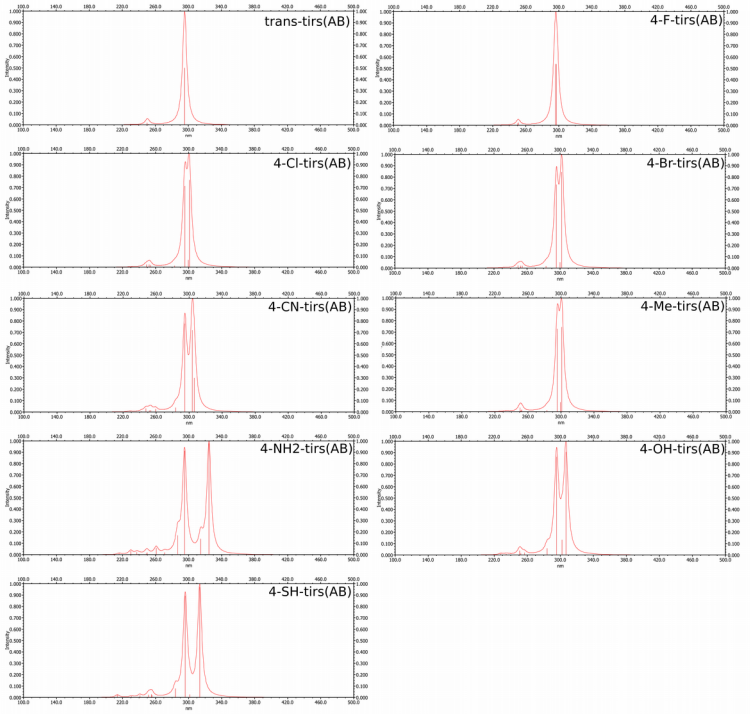

Figure 4.11: Comparison of the absorption spectra of para-substituted tris(AB).

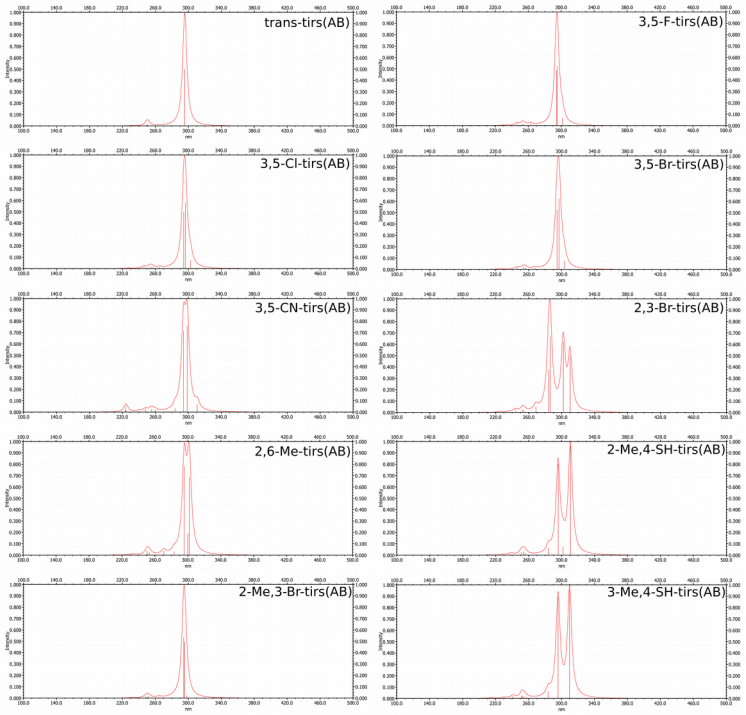

Figure 4.12: Comparison of the absorption spectra of di-substituted tris(AB).

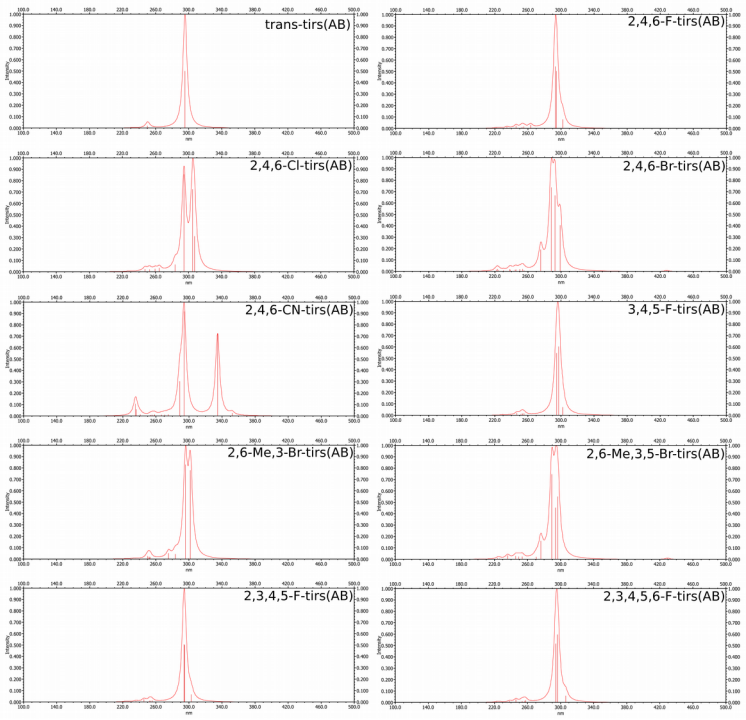

Figure 4.13: Comparison of the absorption spectra of multi-substituted tris(AB).

The absorption spectra of MTA and a set of *mono*-substituted MTA, *di*-substituted MTA and multi-substituted MTA are gathered in Fig. 4.9-4.13. The results show that *para*-NH_2 substituted MTA and several other derivatives could produce a new intense and red shifted π-π* absorption band and an original π-π* band. However, NH_2-substituted MTA has a small absorption peak between the red-shifted π-π* band and the original π-π* band, which may lead to overlap with an adjacent π-π* band originating from neighbouring sub-azo unit. Thus, I decided to use the CN substituted azo subunits which generates a high intensity red shifted π-π* band and an even larger red shifted π-π* band with weak intensity as shown in Fig 4.9. Therefore, its weak intensity π-π* band may not interact with other π-π* absorption bands produced by the other substituted azo subunits. Overall, using appropriate functional groups it can be expected that the mutual interference between two π-π* absorption bands with respect to different azo subunits can be avoided.

Figure 4.14 shows the absorption spectra of MTA and its derivatives 4-SH-MTA, 2,4,6-CN-MTA and 2,4,6-CN,4-SH-MTA in the gas phase. The vertical excitation energies and corresponding oscillator strengths are presented in Table 2. This work focuses on the separation of the π-π* absorption band, so the intensity of the absorption spectra was normalized for MTA and its derivatives. As shown in Fig. 4.14, the absorption bands of 4-SH-MTA and 2,4,6-CN-MTA show similar spectral changes while exhibiting a significant dual band feature. Apart from the original π-π* absorption band, both MTA derivatives produce new and intense π-π* bands which are largely red-shifted toward lower energies compared to that of the parent MTA. 4-SH-MTA has a small red-shifted but high intensity π-π* absorption band at ~314 nm, whereas 2,4,6-CN-MTA possesses a larger red shift in the π-π* band at ~335 nm. This can be mainly attributed to the introduction of SH and CN groups.

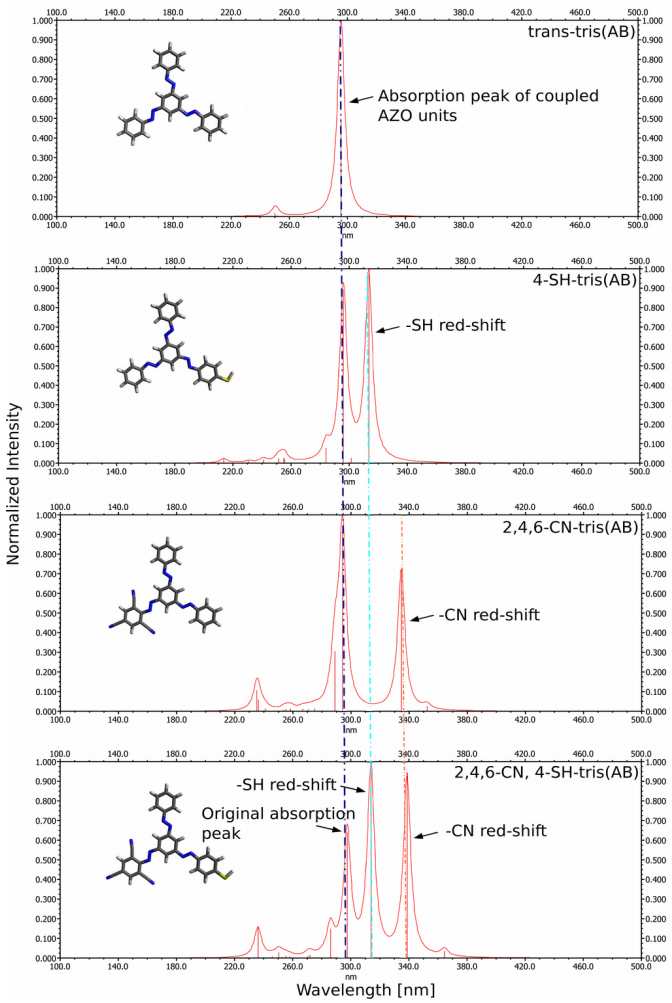

Figure 4.14: Comparison of absorption spectra of MTA, 4-SH-MTA, 2,4,6-CN-MTA and 4-SH, 2,4,6-CN-MTA. TDDFT/BHHLYP with the 6-31G basis set was employed for the excitation energy calculations in the gas phase.*

However, the oscillator strength changes between MTA and its derivatives in Table 4.2 reveal more complicated reasons for the bathchromic shift of 4-SH-MTA and 2,4,6-CN-MTA. It is expected in theory that the superposition of the absorption spectra of the two azo subunits approaches twice the value of that of one isolated azo subunit. One possible reason for the changes in oscillator strength is that the exciton interactions between two transition dipole moments of two azo subunits are not negligible when introducing a functional group breaking the initial structural symmetry of MTA. Note that the low intensity of the blue-shifted π-π* band in the case of 4-SH-MTA and 2,4,6-

CN-MTA indicates the existence of intramolecular excitonic coupling of the neighbouring transition dipole moments. In addition, in Table 2, it is seen that the intensity of the original π-π* band of 4-SH-MTA and 2,4,6-CN-MTA is only reduced by roughly 50% relative to that of the CTA, which coincidentally corresponds to a superposition of the recombinational spectra of three unsubstituted azo subunits.

state	MTA	4-SH-MTA	2,4,6-CN-MTA	2,4,6-CN,4-SH-MTA
S_1	2.92 (0.0000)	2.92 (0.0000)	2.63 (0.0000)	2.63 (0.0000)
S_2	2.93 (0.0000)	2.93 (0.0000)	2.92 (0.0000)	2.92 (0.0000)
S_3	2.93 (0.0000)	2.95 (0.0000)	2.93 (0.0000)	2.95 (0.0001)
S_4	4.15 (0.0002)	3.95 (1.4749)	3.52 (0.0369)	3.40 (0.0410)
S_5	4.19 (1.4123)	4.11 (0.0393)	3.70 (1.0214)	3.66 (1.0194)
S_6	4.19 (1.4144)	4.19 (1.3537)	4.21 (1.3012)	3.95 (1.0578)
S_7	4.40 (0.0000)	4.36 (0.1187)	4.29 (0.4312)	4.16 (0.7010)
S_8	4.93 (0.0041)	4.85 (0.0324)	4.29 (0.0000)	4.30 (0.0000)

Table 4.2: Comparison of the vertical excitation energies of the first eight low-lying excited states of MTA and its derivatives at TDDFT/BHHLYP level of theory with the 6-31G basis set. The values are given in eV. The oscillator strength is given in parentheses.*

In contrast, the absorption spectrum of 2,4,6-CN,4-SH-MTA shows three distinct π–π* absorption bands with roughly identical intensity. As expected, the π-π* absorption bands for each azo subunit seem sufficiently separated to allow for *trans-cis*-isomerization with different wavelengths of light. In addition, it should be noted that the oscillator strength of the blue-shifted π-π* band is still significant, which indicates the presence of weak coupling interactions between two neighbouring azo subunits. However, this small blue-shifted π-π* band is more relevant for the π-π* transition of the unsubstituted azo subunit, which does not affect the switching of the other two. Nevertheless, the unique substituted MTA structure is of importance in the sense that

each azo subunit of the substituted MTA can in principle be operated independently and switched with their own specific wavelengths of visible light.

Next, I turn to the attachment and detachment densities of the lowest ten excited states. The attachment and detachment densities of MTA, 4-SH-MTA, 2,4,6-CN-MTA and 2,4,6-CN,4-SH-MTA are presented in Figure 4.15-4.18. The distributions of the attachment and detachment densities for the 5th, 6th and 7th excited state with respect to three relevant high intensity π-π* bands clearly reveal a π-π* transition character as well as distinct activated fragments upon absorption of light of different wavelengths, which corresponds to the absorption spectra of three different azo subunits. Fig. 4.18 demonstrates the selective control of the switching of azo subunits to be feasible. In addition, an alternative explanation for the low intensity π-π* band at around 365 nm is that a significant charge transfer character is observed in the attachment and detachment densities for the 4th excited state, leading to a small overlap of the detachment and attachment densities as well as a negligible transition dipole moment. However, it may not affect the individual switching efficiency of azo subunits, since the intensity of this weak π-π* band is far less than that of its neighbouring π-π* band.

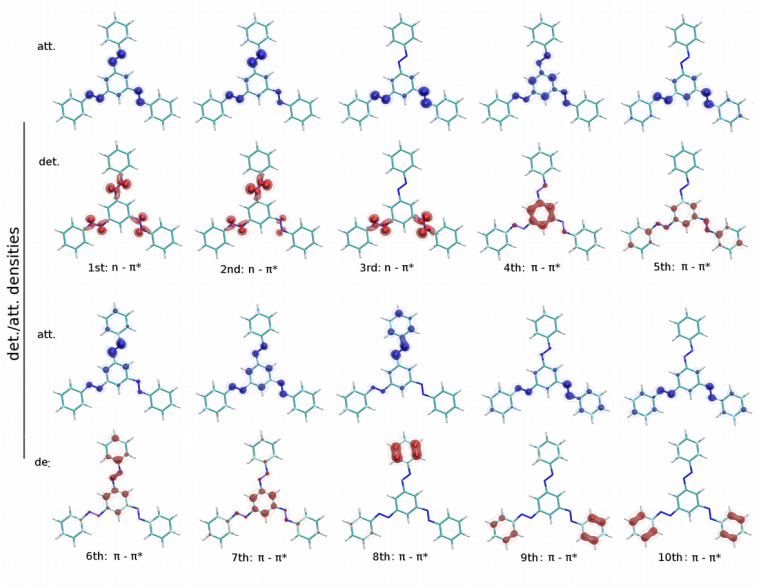

Figure 4.15: Detachment (red) and attachment (blue) densities for the energetically lowest eight excited states of MTA at the BHHLYP/6-31G level of theory.*

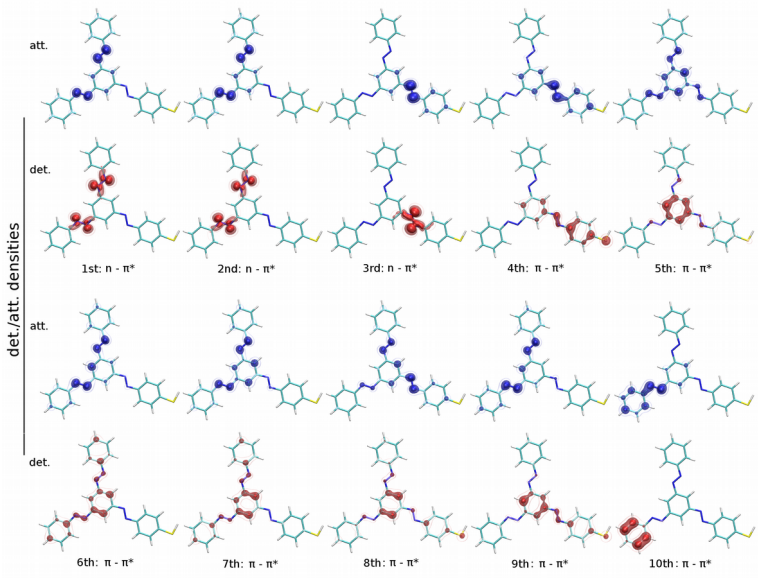

Figure 4.16: Detachment (red) and attachment (blue) densities for the energetically lowest eight excited states of 4-SH-MTA at the BHHLYP/6-31G level of theory.*

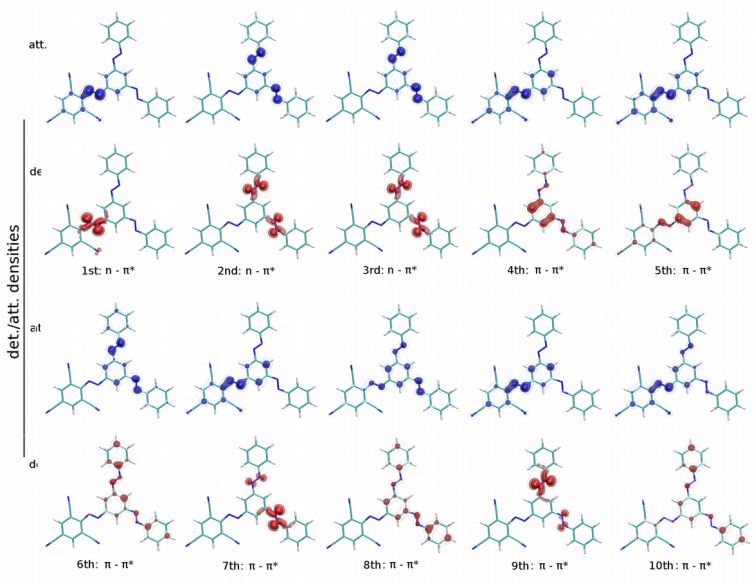

Figure 4.17: Detachment (red) and attachment (blue) densities for the energetically lowest eight excited states of 2,4,6-CN-MTA at the BHHLYP/6-31G level of theory.*

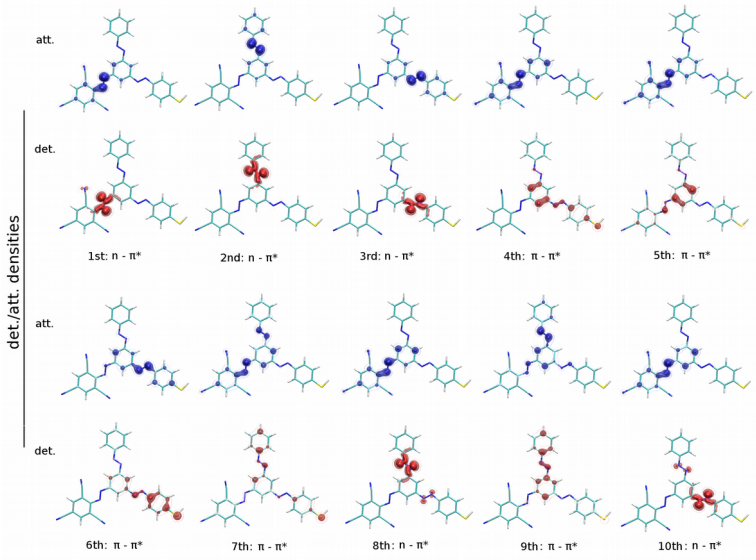

Figure 4.18: Detachment (red) and attachment (blue) densities for the energetically lowest eight excited states of 4-SH, 2,4,6-CN-MTA at the BHHLYP/6-31G level of theory.*

In this context, my intent was to introduce appropriate functional groups to change the position of the π-π* band in the absoption spectra corresponding to individual azo subunit, providing an efficient separation in the π-π* absorption band. Overall, this

fantastic substituted MTA structure gives rise to an efficient separation depending on various substituents. Thus, the inherent absorption wavelengths relative to each azo subunit can be modulated. Nevertheless, it is possible to selectively monitor the reversible isomerization of each of the azo subunits by choosing specific wavelengths of light. Therefore, this work paves the road for a powerful design of macroscopic photoswitching systems.

Figure 4.19 shows three calculated potential energy curves of MTA along rotation, inversion and concerted-inversion isomerization pathways. They were obtained by optimizing all geometrical parameters restricting the movement of the CNNC dihedral angle, CNN angles, and the concerted CNN angles, respectively. The results indicate that the overall trend of the three potential energy surfaces of MTA is in very good agreement with previous studies for the parent azobenzene [32-34]. Specifically, the S_1 potential energy surfaces illustrate the main features of a barrierless reaction along the rotation pathway and substantial energy barrier along the inversion and concerted inversion pathways in the first excited state. It is seen that the curves in S_1 state along the inversion pathway is rather flat compared to the curve in S_1 state along the converted inversion pathway, which also resembles the parent azobenzene. Moreover, a steep curve at the concerted CNN angels beween 90° and 110° along the concerted-inversion pathway may result in a rapid relaxation from the S_2 state or higher excited states to the S_1 state and may thereby contributes to overcoming the energy barrier on the S_1 surface. Similar features of the PES demonstrate that an individual azo subunit behaves like a monomeric azobenzene.

The structural evolution process of MTA along the rotation pathway after the optimization of the S_1 state are displayed in Figure 4.20. It is worthwhile to note that one azo subunit undergoes isomerization along the rotation coordinate while two remaining azo subunits are still in-plane. That is, the changes in geometry reveal that an out-of-plane rotation process of one azo subunit was obviously not affected by the other two. This further confirms the decoupling of azo subunits in MTA.

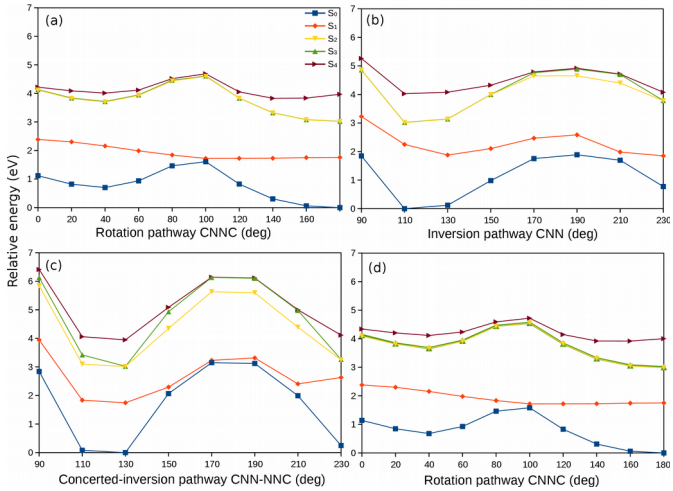

Figure 4.19: PES of MTA along the rotation pathway, inversion pathway and the concerted-inversion pathway based on the optimized S_1 state geometries. (a) Rotation PESs of the first subunit. (b) Inversion PESs of the first sub-azo unit. (c) Concerted-inversion PESs of the first subunit. (d) Rotation PESs of the second sub-azo unit.

Moreover, as *Cisnetti* [60] reported, the photoactivity of the second azo subunit may be influenced by the first one due to the introduction of asymmetry. The spectral analysis of AB, *m*-bis(AB) and MTA also reveals that the photoactivity of the second azo subunit in *m*-bis(AB) and MTA is decreased, which is consistent with the experimental conclusion. However, the potential energy curves for the rotation isomerization of the second azo subunit show very similar isomerization features relative to that of the first azo subunit and may provide an alternative significant insight into the isomerization process of coupled azobenzenes. Nevertheless, my computational results have established a good foundation for further research on multiphotochromic properties and the photochemical behavior of multiazobenzenes.

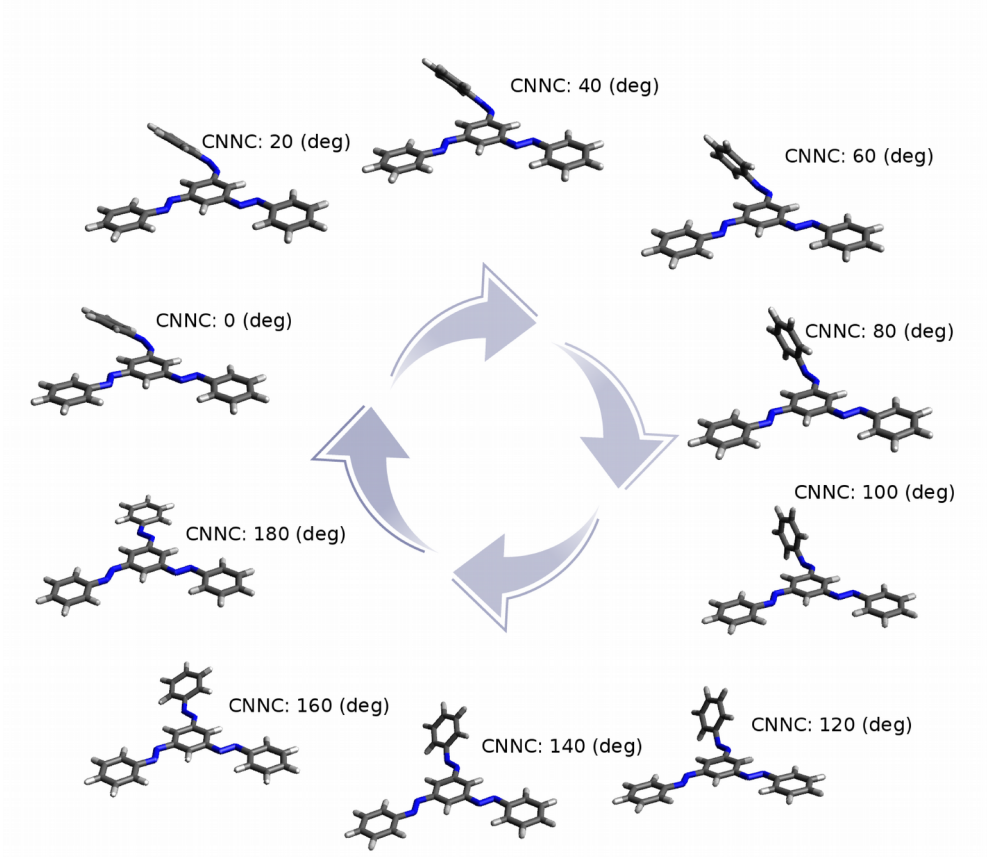

Figure 4.20: Structural evolution process of the first azo subunit *for CTA along the rotation reaction coordinate (CNNC).*

4.3.4 Summary

In summary, the multifunctional coupled-azobenzenes MTA composed of three sub-azo units linked via a central phenyl ring were investigated using TDDFT calculations. The photoswitching efficiency of MTA is enhanced greatly in comparison to the monomer AB due to three decoupled azo subunits. More importantly, each of the azo subunits of the substituted MTA can in principle be selectively and reversibly switched by specific wavelengths of light. It has been found that the isolated and sharp peak in the absorption spectrum of MTA confirms a pronounced superposition of absorption bands of each azo subunit, implying the presence of degenerate states. However, introducing functional groups to MTA leads to the splitting of the main absorption band, and the broken

threefold symmetry may be another possible factor for the splitting. Moreover, the potential energy curves along three pathways reveal the independent isomerization of an individual azo subunit without interaction with the other two. Thus, MTA can be utilized to design complex photoresponsive nanomaterials and biomolecules based on its unique decoupling and threefold symmetry properties.

4.4 Cyclotrisazobenzene (CTA)

4.4.1 Motivation

Recent studies [199-200] of macrocycle compounds including more than two sub-azo units have been presented, which are useful for designing various macroscopic photocontrollable materials [58, 62, 82] and biomolecular systems [201-204]. A strongly constrained multiazobenzene ring system is cyclotrisazobenzene (CTA) [70-71] with a fully conjugated π-system of the *trans*-isomer leading to high stability. CTA (Fig. 4.21) is a type of azobenzenophane containing three azo subunits. The specific macrocyclic connection pattern of three azo subunits enhances the complexity of the photophysical and photochemical properties. In the electronic ground state, all azo subunits of CTA are in a plane. The ππ* transition band in the absorption spectrum of *E*,*E*,*E*-CTA is blue-shifted (294 nm, see Fig. 4.21) compared to monomeric *E*-AB. Interestingly, after UV irradiation, *E*,*E*,*E*-CTA does not isomerize and has no change in the absorption spectrum. In experiments [70], it was found that no product formation is observed with flash photolysis either. Although these results suggest that the azo subunits in CTA cannot be switched between *trans*- and *cis*-isomers, it is still possible that the thermal *cis*→*trans* relaxation in the azo compounds takes place readily and thus leads to an ultrafast *trans*→*cis*→*trans* isomerization process. This might be related to the macrocyclic ring strain of the planar geometry during the isomerization process. So far, there are only a few contributions to synthesis and isomerization of CTA [70-71,

203-205], however, the photochemical properties and the isomerization reaction have not been clarified yet. In this section, the photochromic properties and the excited state relaxation of cyclotrisazobenzene will be addressed using the TDDFT method and the 6-31G* basis set to determine whether CTA undergoes *trans*→*cis* isomerization.

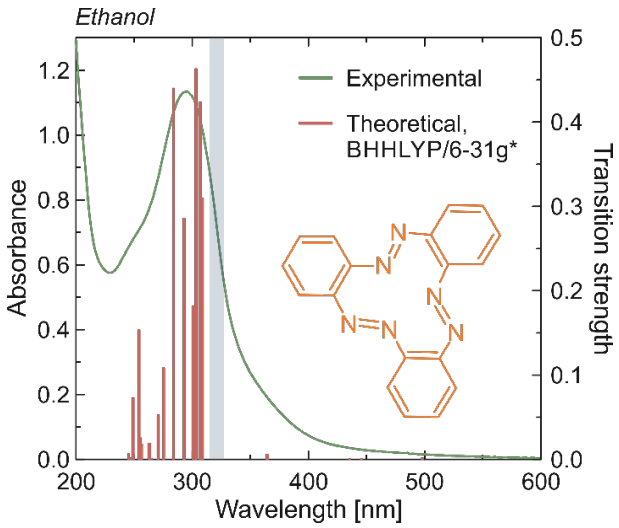

Figure 4.21: Experimental and theoretical absorption spectrum of CTA in ethanol. (Note: this figure is taken from reference [205])

It has to be noted here that some of the content of this chapter has been submitted for publication as:

Chavdar Slavov, Chong Yang, Luca Schweighauser, Hermann A. Wegner, Andreas Dreuw, and Josef Wachtveitl

Cyclotrisazobenzene – a molecular light-to-heat energy converter, ***2017***

4.4.2 Computational methods

At the beginning of this work, a series of excitation energy calculations for CTA using TDDFT together with several typical standard hybrid functionals (CAM-B3LYP [206], BHHLYP [141], B3LYP [140, 187], BLYP [139, 148]) and TDHF [182-184] have been

performed to identify a more appropriate approach. At the same time, calculations using the algebraic diagrammatic construction scheme for the polarization propagator of second order (ADC(2) [91-94]) are used to benchmark the TDDFT calculations, as seen in Table 4.3. The BHHLYP functional reproduces the lowest four excitation energies that are approximately 0.1 eV higher than ADC(2) calculations and a little bit higher for some higher excited states. In contrast, the CAM-B3LYP functional has relatively larger deviations when compared to ADC(2) benchmark results for the lowest four excited states. The BLYP and B3LYP functionals underestimate the excitation energies of the eight lowest excited states while TDHF overestimates the excitation energies. Thus, as previously, the calculations of the absorption spectra were also performed using TDDFT in combination with the BHHLYP functional and the 6-31G* basis set [185], employing a conductor-like polarizable continuum model (C-PCM) [95-97] for ethanol solvation (dielectric constant of ε=24.5).

Note that a 0.2 eV shift between the theoretical excitation energies and the experimental peak is attributed to the different hybrid functionals which include different components of Hartree-Fock exchange. However, the computed theoretical spectrum after a simple 0.2 eV shift is indeed in good agreement with the experimental results (See Fig. 4.21). The potential energy surface calculations along the reaction path provide valuable information for the understanding of the photoisomerization process.

State	BLYP	B3LYP	CAM-B3LYP	BHLYP	TDHF	ADC(2)
S_1	1.29 (0.0023)	1.93 (0.0013)	2.38 (0.0007)	2.53 (0.0009)	3.04 (0.0009)	2.48 (0.001034)
S_2	1.75 (0.0013)	2.36 (0.0017)	2.76 (0.0004)	2.89 (0.0004)	3.28 (0.0003)	2.87 (0.000972)
S_3	1.79 (0.0026)	2.67 (0.0009)	2.88 (0.0006)	2.99 (0.0004)	3.29 (0.0023)	3.05 (0.000599)
S_4	2.15 (0.0023)	2.77 (0.0030)	3.59 (0.0011)	3.69 (0.0029)	4.66 (0.0179)	3.80 (0.007776)
S_5	2.19 (0.0010)	2.86 (0.0058)	3.91 (0.0007)	4.41 (0.0439)	5.48 (0.7658)	3.93 (0.036589)
S_6	2.33 (0.0090)	3.02 (0.0056)	4.05 (0.0254)	4.46 (0.0763)	5.61 (0.4747)	4.01 (0.006568)
S_7	2.47 (0.0058)	3.39 (0.0051)	4.37 (0.0138)	4.59 (0.1168)	5.66 (0.0057)	4.34 (0.030173)
S_8	2.72 (0.0139)	3.52 (0.0280)	4.49 (0.1672)	4.64 (0.2259)	5.72 (0.0036)	4.46 (0.027583)

Table 4.3. Comparison of the vertical excitation energies of the eight low-lying excited states of CTA using different approaches with the 6-31G basis set. The values are given in eV. The intensity is in parentheses.*

In this context, the ground state and the excited state geometry optimizations of all CTA calculations along the torsional pathway in this work were carried out at the DFT and TDDFT/BHLYP/6-31G* level of theory. The relaxed scans of the excited state potential energy surfaces (PES) along the torsional coordinate were generated by calculating single vertical excitation energies for the constrained optimized geometries of the relevant excited states. The Tamm-Dancoff approximation (TDA) [147] was used in the TDDFT excited state optimization calculations for relaxed potential energy curves. All quantum chemical calculations for CTA were carried out using the Q-Chem 4.3.0 program package [177].

4.4.3 Excited state relaxation mechanism

The calculated excitation energies of *E,E,E*-CTA are plotted in Fig. 4.21 together with the experimental absorption spectrum. This plot exhibits a good agreement between my theoretical results and the experimental data. From the analysis of the attachment and detachment densities (See Fig. 4.22), it is found that the lowest three excited states can be characterized as nπ* states, which represent linear combinations of the well-known nπ* state of monomeric azobenzene. The higher excited states up to S_8 have ππ* character, which show delocalization over the whole molecule. Since the oscillator strengths of the lowest three nπ* states are relatively small and thus give insignificant contributions to the main absorption band, CTA generally has to be excited into the ππ* states in experiments. Therefore, the potential energy curves along the rotation coordinate for the optimized geometry at fixed CNNC dihedral angle positions for the ground state and the lowest nπ* (S_1) and ππ* (S_4) states were calculated.

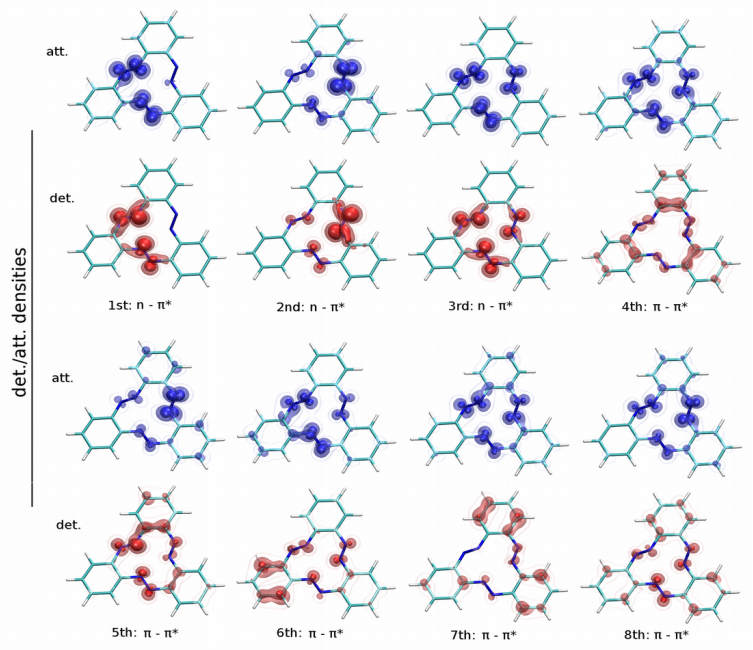

Figure 4.22: Isosurfaces for attachment and detachment densities for the lowest excited states of CTA based on the S_0 optimized geometry at the BHLYP/6-31G level of theory.*

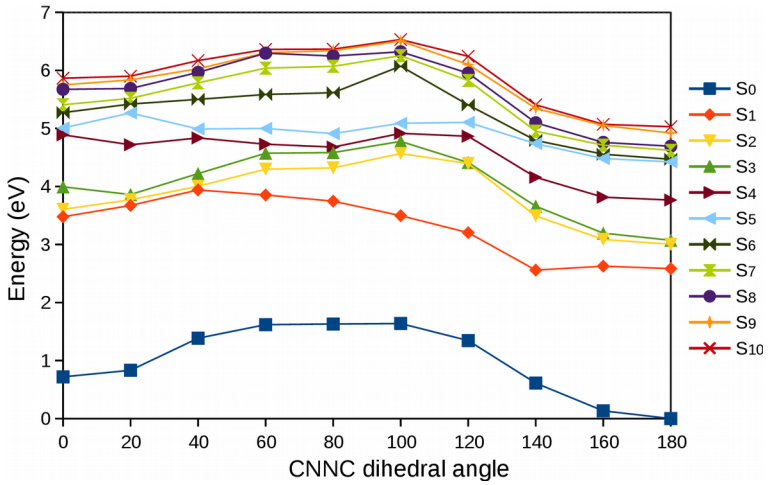

Figure 4.23: Potential energy curves for the torsion around the N=N double bond calculated at the S_0 optimized geometry at the BHHLYP/6-31G level.*

As seen in Fig. 4.23, the overall shapes of the potential energy curves of the ground state and the eight low-lying excited states all show significant energy barriers (>1eV) along the reaction pathway from the *E*,*E*,*E*- to the *E*,*E*,*Z*-isomer. Owing to the

substantial energy barrier, the isomerization of *E*,*E*,*E*-CTA is unlikely to occur on these potential energy surfaces. In other words, the excited state potential energy surfaces exhibit a steep slope at the *E*,*E*,*E*-isomer side, which indicates a rapid relaxation process from the higher excited state to the lower excited states upon excitation into the ππ* states. In this respect, after excitation into the higher excited states the molecules have two possible competing relaxation pathways: 1) internal-conversion to the lowest nπ* state; and 2*)* direct relaxation to the ground state. Due to the very large energy gap between the higher excited states and the ground state (Fig. 4.23), the latter path seems unlikely to take place. Rather, the CTA molecules undergo internal conversion leading to ultrafast relaxation from the Frank-Condon region of the higher excited states down to the lowest nπ* state. The fast internal-conversion decreases the excited state relaxation lifetime and thereby lowers the probability of isomerization of CTA. This effect is in good agreement with Kasha's rule and has been demonstrated experimentally [205].

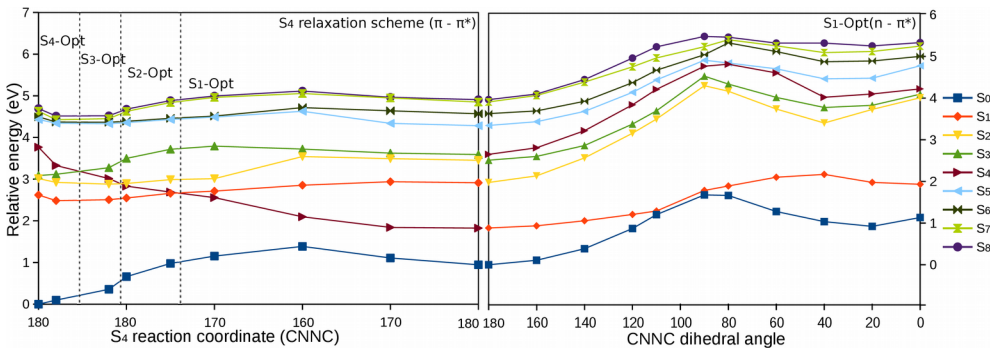

Figure 4.24: (a) Potential energy curves along the relaxation coordinate from the S_4 to the S_1 optimized geometry at 180° of the CNNC dihedral angle. During the optimization the CNNC dihedral angle was allowed to adjust freely during the geometry optimization of the remaining part of the molecule. (b) Potential energy curves for the torsion around the N=N double bond calculated at the S_1 (lowest excited state with nπ character) optimized geometry.*

To fully characterize the relaxation dynamics calculations of the potential energy curves, the S_4 optimized geometry was calculated at TDDFT/BHLYP level of theory by letting the CNNC dihedral angle relax freely (Fig. 4.24a). With the relaxation of the

complete molecule the potential energy of the molecule reduces from the S_4 to the S_1 level and the character of the excited state gradually changes from ππ* to nπ*. Eventually, the excitation energies after relaxation of the S_4 state coincide with the results of the S_1 optimization, indicating relaxation from S_4 to S_1. This fast relaxation is considered to be ultrafast and agrees well with experimental result [205]. Geometry optimizations of the lowest ππ* excited state S_4 reveals that no stable minimum exists in the ππ* state manifold (Fig. 4.24a), but instead barrierless crossings with all lower-lying states exist, which allow for an efficient decay of the excited state population into the lowest nπ* excited state S_1. Along this path, the dihedral angle of the azo subunits does not change significantly, but vary only between 160˚ and 180˚. The geometries of these crossing points are very difficult to determine due to numerical instabilities. Since the excited state surfaces lie so close in energy, one cannot speak of isolated potential energy surfaces, and in principle, one would have to perform nuclear quantum dynamics on these highly coupled surfaces to properly describe the non-radiative processes. This is, however, beyond the scope of this work, as I aim only at identifying the qualitative aspects of the non-radiative decay. From my calculations, however, it is clear that the initial decay from the ππ* manifold into the lowest S_1 state is highly efficient.

Since isolated azobenzene undergoes E->Z isomerization as the main non-radiative decay channel when it reaches the lowest nπ* state after initial photo-excitation into its bright ππ* state, I also tested this possibility for CTA. Therefore, a relaxed scan along this isomerization coordinate has been performed (Fig. 4.24b). One of the azo-units has been chosen as the reaction coordinate and its dihedral angle was successively twisted and frozen, while all other geometrical parameters were allowed to relax freely on the first excited state surface of CTA. Following the relaxation on the lowest nπ* state (S_1), the energy difference between the ground state and the S_1 state becomes quite small in the region of the CNNC dihedral angle of 90° to 110° (Fig. 4.24b). Such proximity indicates the presence of a conical intersection between the S_1 and S_0 potential energy surfaces. The conical intersection appears to be slightly uphill on the S_1 potential energy curve along the torsional pathway from the *E*,*E*,*E*-isomer side. Usually such sloped conical intersections are very efficient, but in this case it does not lead to *trans*→*cis*

isomerization due to the remaining high energy barrier. Nevertheless, the molecules arriving from higher ππ* states carry significant amount of vibrational energy, which might be sufficient to overcome the barrier (this is less likely in the case of the nπ* excitation). One should note here that at the optimized S_1 geometries the S_1 and the S_0 potential energy curves are in general very close even at 180° of the dihedral angle (Fig. 4.24b). This significantly increases the probability for internal conversion prior to relaxation on the S_1 potential energy surface. Hence, even if a conical intersection appears on the S_1 (nπ*) surface of CTA it is still very likely that the molecule relaxes to the ground state directly and thus displays a very short S_1 lifetime.

4.4.4 Summary

In conclusion, my quantum chemical calculations demonstrate why no isomerization of *E,E,E*-CTA was observed in the corresponding experiments [70-71, 205]. The high density of closely spaced excited states leads to fast relaxation of the excited molecule to the lowest lying excited states. The lack of a significant angle change is due to the strained structure of CTA, which leads to a high energetic barrier along the reaction coordinate towards the *trans*-isomer. The close proximity between the S_1 and S_0 potential energy curves, allowing fast internal conversion, and the absence of a potential energy minimum at the 90° geometry prevent the formation of an *Z,E,E*-CTA isomer. The molecular strain in CTA shifts a conical intersection between S_1 and S_0, which is well-known in isolated azobenzene to be located at 90˚, to a larger dihedral angle of 110˚. This converts the conical intersection from an efficient *trans* to *cis* pathway to an efficient non-radiative pathway back to the original *trans*-state, accounting for the high stability of the *E,E,E*-CTA isomer. In summary, the CTA molecule represents an ideal photo-stable nanoscale light-to-heat energy converter with numerous application possibilities.

Chapter 5

Restricted virtual space (RVS) approximation for ADC schemes

5.1 Background and Motivation

In this chapter, I will turn to excited state calculation methods and will address the issue of an effective approximation for calculations of excited states for the sake of enhanced computational efficiency. Nowadays, the accurate description of excited states of medium-sized and large molecular systems and their properties within *ab initio* quantum chemistry methods have attracted growing attention [37, 41]. The demand for time-saving and accurate calculations of excited states has already led to various corrections for high-level quantum chemistry approximation methods that offer a good compromise between accuracy and computational effort. In theory, the larger the basis set, the more accurate the excited state calculation. As is well known, with increasing size of the basis set or the number of electrons, the computational cost of high-order

quantum chemical methods becomes quite high. Specifically, the computational effort of many typical wavefunction based methods, such as the coupled cluster singles and doubles method (CCSD) [38], the corresponding equation-of-motion and and linear-response coupled cluster (LR-CC, EOM-CC) method [39, 87, 129, 207], the complete active space self consistent field (CASSCF) method [43-44], the complete active space second-order perturbation theory (CASPT2) method [45-47], the multi-reference configuration interaction (MRCI) method [89-90], and the algebraic diagrammatic construction (ADC) method [40-42, 91-94], scale steeply with the size of the basis sets. Therefore, an accurate description and prediction of a broad range of molecules remains a great challenge for computational chemistry.

An effective way of lowering the computational effort of excited state calculations has emerged via reduction of the virtual orbital space within high-level correlation methods [208-219]. In general, the inner core orbitals can be excluded in excitation energy calculation in most practical applications since they provide only a negligible contribution to differential electron correlation. Similarly, a small segment of high-lying virtual orbitals is also considered to have an insignificant effect on the electron correlation calculations of the low-lying excited states and neglecting them therefore leads to no significant loss of accuracy compared with full virtual orbital space (FVS) calculations. When the core orbitals and a fraction of high-lying virtual orbitals are truncated simultaneously, considerable computational savings for the restricted virtual space (RVS) calculations with negligible errors can be expected. Therefore, it is possible to reach a good compromise between the accuracy and computational effort by freezing core orbitals and a part of the highest virtual orbitals.

Previously, the truncation of the highest virtual orbitals in many high-level correlation approaches has been proposed [211, 215-216, 220]. As early as in the 1980s, Hada *et al*. [211] proposed an approximation in the multiconfigurational self-consistent field (MCSCF) method by means of the reduction of the core orbitals and some of the high-energy virtual orbitals. Since the intergral transformation steps of each SCF iteration are simplified, the computational demand dramatically decreases and the accuracy of the total energy and Hellmann-Feynman force remains accurate compared with full MCSCF

calculations. Furthermore, freezing of all σ and σ* oribtals was applied for studying extended graphene nanoflakes at the correlated multi-reference level [215].

Recent advances in quantum chemistry have made it possible to use the RVS approximation in the calculations of excited states. For example, a dropped molecular orbital space employed in the analytic gradient method for an excited state within the equation-of-motion coupled cluster singles and doubles (EOM-CCSD) method was introduced by *Baeck* and *Jeon* in 2000 [216]. The authors provided the possibility of qualitative studies for the geometries and vibrational properties of the ground and excited states with the drop-MO method. Most recently, *Send et al.* studied a RVS approximation for coupled cluster excitation energies at the approximate singles and doubles level of theory (CC2) [220]. The RVS calculations show that most of the high-lying virtual orbitals can be restricted without introducing significant errors in the CC2 excitation energies, leading to a significant saving in computational cost [221-222].

The other two popular approaches that can minimize the size of the basis sets for high-level correlated methods with a negligible error are the optimized virtual orbital space (OVOS) [223-229] and the frozen natural orbital (FNO) [230-233] approaches. The optimized virtual orbital space method proposed by *Adamovicz* and *Bartlett* [223-224] has been used successfully to calculate correlation energies and molecular properties with good accuracy. This OVOS method employs the Hylleraas functional and a Newton-Raphson technique to optimize a set of active, optimized virtual orbitals. It has been frequently applied to different high-level correlated approaches. Another popular way is the FNO approach which also has many successful examples in practice. The FNO truncation coupled cluster approach has been proposed by *Taube* and *Bartlett* [225-226] to investigate the truncation error introduced by the reduction of the virtual space at the CCSD(T) level with different basis sets, yielding fairly accurate CC correlation energies, compared with the full virtual space results. Moreover, *Landau et al.* [232] employed the FNO approach to open-shell ionized electronic states within equation-of-motion coupled cluster (EOM-CC), allowing for a small segment of natural occupied and a part of virtual orbital space to be simultaneously truncated with negligible error.

Chapter 5. RVS-ADC

Recent developments of the algebraic diagrammatic construction (ADC) scheme for the polarization propagator has shown that it can provide remarkably accurate descriptions of electronically excited states [234-237]. More specifically, ADC(2) has even proved to be slightly more efficient than CC2 with a similar precision in the treatment of singly excited states [237-238]. Furthermore, the third-order scheme ADC(3) offers a balanced description of the valence excitation spectrum and thus further improves the accuracy of calculated electronic excitation energies [237]. This approach not only allows for accurate vertical excitation energy calculations, but also provides highly accurate descriptions of molecular properties such as dipole moments and nuclear gradients [238], as well as molecular response properties, *e.g.,* two-photo absorption properties [239], polarizabilities [240] and indirect nuclear spin-spin coupling constants [241]. However, the high computational cost, in particular using large basis sets, limits the applicability of ADC-based approaches to small and medium-sized molecular systems. In fact, a lot of work has been carried out on this issue. To the best of my knowledge, the ADC scheme employing the RVS approximation has not yet been exploited and is likely to be more efficient than standard ADC calculations. In light of the importance of the low-lying excited states of most organic molecules in photochemical processes and their potential use in technical applications, I implemented the RVS approximation for ADC schemes (RVS-ADC) in the hope of extending ADC calculations of low-lying excited states to medium-sized and large organic molecules with large basis sets.

In this chapter, the RVS-ADC method for vertical excitation energies of low-lying excited states is evaluated, allowing both reduction of the core and a certain proportion of the virtual orbital space. Firstly, the RVS errors of the lowest excitation energies are tested, using ADC(2) with different sizes of molecular orbital space. Secondly, to evaluate the performance of different basis sets with the RVS-ADC approach, three different standard basis sets developed by *Dunning* [242-243], *Pople* [244-245] and *Ahlrichs* [246-248] are employed in the RVS-ADC excitation energy calculations. Moreover, an improvement of the RVS-ADC approach is demonstrated by ADC(3) calculations on the pyridine molecule. Finally, the timing of the RVS-ADC schemes relative to the percentage of the restricted virtual orbital space is illustrated.

The main purpose of this work is to evaluate the performance of the RVS approximation in ADC schemes for the calculation of vertical excitation energies of low-lying excited states. Due to the lack of a unified cutoff criterion to choose the number of restricted virtual orbitals, previous studies used various ways to retain useful virtual orbitals such as the frozen natural orbitals (FNOs) [231-232] and the reduction of the virtual orbital space above a certain energy threshold [220]. Here, I will employ two different cutoff criteria: one is the percentage of the restricted virtual orbital space (PRVS), and the other is the normalized threshold of frozen virtual orbital space (NVT). The NVT was obtained by dividing the virtual orbital energy threshold by the HOMO-LUMO gap. One can readily use the NVT to specify the number of restricted virtual orbitals by means of an evaluation of the HOMO-LUMO gap energy. Another goal of this chapter is to investigate the influence of different types of basis sets on the RVS-ADC approach. In addition, the accuracy and efficiency of RVS-ADC(2) and RVS-ADC(3) are benchmarked via timing analyses with respect to PVRS.

It has to be noted here that parts of the contents of this chapter has been published in:

Chong Yang and Andreas Dreuw

Evaluation of the restricted virtual space (RVS) approximation in the algebraic diagrammatic construction (ADC) scheme for the polarization propagator to speed-up excited-state calculations. *J. Comput. Chem.*, **2017**, in print, DOI: 10.1002/jcc.24794.

5.2 Computational Methods

To investigate the effects of the restricted virtual orbital space approach on the ADC excitation energies, I computed the excited states of several representative organic molecules using basis sets of different sizes. The accuracy and reliability of RVS-ADC is quantified by the excitation energy error, which is defined as the energy difference between the RVS and the full virtual orbital space (FVS) ADC excitation energies. A

smaller error indicates that the RVS-ADC approach guarantees accuracy of the excitation energy compared with the FVS calculation. In order to cover as many organic molecules as possible, several representative organic compounds including different molecular structures were considered. In particular, I considered three typical molecules: indole, octatetraene and pyridine as shown in Fig. 5.1, which will be discussed in more detail later. All ADC calculations were carried out with the Q-Chem 4.3 program package [177]. The geometries of the ground state of the tested organic molecules were optimized with second-order Møller-Plesset perturbation (MP2) theory (114, 126) using the cc-pVTZ basis set as well as the resolution of the identity (RI) approximation [129, 249].

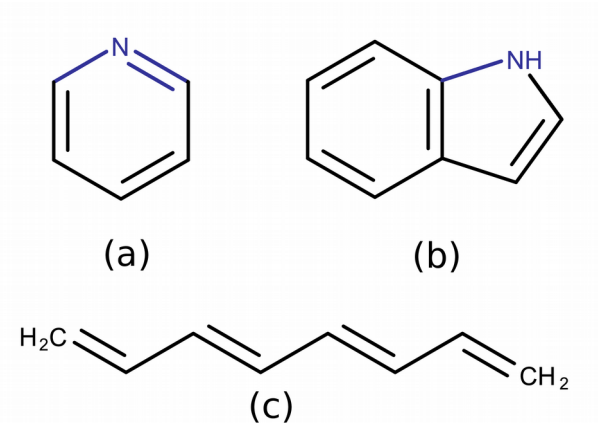

Figure 5.1: Molecular structures of the studied molecules: (a) pyridine; (b) indole; and (c) octatetraene.

For comparison, the excited state calculations of these molecules were calculated at the ADC(2) level of theory using three different standard basis sets: cc-pVTZ, 6-311G*, and def2-TZVP. I benchmarked the performance of the RVS-ADC scheme for excitation energies with two different truncation criteria, on the one hand, in order to better understand the effect of the high-lying restricted virtual orbital space on the low-lying excited states, and on the other hand to make the RVS-ADC scheme more generally applicable. Moreover, the calculations were performed on pyridine at the RVS-ADC(3) level using the def2-TZVP basis set as well. Then, an analysis of the resulting ADC(3) calculation is reported, and also comparisons are made with ADC(2)

calculations. In addition, I present timings for excitation energy calculations versus the percentage of the restricted virtual orbitals at the ADC(2) and ADC(3) level of theory with the def2-TZVP basis set. Note that all timing calculations of pyridine were computed one by one on the same computer, respectively. In this work, all calculations with the RVS-ADC approach are reported employing the frozen core approximation additionally.

As has been reported previously [220], the virtual orbital space was divided into two parts: the lower virtual orbitals and the highest virtual orbitals. The latter can be restricted artificially without affecting the results due to the insignificant contribution of the highest virtual orbitals to the low-lying vertical excitation energies. Moreover, the restricted virtual orbitals should be well separated energetically from the rest of the virtual orbital space. In general, this reliable and convenient RVS-ADC approach will be sufficient to meet the demands of most benchmarking studies.

5.3 RVS-ADC: Octatetraene and Indole

In this section, I show three representative examples to investigate the accuracy and reliability of the RVS-ADC approach with different types of basis sets. The performance of the RVS approximation in the ADC scheme with three standard basis sets using two different truncation criteria is studied by means of the analysis of the energy error. In theory, the error should be smaller than a certain tolerance value to guarantee the accuracy of the result. Considering the average error for vertical excitation energies based on most *ab initio* quantum chemistry methods, the error for the RVS-ADC can be set below 0.05 *eV* so that it is still accurate enough to meet the requirement of benchmarking studies. For the sake of improvement of RVS-ADC, I have carried out calculations of RVS-ADC(3) excitation energies on pyridine to make a comparison to RVS-ADC(2) calculations. In particular, it is interesting to note that the truncated highest virtual orbitals and core orbitals are also absent in RVS-ADC(2)

calculations, while this issue can be solved by RVS-ADC(3). Relevant to the loss in correlations, I refer to the effect of orbital relaxation on the correlation energy later.

I choose octatetraene and indole as examples in this section. Octatetraene is a representative of the linear polyenes, possessing low-lying ππ* states with a conjugated π-system. Furthermore, indole is a typical aromatic heterocyclic molecule which has distinct low-lying nπ*and ππ* states.

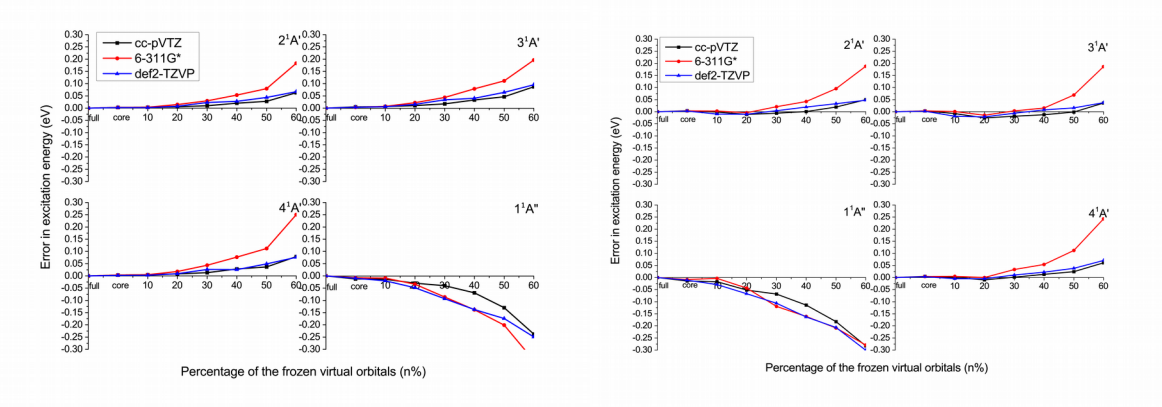

Figure 5.2: The relative error of excitation energies (eV) of the first four lowest excited states of octatetraene (left) and indole (right) as a function of the pecentage of the restricted virtual orbital space using the RVS approximation at the ADC(2) level of theory with the cc-pVTZ, 6-311G and def2-TZVP basis sets.*

Figure 5.2 shows the RVS error of the first four vertical excitation energies of the low-lying excited states versus the percentage of the restricted virtual orbitals with three different standard basis sets. As seen in Fig. 5.2, the excitation energies of the low-lying excited states with frozen core orbital approximation are almost identical to the results of the FVS calculations. The errors in all frozen core cases are small and the effects of the restricted core orbitals on the vertical excitation energies are negligible, as proposed previously [211, 219, 231]. Moreover, I observed that the error of the first four low-lying excited states increases slowly with increasing percentage of the restricted virtual orbital space. Specifically, the excitation energy errors of the lowest excitation energies are lower than 0.05 *eV* for the 2^1A', 3^1A' and 4^1A' excited states in both cases, if the

truncation of virtual orbital space is less than 50%. However, the deviation of the $1^1A''$ excited state is a little more sensitive to the truncation of the high-lying virtual orbital space compared to other excited states, and the error is slightly larger than that of other excited states with the same percentage of the restricted virtual orbitals. In other words, freezing 30% of the virtual orbitals, with the exception of the cc-pVTZ calculations, the truncation errors become larger than 0.05 *eV* using the 6-311G* and def2-TZVP basis sets. As a result, even a small percentage of frozen virtual orbital space may also lead to larger errors for these excited state, which are beyond the standard tolerance value. This shows the importance of the highest virtual orbitals for describing the correlation energy with respect to some unique low-lying excited states. Additionally, it is also worthwhile to note that a similar behavior is observed not only in the cases of octatetraene and indole but also in other test examples.

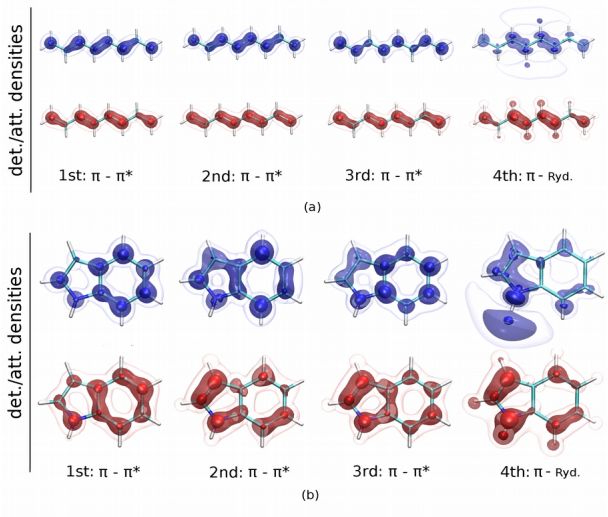

Figure 5.3: Isosurfaces for attachment (blue) and detachment (red) densities for the first four lowest excited states for octatetraene (a) and indole (b) at the ADC(2)/def2-TZVP level of theory.

The transition nature of the $1^1A''$, $2^1A'$, $3^1A'$ and $4^1A'$ excited states is shown in Fig. 5.3. It was demonstrated that the $1^1A''$ excited state has Rydberg character, whereas the $2^1A'$, $3^1A'$ and $4^1A'$ excited states are $\pi\pi^*$ states. As to the problem of how to explain these

exceptional excited states, I will refer to orbital relaxation in the following. Here, according to my calculations on the $2^1A'$, $3^1A'$ and $4^1A'$ excited states, it still demonstrates that a large number of high-lying virtual orbitals can be restricted for excitation energy calculaltions of most low-lying excited states without introducing a significant error, compared to the FVS-ADC calculations.

The other deduction from Fig. 5.2 is that the excitation energy error versus the percentage of the restricted virtual orbital space in both cases displays very similar features for the three different standard basis sets. The errors for all three different basis sets increase slowly with increasing the percentage of the restricted virtual orbital space (PRVS). In principle, the larger the basis sets, the better the accuracy. As expected, the 6-311G*, the smallest basis set, yields larger errors than the def2-TZVP and cc-pVTZ basis sets. Furthermore, it also indicates that the virtual orbital space even can be truncated by 50% for a larger basis set, i.e. def2-TZVP and cc-pVTZ, while the errors of the $2^1A'$, $3^1A'$ and $4^1A'$ excited states for octatetraene and indole are still in a reasonable range. In contrast, the error of the $1^1A''$ excited state with all three different basis sets becomes slightly larger relative to the PRVS. This error is smaller than 0.05 *eV* with 30% truncated virtual orbital space only when the large cc-pVTZ basis set is used. Thus, one has to realize that the deviations of the excitation energies relative to the truncation of high-lying virtual orbitals in most cases are dependent on the size rather than the type of basis sets. In general, RVS-ADC can be used for excitation energy calculations with various basis sets, reducing even more than 50% of FVS for some large basis sets, while the computational cost decreases drastically.

5.4 Pyridine

To investigate the effect of $n\pi^*$ and $\pi\pi^*$ states on the RVS-ADC excitation energy calculations, I further calculated the errors of the first four lowest excitation energies of pyridine. Pyridine is a representative aromatic organic compound and it also has low-

lying nπ* and ππ* states. Fig. 5.4 shows that the error of the 1^1A" and 2^1A" excited states with all three basis sets no longer presents the linear dependency with increasing PFVS. Apparently, the RVS errors of both excited states are connected to the restricted virtual space and the deviations become rapidly larger than 0.05 *eV* when only freezing a small fraction of the high-lying virtual orbitals. The largest error of 0.16 *eV* for the 2^1A" excited state with the cc-pVTZ basis occurs when 30% restricted virtual orbital space is used. Unexpectedly, the larger cc-pVTZ basis set shows worse performance in accuracy compared to the 6-311G* and def2-TZVP basis sets in the RVS-ADC calculations. On the contrary, the relative errors for the 2^1A' and 3^1A' excited states versus the percentage of the restricted virtual orbital space are clearly seen in Fig. 5.4. This shows that the results of some low-lying excitation energies with the RVS-ADC approach are still very promising and these errors are also in line with the behavior of the 2^1A', 3^1A' and 4^1A' excited states in the cases of octatetraene and indole as discussed above. In theory, the higher excited states should be affected strongly by the restricted high-lying virtual orbitals since the orbital relaxation effect might be better described by the restricted virtual orbitals for the higher excited states. However, in this case, I found that the same number of restricted virtual orbitals possibly plays different roles in the calculation of the lowest excitation energies for different low-lying excited states. In effect, the accuracy of the RVS-ADC approach for the lowest excitation energies depends not only on the size and quality of the selected basis sets but also on the transition character of the required excited states.

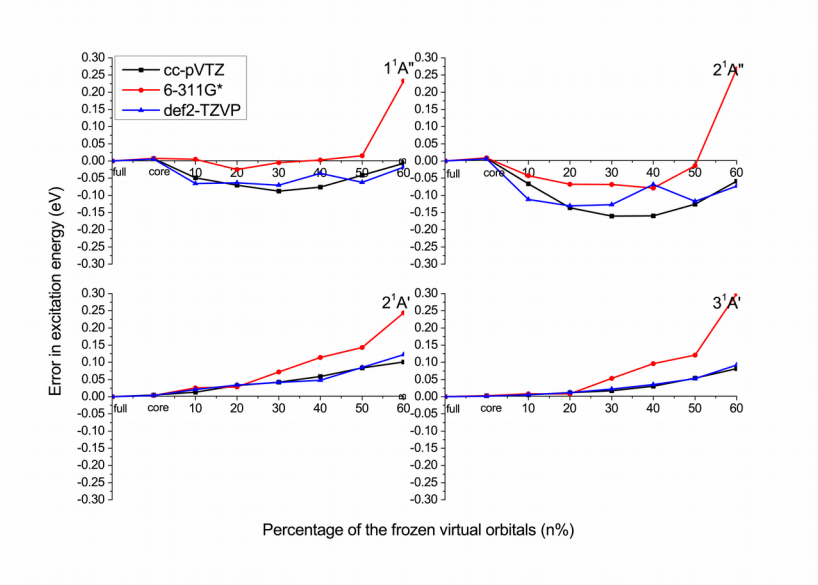

Figure 5.4: The relative error of excitation energies (eV) of the first four lowest excited states for pyridine as a function of the percentage of the restricted virtual orbital space using the RVS approximation at the ADC(2) level of thory with the cc-pVTZ, 6-311G and def2-TZVP basis sets.*

In order to determine the characteristics and the application range of the RVS-ADC approach, I studied the transition character of the low-lying excited states via detachment and attachment densities of the lowest excited states, which are shown in Fig. 5.5. The graphical representation of the 1^1A" and 2^1A" excited states clearly indicates that both excited states are identified as nπ* states and they obviously possess some charge transfer character, whereas the 2^1A' and 3^1A' excited states are characterized as ππ* transitions. As exhibited in Fig. 5.4, the error for the 1^1A" and 2^1A" excited states are susceptible to the truncation of the virtual orbital space, whereas the higher 2^1A' and 3^1A' excited states yield relatively small errors. Remarkably, the accuracy of the RVS-ADC approach is readily available for these lowest excited states due to the ππ* transition. The reason why the RVS-ADC approach is more successful in the low-lying excited states which have ππ* character, one possible explanation, as mentioned above, is that the orbital relaxation effect which is described by the restricted highest virtual orbitals has little influence on the low-lying ππ* excited states.

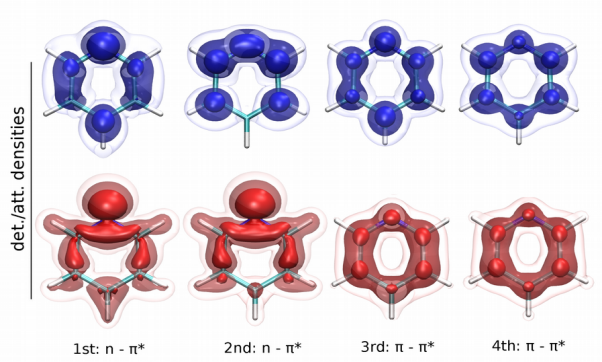

Figure 5.5: Isosurfaces for attachment (blue) and detachment (red) densities for the lowest excited states for pyridine at the ADC(2)/def2-TZVP level of theory.

Apparently, the low-lying nπ* excited states are more likely to be affected by orbital relaxation effect. The contribution introduced by the relaxation effect to the excitation energy of the low-lying ππ* excited states are probably cancelled out by each other, particularly in the case of the conjugated π system, since the orbital rotation cannot change the second-order energy for the ππ* excited states.

Moreover, I further present results of the root-mean-square (RMS) errors of the RVS-ADC(2) approach summed over eight organic molecules given in Table 5.1. It is found that the RMS error is smaller than 0.05 *eV* for the cc-pVTZ and def2-TZVP basis sets using the RVS-ADC even when up to 50% of the full virtual orbital space is restricted, while it has a considerable error at the same truncation level for smaller basis sets, e.g, the 6-311G* basis set. The result is in line with the behavior of each individual molecule. Therefore, the conclusion is that the RVS-ADC approach can offer acceptable lowest excitation energy calculations and is also more effective and applicable for estimating the lowest excitation energies of the low-lying ππ* excited states. In view of the complicated orbital relaxation effect, I attempted to use the higher order ADC(3) method to compensate the loss of double excitation description of RVS-ADC(2) excitation energies of the nπ* states. In the next section, I will present a successful improvement of the RVS-ADC approach.

			The percentage of the restricted virtual orbital space						
Basis set	Error	full	core	10%	20%	30%	40%	50%	60%
cc-pVTZ	RMS Error	0	0,0045 (±0,0021)	0,00659 (±0,0161)	0,01197 (±0,0245)	0,01499 (±0,0241)	0,02447 (±0,0239)	0,04258 (±0,0231)	0,07317 (±0,0231)
	furan	0	0,00517	-0,00947	-0,01257	-0,00914	0,00059	0,02921	0,05515
	coumarin	0	0,00381	0,006892	0,007159	0,009493	0,021793	0,040863	0,061102
	pyrimidine	0	0,00546	0,00966	0,02152	0,02714	0,03917	0,06466	0,09452
	benzene	0	0,00459	0,00614	0,01107	0,01945	0,03585	0,04974	0,08279
	indole	0	0,00426	-0,00124	-0,01114	-0,00606	0,0008	0,01953	0,05006
	oct	0	0,00245	0,00337	0,00557	0,00948	0,02035	0,02795	0,06311
	pyridine	0	0,00286	0,00555	0,01193	0,01736	0,03048	0,05358	0,08167
	guanine	0	0,00613	0,00592	0,0073	0,00904	0,01237	0,03595	0,08428
TZVP	RMS Error	0	0,00326 (±0,0016)	0,00762 (±0,0206)	0,01199 (±0,0250)	0,01840 (±0,0175)	0,03145 (±0,0173)	0,04989 (±0,0264)	0,07719 (±0,0363)
	furan	0	0,00364	-0,01299	-0,013	0,00088	0,0236	0,02345	0,04089
	coumarin	0	0,00281	0,00502	0,00503	0,01496	0,028	0,04591	0,06867
	pyrimidine	0	0,00398	0,01	0,02104	0,02552	0,0487	0,07424	0,10771
	benzene	0	0,00328	0,00617	0,01384	0,02849	0,03999	0,05642	0,09223
	indole	0	0,00308	-0,00963	-0,01027	0,00383	0,01956	0,03307	0,04772
	oct	0	0,00176	0,00209	0,0073	0,02278	0,02732	0,04368	0,06714
	pyridine	0	0,0017	0,00525	0,01172	0,02185	0,03524	0,05285	0,09167
	guanine	0	0,00467	0,00279	0,00509	0,00323	0,01511	0,05259	0,07737
6-311G*	RMS error	0	0,00382 (±0,0013)	0,01003 (±0,0120)	0,01823 (±0,0222)	0,05021 (±0,0476)	0,08081 (±0,0389)	0,11251 (±0,0330)	0,21692 (±0,0482)
	furan	0	0,00482	0,02207	0,0347	0,09776	0,10539	0,12041	0,24427
	coumarin	0	0,00329	0,0061	0,0045	0,02149	0,05649	0,09888	0,1687
	pyrimidine	0	0,00397	0,00725	0,02387	0,05317	0,09775	0,13847	0,20656
	benzene	0	0,0036	0,0061	0,01706	0,05165	0,09963	0,12091	0,19934
	indole	0	0,00361	0,00278	-0,00399	0,02052	0,04194	0,09556	0,18775
	oct	0	0,00252	0,00356	0,0144	0,02962	0,05294	0,07955	0,18327
	pyridine	0	0,00285	0,00863	0,00864	0,05291	0,09621	0,12121	0,29924
	guanine	0	0,00514	0,00978	0,01659	0,02355	0,06812	0,1142	0,218

Table. 5.1: The RMS Error (eV) summed over eight organic compounds. The error of the excitation energies of these eight compounds calculated with ADC(2)/cc-pVTZ, ADC(2)/def2-TZVP and ADC(2)/6-311G using the RVS approximation. The errors of each compound were all selected from the low-lying π-π* excited states.*

5.5 Comparison of RVS-ADC(2) and RVS-ADC(3)

Fig. 5.6 shows the excitation energy error of the lowest excitation energies of pyridine versus the percentage of the frozen virtual orbital space. The calculations were performed on pyridine at the ADC(2) and ADC(3) level of theory using the def2-TZVP basis set. The error of the 1^1A" and 2^1A" excited states at the ADC(3) level of theory is much less than that of the ADC(2) calculations. As expected, the errors of the four lowest excited states are smaller than 0.05 *eV* when less than 40% frozen virtual orbital space are restricted in ADC(3)/def2-TZVP calculations.

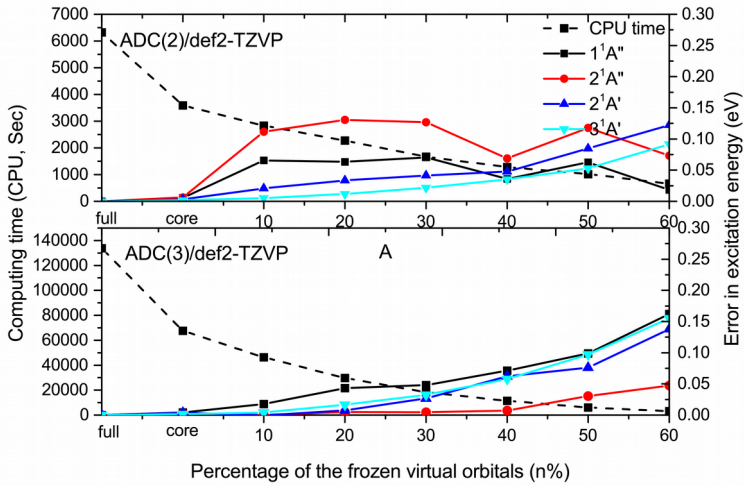

Figure 5.6: CPU time (sec) and the absolute values of the errors (eV) of the first four lowest excited states for pyridine as a function of the percentage of the restricted virtual orbital space using the RVS approximation at the ADC(2) (top) and ADC(3) (bottom) level of theory with def2-TZVP basis set, respectively. The 2^1A' and 3^1A' excited states have ππ character.*

Apparently, the errors introduced by RVS-ADC(2) are greatly improved by RVS-ADC(3). In fact, the most remarkable feature is that only the errors for 1^1A" and 2^1A" excited states that involve nπ* character are significantly diminished by the RVS-ADC(3) approach, as demonstrated in Fig. 5.6 (bottom). By contrast, the 2^1A' and 3^1A'

excited states are not affected strongly by the third order ADC(3) scheme with the RVS approximation. This suggests that the improvement of accuracy for $1^1A"$ and $2^1A"$ excited states with RVS-ADC(3) may originate from the accurate treatment of double excitations with the third order ADC(3). In other words, the contributions of the double excitation advantageously may cancel out errors caused by orbital relaxation effects on low-lying nπ* excited states. Hence, the large errors introduced by the RVS approximation in ADC(2) calculations can be corrected by the third order ADC(3) scheme even when the low-lying excited states have nπ* character, thereby enlarging the application range of the RVS-ADC approach.

Figure 5.6 also presents the computational time (CPU time) and the error of the lowest excitation energies versus the percentage of the restricted virtual orbitals of pyridine. In Fig. 5.6 (top), I used the absolute value of the error of the $1^1A"$ and $2^1A"$ excited states, so it is much easier to observe and compare the error of these excited states. Obviously, the total CPU time in both ADC(2)/def2-TZVP and ADC(3)/def2-TZVP calculations decreases dramatically with increasing the percentage of the restricted virtual orbital space. By freezing only 30% of the virtual orbital space the RVS-ADC(2) calculation just needs roughly 26% CPU time compared to an FVS calculation and even better, the RVS-ADC(3) calculations only need 14% CPU time, while the RVS-ADC(3) truncation error is still smaller than 0.05 *eV*. The prefactor of computational cost with 30% restricted virtual orbital space is four for RVS-ADC(2) and seven for RVS-ADC(3) calculations, respectively. Thus, I conclude that the overall performance of RVS-ADC is improved if the third order ADC(3) is considered and the RVS-ADC approach offers greater accuracy and significantly lower computational cost for vertical excitation energy calculations, allowing the calculation of the lowest excitation energies without a significant loss in accuracy for most benchmarking studies.

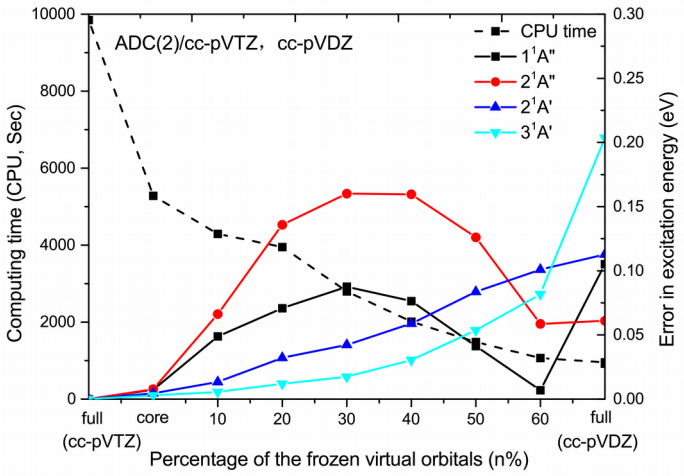

Figure 5.7: CPU time (Sec) and the absolute values of the errors (eV) of the $2^1A'$ and $3^1A'$ excitation energies of pyridine versus the percentage of frozen virtual and core orbitals in ADC(2)/cc-pVTZ as well as FVS ADC(2)/cc-pVDZ calculations.

For the sake of comparison, the efficiency and accuracy of the RVS-ADC(2) approach with the cc-pVTZ and cc-pVDZ basis sets have been studied in more detail. As shown in Figure 7, similar to the benchmark using the def2-TZVP basis set above, the total CPU time of the RVS calculations at the level of ADC(2)/cc-pVTZ decreases as the number of restricted virtual orbitals increases, whereas the errors of the $2^1A'$ and $3^1A'$ excited states are still within a reasonable scope. I observed that the errors of the $2^1A'$ and $3^1A'$ excited states in RVS-ADC(2)/cc-pVTZ calculations are smaller than those of FVS-ADC(2)/cc-pVDZ even if 60% of the total virtual orbital space is restricted. In theory, the results of excitation energy calculations with the large cc-pVTZ basis set should be more accurate than those with the small cc-pVDZ basis set. At this point, it is instructive to compare the result of RVS-ADC(2)/cc-pVDZ calculations with those using the cc-pVTZ basis set at the same truncation level. Table 5.2 presents vertical excitation energies of the first four low-lying excited states employing the RVS-ADC(2) approach with the cc-pVDZ and cc-pVTZ basis sets, respectively. It shows the percentage of the restricted virtual orbitals and the corresponding number of the virtual orbitals (NVO) to be used in the RVS calculations. As expected, the triple zeta basis set for RVS-ADC calculations performs quite well compared to the double zeta basis set at

the same truncation level. This implies that the small basis sets are more sensitive to the variation of the basis set size in RVS-ADC calculations. Furthermore, I have found that 60% truncation of the virtual orbitals in calculations with the triple zeta basis set is even superior to the result with the FVS double zeta basis set. That is, even if 60% of the full virtual orbital space is restricted in RVS-ADC(2) calculations with the cc-pVTZ basis set, the result is still much better than the result of FVS-ADC(2) calculations with the double zeta basis set at roughly the same computational cost. That is why the RVS-ADC approach not only holds promise for remarkable accuracy and efficiency but also reveals distinct advantages of high quality basis sets with the RVS approximation in comparison to conventional wavefunction based methods.

PRVS	NVO		1A"		2A"		2A'		3A'	
			$n \rightarrow \pi^*$		$n \rightarrow \pi^*$		$\pi \rightarrow \pi^*$		$\pi \rightarrow \pi^*$	
	cc-pVDZ	cc-pVTZ	cc-pVDZ	cc-pVTZ	cc-pVDZ	cc-pVTZ	cc-pVDZ	cc-pVTZ	cc-pVDZ	cc-pVTZ
full	88	229	5.16197	5.05612	5.4001	5.33942	5.52620	5.41339	7.00091	6.79713
core	88	229	5.16599	5.06334	5.40613	5.34725	5.52714	5.4179	7.00167	6.79999
10	79	206	5.10961	5.00728	5.33424	5.27325	5.54229	5.42677	7.00608	6.80268
20	70	183	5.12062	4.98539	5.29591	5.20353	5.57842	5.44562	7.03701	6.80906
30	62	160	5.14796	4.96841	5.35459	5.17925	5.61245	5.45563	7.08562	6.81449
40	53	137	5.12165	4.97979	5.35276	5.17975	5.61934	5.47219	7.09867	6.82761
50	44	114	5.20907	5.01486	5.45877	5.21342	5.67659	5.49701	7.18327	6.85071
60	35	92	5.53076	5.04921	5.76470	5.28082	5.78570	5.51440	7.32428	6.87880

Table 5.2: Excitation energies(eV) of pyridine at the ADC(2)s level using the RVS approximation. PRVS represents the percentage of the restricted virtual orbital space. NVO means the number of the virtual orbitals to be used in the RVS calculations.

5.6 Normalized Virtual Orbital Energy Threshold (NVT)

The vertical excitation energies and the oscillator strengths of indole have been calculated with the RVS-ADC(2) approach using the def2-TZVP basis set. Table 5.3 summarizes the vertical excitation energies and the oscillator strengths of the low-lying excited states for indole with a new cutoff criterion: the normalized virtual orbital energy threshold. The definition of the NVT was mentioned above by dividing the virtual orbital energy threshold with the HOMO-LUMO gap. For the convenience of comparison, the corresponding PFVS relative to the NVT are listed as well. NVT can be easily applied to the treatment of the input parameters and provides a reliable controllability as well as the RVS-ADC approach is implemented into Q-Chem or other program packages. The excitation energy calculations of the first four low-lying excited states show that the errors of the vertical excitation energies with respect to the NVT values are smaller than 0.05 *eV* until the truncation level of the NVT value is below roughly 8 for the $2^1A'$, $3^1A'$ and $4^1A'$ excited states. The error of the vertical excitation energies of the $1^1A''$ excited state deviates more strongly from the other excited states using the same NVT value. However, the negligible errors between the RVS and the FVS results of the low-lying $\pi\pi^*$ excited states demonstrate the usefulness of the RVS-ADC approach and the practicality of NVT. From what has been discussed above, one may safely draw the conclusion that, if the NVT is above a certain value, the RVS-ADC approach holds promise of accuracy of the excitation energy calculation for low-lying excited states, particularly for the excited states which possess $\pi\pi^*$ transition character.

Additionally, it was found that the error of the oscillator strength is also affected by the truncation of the high-lying virtual orbitals as shown in Table 5.3. The magnitudes of the oscillator strengths of the $3^1A'$ and $4^1A'$ excited states are recovered by more than 96% and 97% compared to the result of the FVS-ADC calculation, respectively, if the NVT value is greater than or equal to 8 (PFVS≈44%). This implies that the effect of

the truncation of the high-lying virtual orbitals on the oscillator strength of low-lying excited states is quite small, especially for “bright states”.

		The vertical excitation energies (eV) & oscillator strengths							
state	NVT	3	5	8	10	13	15	core	full
	PRVS	77%	59%	44%	23%	12%	5%	0%	0%
2A'		5.0010	4.80647	4.79753	4.76317	4.75815	4.77328	4.77511	4.77203
		(0.039916)	(0.040014)	(0.035708)	(0.035987)	(0.035353)	(0.032447)	(0.032115)	(0.031981)
3A'		5.24298	5.04548	5.04026	5.00858	5.00349	5.02772	5.03100	5.02864
		(0.120689)	(0.103070)	(0.108963)	(0.102685)	(0.103233)	(0.111914)	(0.112924)	(0.112671)
4A'		6.54413	6.32388	6.30293	6.27200	6.26638	6.27698	6.27817	6.27496
		(0.862050)	(0.847910)	(0.825436)	(0.831890)	(0.827738)	(0.807263)	(0.804610)	(0.804247)
1A"		5.81521	5.99335	6.10292	6.19949	6.23716	6.27072	6.26710	6.27821
		(0.000000)	(0.000008)	(0.000000)	(0.000005)	(0.000002)	(0.000006)	(0.000007)	(0.000007)

Table 5.3: Comparsion of the vertical excitation energies and the oscilator strength of the first four lowest excited states for indole with the normalized cutoff threshold of virtual orbital energy (eV). The normalized virtual orbital energy threshold (NVT) is defined as the cutoff threshold over (E_{LUMO}-E_{HOMO}). The percentages of the full virtual orbital space (PFVS) relative to the NVT value are listed as well.

Compared with the 3^1A' and 4^1A' excited states the magnitude of the 2^1A' excited state is extremely small, almost close to zero, thus, this small error hardly has any influence on the absorption spectrum calculation. In addition, I also observed that the irregular values of the oscillator strength of the 1^1A" excited state does not depend linearly on the restricted high-lying virtual orbital space, since the 1^1A" excited state is a “dark state”, the tiny error of the oscillator strength makes it insignificant. Note that the effect of the high-lying restricted virtual orbital space on the oscillator strength is similar to that on the lowest excitation energies. Both of them depend on the size of the restricted virtual orbital space as well. Although with a rather large proportion of the restricted virtual

orbital space, the RVS-ADC approach still holds the promise of accuracy, and, thereby, the negligible error of oscillator strength with a certain amount of the restricted virtual orbitals can be used for the simulation of absorption spectra employing the RVS-ADC approach with large basis sets.

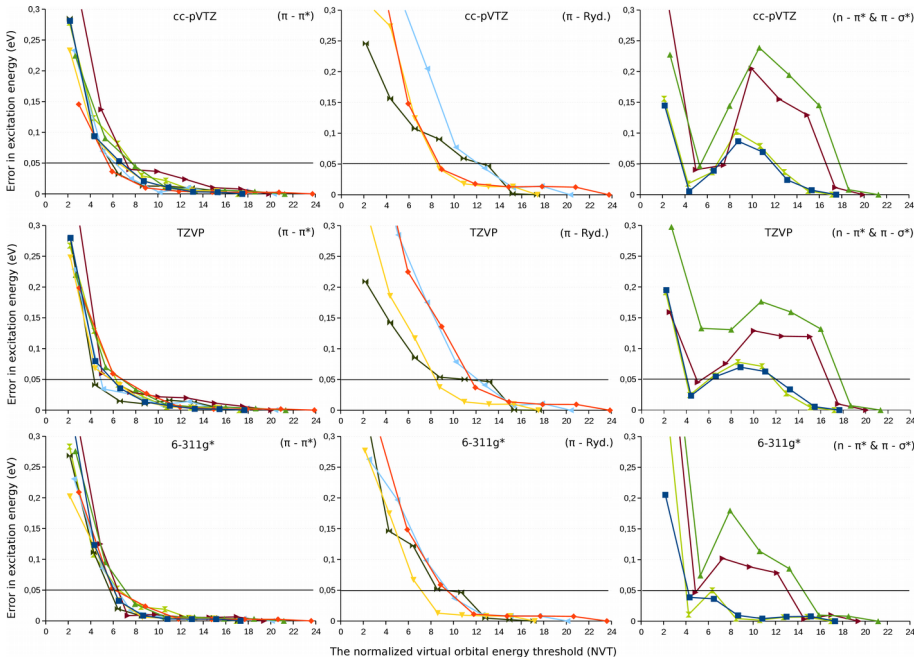

Figure 5.8: The absolute value of the error of the first ππ, πσ*, nπ* and π-Rydberg excited states versus the NVT value for the low-lying excited states of eight representative molecules (furan, coumarin, pyrimidine, benzene, indole, octatetraene, pyridine and guanine) at the RVS-ADC(2) level of theory with the cc-pVTZ, def2-TZVP and 6-311G* basis sets.*

Figure 5.8 presents the absolute values of the excitation energy errors for the low-lying excited states as a function of the NVT. In Fig. 5.8, the errors of the excitation energies of the ππ*, πσ*, nπ* and π-Rydberg excited states versus the NVT with the 6-311G*, def2-TZVP and cc-pVTZ basis sets based on the tested cases are plotted, respectively. From calculations of all benchmarked molecules, it was found that all errors of the ππ* excited states within RVS-ADC calculations are rather small, and even for nπ* and πσ* excited states the excitation energy only has a maximum error of 0.24 *eV* when the NVT value is larger than 8. As previously discussed, the error of the nπ* excited states do not

depend on the size of the restricted virtual orbital space and deviate more strongly from the standard tolerance range, which is probably attributed to the relaxation effect described by the truncated virtual orbital space as discussed above. When an electronically excited state is affirmed as a Rydberg state, the errors decline slowly with increasing NVT value in comparison with the result of the ππ* excited state, because wave functions of Rydberg states are diffuse and the high-lying virtual orbitals are relevant for their excitation energies. In addition, it was observed that the error of the ππ* excited state with all three basis sets can be quantified using the same NVT value. The errors decrease dramatically when the NVT value varies from 2 to 6, and the errors are smaller than 0.05 *eV* when the NVT value is increased to 8. However, under the same standard error, the NVT in the case of π-Rydberg states is at least 14, whereas it has to be greater than 18 in the case of the nπ* and πσ* excited states. According to my calculations, the results demonstrate that the error of low-lying ππ* excited states can be controlled in a safe range as long as a unified NVT value is set up for three different standard basis sets. Using NVT, the RVS-ADC approach not only allows a feasible and controllable implementation, but also guarantees the accuracy of the excitation energy of low-lying excited states with a great computational saving. As to the error of nπ* and πσ* excited states or π-Rydberg excited states, the problem can be solved by higher order ADC methods with the RVS approximation, such as ADC(3).

5.7 Conclusion

In the present work, I tested a restricted virtual space (RVS) approximation within the algebraic diagrammatic construction (ADC) scheme to benchmark its performance for the lowest vertical excitation energy calculations. Not only the core orbitals but a fraction of the highest virtual orbitals are restricted in the excitation energy calculations with the RVS-ADC approach, which has the advantages of high efficiency, small deviation, flexibility and low computational cost. In fact, the RVS approximation has

been successfully proven to be an efficient method by a previous investigation for CC2 excitation energies [32]. My results deepen and enrich the content of the restricted core and virtual orbital approximation for excitation energy calculations and improve the applicability and effectiveness of the ADC scheme using large basis sets with the RVS approximation.

The RVS-ADC calculations were performed for the first four low-lying excited states of octatetraene, indole, and pyridine, using different standard basis sets, i.e. 6-311G*, cc-pVTZ and def2-TZVP. The results show that the restriction of the core and a fraction of the highest virtual orbitals in ADC(2) calculations has negligible effects on the vertical excitation energies of low-lying ππ* states with three different standard basis sets. Specifically, freezing the core and less than 30% truncation of the high-lying virtual orbitals have negligible effects on the ππ* excited states, and one can even restrict the virtual orbital space by 50% for large basis sets such as def2-TZVP and cc-pVTZ.

The influence of the number of truncated virtual orbitals is generally smaller for ππ* transitions than for nπ* and πσ* transitions. As a consequence, the applicability and efficiency of the RVS-ADC(2) approach for the lowest excitation energies is significantly affected by the transition character of the low-lying excited states. When the lowest excited states are characterized as nπ* or πσ* states, the RVS-ADC(2) is no longer very promising. By contrast, π-Rydberg excited states behave better than nπ* or πσ* states. However, calculations at the level of RVS-ADC(3)/def2-TZVP on pyridine demonstrate that the accuracy and the applicability range of ADC approaches are greatly improved, since the unconventional errors of nπ* or πσ* states introduced by the RVS-ADC(2) are corrected by the third-order ADC(3) scheme.

Moreover, it is also significant that the RVS approximation with larger basis sets saves more computational cost and reproduces more accurate results compared to the smaller basis set. A comparison of the RVS excitation energies employing the cc-pVTZ basis set and the FVS excitation energies employing the cc-pVDZ basis set shows that only 40% FVS with the cc-pVTZ basis set yields a more accurate result than the overall FVS with the cc-pVDZ basis set, while using roughly the same number of virtual orbitals.

Also, the errors with different basis sets present very similar convergence characteristics when the same NVT value is used in the RVS-ADC(2) calculations. This allows one to control the desired accuracy by using a unified NVT for various basis sets.

Here, only preliminary evaluations of the RVS-ADC approach for the low-lying excited states are presented. A detailed survey of the RVS-ADC approach and calculations of the electronic properties such as the dipole moment, charge transfer and the transition dipole moment of the excited states will be addressed in the future.

Chapter 6

Conclusion and Outlook

In this thesis, I presented a series of fascinating multiple azobenzenes, which are valuable candidates to be applied as multiphotochromic switches in photoresponsive functional materials, biomolecular systems and nano-optic devices. Due to numerous potential applications of multiazobenzenes, it is attractive to exploit the underlying multiphotochromic properties and cooperative photoisomerization mechanisms towards designing robust and highly efficient coupled photoswitches. The results of this research not only provide novel and efficient multiple azobenzene structures as photoswitches for the control of long-range chemical reactions and processes, but provide further insight into the photoisomerization mechanism of azobenzene and multiazobenzenes. As is well-known, low-lying excited states play a fundamental role in the photochemical reaction process, and thus accurate quantum chemical calculations of electronically excited states for medium-sized and large molecular systems are desirable. Hence, the development of computationally efficient theoretical approaches for the calculation of excited states is rewarding. In this work, an efficient restricted virtual space (RVS) approximation for the algebraic diagrammatic construction scheme (ADC) was presented for the computation of excited states, which offers a good compromise between accuracy and computational cost.

Chapter 6. Conclusion and Outlook

Owing to complicated external enviromental factors, such as solvent effects, temperature, and irradiation wavelength, some particularly desirable electronic structures still cannot be obtained via current experimental techniques for further understanding of the photoisomerization processes. In contrast, quantum chemical approaches can provide significant insight into the electronic structure, which can account for the photoisomerization process of a system. For comparison to experimental data, an appropriate quantum chemical method for the treatment of the electronic ground and excited states of a given system is an essential part of theoretical and computational chemistry. Currently, various quantum chemical methods have been proposed for the treatment of excited states, which were addressed biefly in Chapter 2. Time-dependent density functional theory (TDDFT) is the most widely-applied method for the calculation of electronically excited states to investigate excited state properties and photo-chemical reaction processes of a system. TDDFT not only yields a good description of excited states of medium-sized and large molecular systems with reasonable computational time-savings, but also allows for the treatment of excited states in a solvent in combination with continuum sovation models. This implementation is beneficial for the study of excited states of a solvated molecules with a large number of solvent molecules. Besides, the algebraic diagrammatic construction (ADC) scheme is an effective wavefunction based method for the accurate calculation of excited states based on perturbation theory, which has been successfully used for the calculation of medium-sized to large molecules. For benchmark purposes, ADC calculations were carried out for comparsion with experimental data and TDDFT results to confirm the accuracy of selected TDDFT methods.

Previous efforts for the investigation of the photoisomerization of azobenzene have been made to develop various novel and efficient photoswitches. The recent multi-components materials containing two or even more azobenzene units call for the understanding of the underlying cooperative mechanism for the photoisomerization. However, the unique switching behavior and multiphotochromic properties of the connected azobenzenes have only scarcely been addressed. This work addressed the multiphotochromic properties and photoisomerization of two types of multiazobenes:

linear azobenzenes and non-linear azobenzenes.

In Chapter 3, at first, the absorption spectra of the parent azobenzene (AB) and the linear azobenzenes (AB-(n)) were calculated using the TDDFT/ BHLYP method with the 6-31G* basis set benchmarked against reliable wavefunction based methods and experimental data. It is found that the order of electronically excited states changes with increasing chain length. The excitation energies generally decrease but to different degrees. A significant dual band appears in the π-π* absorption band of the twisted AB-(n) due to strong excitonic coupling interaction between two roughly equal moieties. These absorption spectra contribute to the understanding of the photoisomerization of the twisted AB-(n)s due to excitonic coupling interactions. In addition, the red-shift in the π-π* band of a series of AB-(n) including not only *trans*-AB-(n) but also *cis*-AB-(n) gradually increases with increasing chain length. This is because increasing the chain length strengthens the conjugated π-system of the AB-(n).

Furthermore, relaxed scans of the S_1 potential energy surface along the CNNC rotation, CNN inversion and the concerted-inversion pathways have been computed to explore the isomerzation mechanism of AB and linear multiazobenzenes. The S_1 potential energy surface of AB and AB-(n) is essentially barrierless along the rotation pathway and a conical intersection is most likely to appear in all cases of the AB-(n). Thus, the rotation mechanism may dominate the isomerization in the n-π* state. Although a large potential barrier was found in the S_1 potential surface along the concerted-inversion pathway, this path remains an energetically favorable isomerization pathway when excited to the S_2 state or even higher excited states. Since the energy gap between the S_2 state and the S_1 state becomes smaller with increasing chain length, rapid relaxation from higher excited states to the S_1 state occurs more easily, which is helpful to overcome the potential barrier in the S_1 surface. Moreover, the relaxed potential energy curves along three different pathways with different chain lengths indicate that the concerted-inversion isomerization mechanism is significantly affected by the chain length compared to the other two paths.

In Chapter 4, several different non-linear multiazobenzenes were investigated. This

project initiated a new investigation of the structures and absorption spectra for *o-, m-* and *p*-bisazobenzenes to obtain highly efficient photoswitching multiazobenzenes. The absorption spectra of AB, *o-, m-* and *p*-bisazobenzenes in trans (*E*), cis (*Z*) and *E,Z*-isomerization states were calculated in the gas phase and in solution, respectively. Surprisingly, a significant dual band only appears in the gas-phase and the solvent absorption spectra of *o*-bisazobenzene due to its intramolecular excitonic interactions between two individual azo subunits. The spectral properties of *m*-bisazobenzene are very similar to the monomeric azobenzene but feature a two times higher intensity, which indicates decoupling of two azo subunits. Therefore, two sub-azo units of *m*-bisazobenzene can be switched independently from each other. In addition, *p*-bisazobenzene shows a strong π conjugation extending over the two azo subunits, leading to strong planarity of the molecule. Furthermore, an extension to tris-azobenzene containing three azobenzene units connected via a central phenyl ring was taken into account. Previous studies [57, 60] found that the absorption spectra of substituted azobenzenes have different spectral shifts due to various electron donating and withdrawing substituents. To obtain efficient separation in the absorption spectra corresponding to three different azo subunits, the absorption spectra of *m*-trisazobenzene and its derivatives were then calculated at the TDDFT/B3LYP level of theory. A series of substituted *m*-trisazobenzenes were evaluated to develop novel multiazobenzene structures for highly efficient and multifunctional molecular photoswitches. Ultimately, an unique substituted MTA containing three independently photoswitching azo subunits was constructed and each azo subunit of the substituted MTA can in principle be switched selectively by appropriate wavelengths of light.

Moreover, cyclotrisazobenzene (CTA), which exhibits a high stability of the trans-isomerzation state, has attracted recent attention [68,70-71] due to its unique macrocyclic strained structure and isomerization properties. An in-depth understanding of the multiphotochromic photoresponsive structure and the isomerization mechanism of macrocyclic azobenzenes is the molecular foundation to exploit new properties for specific azobenzene-based materials. A relaxed scan of the S_1 potential energy surface along the torsion pathway and geometry optimization of the lowest ππ* excited state S_4

of CTA was performed at the TDDFT/BHLYP level of theory. The calculations confirmed an essentially blocked isomerization pathway of the azo subunits due to the strain in CTA. Based on this property, CTA as constrained cyclic molecules can therefore be utilized as UV-absorbers in many potential applications.

Next, to obtain a good comprise between accuracy and the computational effort for excited state calculations, an efficient implementation of the restricted virtual space (RVS) approximation in the algebraic diagrammatic construction (ADC) scheme was presented in Chapter 5. Due to the RVS approximation, the size of the virtual orbital space is reduced due to negligible contributions to the low-lying excited states. In effect, not only a substantial amount of energetically high-lying virtual orbitals but also the core orbitals are restricted for low-lying excited state calculations. RVS-ADC test calculations were performed on several representative organic molecules such as octatetraene, indole, and pyridine using three different standard basis sets of triple-zeta quality, i.e. 6-311G*, cc-pVTZ and def2-TZVP. The results revealed the accuracy and limitations of the applicability of RVS-ADC(2) when only retaining a segment of the total virtual orbital space. Specifically, freezing the core and truncating less than 30% of the high-lying virtual orbitals with 6-31G* basis set and even more than 50% for def2-TZVP and cc-pVTZ basis sets has negligible effects on the low-lying ππ* excited states. However, when the lowest excited states are characterized by nπ* and πσ* states, RVS-ADC(2) is no longer very reliable. By contrast, RVS-ADC for π-Rydberg excited state behaves better than for nπ* or πσ* states. This problematic behavior is probably attributed to orbital relaxation caused by the ignored virtual orbitals, which features different errors for low-lying excited states having different character. Furthermore, test calculations on pyridine at the level of RVS-ADC(3)/def2-TZVP demonstrate that the accuracy of the RVS-ADC(3) approach is greatly improved, since the errors introduced by RVS-ADC(2) are corrected at the higher-order ADC scheme. Using the same number of the virtual orbitals, the accuracy of RVS-ADC excitation energies with the cc-pVTZ basis set is better than with the cc-pVDZ basis set. Using a unified NVT value, the RVS errors with different standard basis sets are quite similar from the accuracy perspective. NVT makes the application of the RVS-ADC scheme

more controllable, regardless of the type of the basis set. The investigation of the RVS approximation in the ADC schemes would be useful to describe low-lying excited states of medium-sized molecules and can provide promising benchmark results for comparison purposes with less computational effort.

In the present work, the unique photochromic properties and isomerizaion behavior of linear multiazobenzenes and non-linear azobenzenes were investigated using TDDFT together with more accurate wavefunction based methods like the ADC method. The performance of RVS-ADC for excitation energies of the lowest excited states was evaluated. However, an important question concerning conical intersections remains to be answered due to the failure of many single-reference quantum chemical methods like TDDFT and ADC. Future work will still focus on the development of a variety of multiple azobenzenes in the design of coupled photoswitches to be applied in various photoresponsive materials. Another interesting perspective involves the interactions between two or even more individual azobenzenes that undergo isomerization simultaneously. Further, the unique optical surface patterning effect occurring in mass azobenzene systems necessitates the research of cooperative isomerization mechanism. Besides, future studies on the RVS-ADC scheme in the calculation of excited state properties like dipole moments, geometries and transition dipole moments are ongoing.

Acknowledgements

First, I am very grateful to my supervisor Prof. Dr. Andreas Dreuw for giving me the opportunity to study interesting research projects. His understanding and constant encouragement always motivated me to complete my studies throughout my reseach period. With his expertise, generous guidance, fruitful discussions and suggestions, I have made great progress not only in my research project but also deeply in my scientific mind. Especially, I am hugely indebted to him for saving me during our canyoning in Kleinwalsertal.

I would like to thank Prof. Dr. Shirin Faraji, who recommended me to Prof. Dr. Andreas Dreuw, for being such a kind mentor and for giving me a lot of advice, not only for my research, but for life. I am also indebted to Dr. Michael Wormit for his steady encouragement and for teaching me useful scientific approaches at the beginning .

I am thankful to Prof. Dr. Josef Wachtveitl and Dr. Chavdar Slavov for the pleasant cooperation on two exciting papers.

I owe a deep sense of gratitude to Prof. Dr. Jochen Schirmer and PD Dr. Markus Pernpointner for helpful and interesting discussions.

I would especially like to express my gratitude to Dr. Tim Stauch and Daniel Lefrancois, who strictly corrected my dissertation and provided me with very useful suggestions.

I want to thank Ellen, Mannfred, Stefan, Max, Michael, Felix and Tobi for their kind help throughout the past four years.

I also take this opportunity to thank all members of the Dreuw Group for giving me an unforgettable experience in Heidelberg.

Finally, I am also grateful to my father, mother, sister and friends, who have always encouraged and supported me to go on and to complete my studies.

Bibliography

1. G. S. Hartley. *Nature,* 1937, 140, 281-281.
2. H. Rau and E. Lueddecke. *J. Am. Chem. Soc.*, 1982,104, 1616-1620.
3. H. Rau. *In Photochromism: Molecular and Systems; ed. H. Durr, H.Bouas-Laur an, Elsevier: Amsterdam,* 1990, pp 165-192.
4. Z. F. Liu, K. Hashimoto, A. Fujishima. *Nature.* 1990, 347, 658-660.
5. Z. Sekkat, M. Dumont. *Appl. Phys. B.* 1992, 54, 486-489.
6. T. Ikeda, O. Tsutsumi. *Science,* 1995, 268, 1873-1875.
7. H. Rau. *Angew. Chem., Int. Ed. Engl.,* 1973, 12, 224-235
8. T. Schultz, J. Quenneville, B. Levine, A. Toniolo, T. J. Martínez, S. Lochbrunner, M. Schmitt, J. P. Shaffer, M. Z. Zgierski, and A. Stolow. *J. Am. Chem. Soc.*, 2003, 125, 8098-8099
9. W. Feng, W. Luo and Y. Feng. *Nanoscale,* 2012, 4, 6118-6134.
10. Y. Wang and H. P. Cheng. *Phys. Rev. B,* 2012, 86, 035444(10).
11. H. Asanuma, T. Ito, T. Yoshida, X. Liang and M. Komiyama, *Angew. Chem., Int. Ed.,* 1999, 38, 2393-2395.
12. A. A. Beharry and G. A. Woolley. *Chem. Soc. Rev.,* 2011, 40, 4422-4437.
13. F. Zhang, A. Zarrine-Afsar, M. S. Al-Abdul-Wahid, R. S. Prosser, A. R. Davidson and G. A. Woolley, *J. Am. Chem. Soc.,* 2009, 131, 2283-2289.
14. C. Renner and L. Moroder, *ChemBioChem,* 2006, 7, 868-878.
15. T. Hugel, N. B. Holland, A. Cattani, L. Moroder, M. Seitz, H. E. Gaub. *Science,* 2002, 296, 1103-1106.
16. H. M. Dhammika Bandara and S. C. Burdette. *Chem. Soc. Rev.,* 2012,41, 1809-1

825.

17. T. Sasaki and J. M. Tour, *Org. Lett.,* 2008, 10, 897-900.

18. J. Shao, Y. Lei, Z. Wen, Y. Dou, Z. Wang. *J. Chem. Phys.* 2008, 129, 164111/1.

19. M. Blanco-Lomas, S. Samanta, P. J. Campos, G. A. Woolley, D. Sampedro. *J. Am. Chem. Soc.* 2012,134, 6960.

20. B. Sapich, A. B. E. Vix, J. P. Rabe, J. Stumpe. *Macromolecules,* 2005, 38, 10480.

21. K. Hunger. *Industrial dyes: Chemistry, Properties, Applications,* Wiley-VCH, Weinheim, Germany, 2003, p 14-35.

22. H. Zollinger, *Color Chemistry: Syntheses, Properties and Applications of Organic Dyes and Pigments,* VCH, NY, 1987, p 85.

23. A. Jain, Y. Gupta and S. K. Jain, Crit. Rev. Ther. *Drug Carrier Syst.*, 2006, 23, 349.

24. T. Fujino, S. Y. Arzhantsev, T. Tahara. *J. Phys. Chem. A,* 2001, 105, 8123-8129.

25. H. Fliegl, A. Kohn, C. Hättig, R. Ahlrichs. *J. Am. Chem. Soc.*, *2003*, *125*, 9821-9827.

26. J.-Å. Anderson, R. Petterson, L. Tegnér. *J. Photochem.,* 1982, 20, 17-32.

27. A. Cembran, F. Bernardi, M. Garavelli, L. Gagliardi, G. Orlandi. *J. Am. Chem. S oc.,* 2004, 126, 3234-3243.

28. I. K. Lednev, T.-Q, Ye, L. C. Abbot, R. E. Hester, J. N. Moore. *J. Phys. Chem. A,* 1998, 102, 9161-9166.

29. T. Ishikawa, T. Noro. *J. Chem. Phys.*, 2001, 115, 7503-7512.

30. I. K. Lednev, T.-Q. Ye, P. Matousek, M. Towrie, P. Foggi, F. V. R. Neuwahl, S. Umpathy, R. E Hester, J. N. Moore. *Chem. Phys. Lett.,* 1998, 290, 68-74.

31. P. Cattaneo, M. Persico. Phys. *Chem. Chem. Phys.*, 1999, 1, 4739-4743.

32. C. R. Crecca and A. E. Roitberg. *J. Phys. Chem. A,* 2006, 110, 8188-8203.

33. S. Monti, G. Orlandi, and P. Palmieri. *Chem. Phys.*, 1982, 71, 87-99.

34. E. W.-G. Diau, *J. Phys. Chem. A*, 2004, 108, 950-956.

35. C.-W. Chang, Y. C. Lu, T. T. Wang, and E. W.-G. Diau. *J. Am. Chem. Soc.*, 2004, 126, 10109-10118.

36. T. Nägele, R. Hoche, W. Zinth, J. Wachtveitl. *J. Chem. Phys. Lett.*, 1997, 272, 489-495.

37. A. Dreuw and M. Head-Gordon. *Chem. Rev.,* 2005, 105, 4009-4027.

38. G. D. Purvis III, R. J. Bartlett. *J.Chem. Phys.*, 1982, 76, 1910-1918.

39. J. F. Stanton, R. J. Bartlett. *J.Chem. Phys.,* 1993, 98, 7029-7039.

40. J. H. Starcke, M. Wormit, J. Schirmer and A. Dreuw. *Chem. Phys.*, 2006, 329, 3 9-49.

41. A. Dreuw, M. Wormit, *WIREs. Comp. Mol. Sci.,* 2015, 5, 82-95.

42. J. Schirmer. *Phys. Rev. A*, 1982, 26, 2395-2416.

43. P. Å. Malmqvist, B.O. Roos, Chem. Phys. Lett., 1989, 155, 189-194.

44. J. Olsen. *Int. J. Quant. Chem*., 2011, 111, 3267-3272.

45. J. Finley, P. A. Malmqvist, B.O. Roos, L. Serrano-Andres. *Chem. Phys. Lett.,* 1998, 288, 299-306

46. G. Ghigo, B. O. Roos and P.-Å. Malmqvist. *Chem. Phys. Lett.,* 2004, 396, 142-149.

47. M.W. Schmidt, M.S. Gordon. *Annu. Rev. Phys. Chem.,* 1998, 49, 233-66.

48. E. Runge and E. K. U. Gross. *Phys. Rev. Lett.,* 1984, 52, 997-1000.

49. M. E. Casida, *Recent Advances in Density Functional Methods* (D. P. Chong, Ed.), World Scientific, Singapore, *1995, Part I, Chap. 5.*

50. L. Gagliardi, G. Orlandi, F. Bernardi, A. Cembran and M. Garavelli. *Theor. Che m. Acc.,* 2004, 111, 363-372.

51. M. L. Tiago, S. I. smail-Beigi, and S. G. Louie. *J. Chem. Phys., 2005, 122, 0943 11-094317.*

52. M. J. Comstock, N. Levy, A. Kirakosian, J. Cho, F. Lauterwasser, J. H. Harvey, D. A. Strubbe, J. M. J. Fréchet, D. Trauner, S. G. Louie, M. F. *Phys. Rev. Lett.,* 2007, 99, 038301.

53. E. Kazuma, M. Han, J. Jung, J. Oh, T. Seki and Y. Kim. *J. Chem. Phys. Lett.,* 2015, 6,4239-4243.

54. Y. Harabuchi, M. Ishii, A. Nakayama, T. Noro, T. Taketsugu. *J. Chem. Phys.,* 2013, 138, 064305.

55. E. M. M. Tan. *et al. Nat. Commun.,* 2015, 6, 5860.

56. S. Bellotto, R. Reuter, C. Heinis, and H. A. Wegner. *J. Org. Chem.,* 2011, 76, 9826-9834.

57. G. Floß and P. Saalfrank, *J. Phys. Chem. A,* 2015, 119, 5026-5037.

58. D. Bléger, J. Dokic´, M. V. Peters, L. Grubert, P. Saalfrank and S. Hecht. *J. Phys. Chem. B,* 2011, 115, 9930-9940.

59. C. Slavov, C. Yang, L. Schweighauser, C. Boumrifak, A. Dreuw, H. A. Wegner and J. Wachtveitl. *Phys. Chem. Chem. Phys.,* 2016, 18, 0 14795-14804.

60. F. Cisnetti, R. Ballardini, A. Credi, M. T. Gandolfi, S. Masiero, F. Negri, S. Pier accini, G. P. Spada. *Chem. Eur. J.* 2004, 10, 2011-2021.

61. J. Robertus, S. F. Reker, T. C. Pijper, A. Deuzeman, W. R. Browne, B. L. Fering a. *Phy s. Chem. Chem. Phys.* 2012, 14, 4374-4382.

62. N. B. Holland, T. Hugel, G. Neuert, A. Cattani-Scholz, C. Renner, D. Oesterhelt, L. Moroder, M. Seitz and H. E. Gaub. *Macromolecules,* 2003, 36, 2015-2023.

63. D. Bléger, Z. Yu and S. Hecht. *Chem. Commun.,* 2011, 47 12260-12266.

64. Z. Yu and S. Hecht, *Angew. Chem., Int. Ed.*, 2011, 50, 1640-1643.

65. M. R. Han and M. Hara. *New J. Chem.*, 2006, 30, 223-227.

66. D. Jacquemin, E. A. Perp`te, G. Scalmani, I. Ciofini, C. Peltier and C. Adamo. *C hem. Phys.,* 2010, 372, 61-66.

67. S. Iamsaard, S. J. Aßhoff, B. Matt, T. Kudernac, J. J. L. M. Cornelissen, S. P. Fletcher and N. Katsonis. *Nat. Chem.,* 2014, 6, 229-235.

68. R. Reuter and H. A. Wegner. *Chem. Commun.,* 2013, 49, 146-148.

69. M. Baroncini, S. d'Agostino, G. Bergamini, P. Ceroni, A. Comotti, P. Sozzani, I. Bassanetti, F. Grepioni, T. M. Hernandez, S. Silvi, M. Venturi and A. Credi. *Nat. Chem.,* 2015, 7, 634-640.

70. R. Reuter, N. Hostettler, M. Neuburger and H. A. Wegner. *Eur. J. Org. Chem.*, 2009, 2009, 5647-5652.

71. R. Reuter, N. Hostettler, M. Neuburger and H. A. Wegner, *CHIMIA Int. J. Chem.,* 2010, 64, 180-183.

72. E. Titov, G. Granucci, J. P. Götze, M. Persico, and P. Saalfrank, *J. Phys. Chem. Lett.*, 2016, 7, 3591-3596.

73. T. G. Gopakumar, T. Davran-Candan, J. Bahrenburg, R. J. Maurer, F. Temps, K. Reuter and R. Berndt. *Angew. Chem. Int. Ed*. 2013, 52, 11007-11010

74. K. Scheil, T. G. Gopakumar, J. Bahrenburg, F. Temps, R. J. Maurer, K. Reuter, and R. Berndt. *J. Phys. Chem. Lett.*, 2016, 7, 2080-2084

75. Y. Lim, S. Choi, K. B. Park and C. -G Cho. *J. Org. Chem.,* 2004, 69, 2603-2606.

76. M. Müri, K. C. Schuermann, L. De Cola and M. Mayor. *Eur. J. Org. Chem.,* 2009, 2562-2575.

77. Á. Moneo, ; G. C. Justino, M. F. N. N. Carvalho, M. C. Oliveira, A. M. M. Antunes, D. Bléger, S. Hecht, and J. P. Telo. *J. Phys. Chem. A,* 2013, 117, 14056-14064.

78. O. A. Blackburn, B. J. Coe. and M. Helliwell. *Organometallics,* 2011, 30, 4910-4923.

79. H. Koshima, N. Ojima, H. Uchimoto, *J. Am. Chem. Soc.,* 2009, 131, 6890-6891.

80. Y. L. Yu, M. Nakano, T. Ikeda. *Nature,* 2003, 425, 145.

81. N. Hosono, T. Kajitani, T. Fukushima, K. Ito, S. Sasaki, M. Takata, T. Aida. *Science*, 2010, 330, 808-811.

82. L. Schweighauser, D. Häussinger, M. Neuburger and H. A. Wegner. *Org. Biomol. Chem.,* 2014, 12, 3371-3379.

83. E. Durgun and J. C. Grossman, *J. Phys. Chem. Lett.,* 2013, 4, 854-860.

84. C. Hättig, F. Weigend. *J. Chem. Phys.*, 2000, 113, 5154-5161.

85. M. Head-Gordon; R. J. Rico, M. Oumi, T. J. Lee. *Chem. Phys. Lett.*, 1994, 219, 21-29.

86. H. Larse, K. Hald, J, Olsen and P. Jorgensen, *J. Chem. Phys.,* 2001, 115, 3015-3020.

87. H. Sekino, R. J. Bartlett. *Int. J. Quant. Chem. Symp.,* 1984 , 18 , 255-265.

88. J. F. Stanton, R. J. Bartlett. *J. Chem. Phys.* 1993, 98, 7029-7039.

89. H. J. Werner, P. J. Knowles. *J. Chem. Phys.* 1988, 89, 5803-5814.

90. P. J. Knowles and H. J. Werner. *Theo. Chim. Acta.* 1992, 84, 95.

91. A. B. Trofimov, J. Schirmer. *J. Phys. B. At. Mol. Opt. Phys.,* 1995, 28, 2299-2324.

92. A. B. Trofimov, G. Stelter, J. Schirmer. *J. Chem. Phys.,* 1999, 111,9982-9999.

93. J. H. Starcke, M. Wormit, A. Dreuw. *J. Chem. Phys.,* 2009, 130, 024104.

94. S. Knippenberg, P. Eisenbrandt, L. Šištík, P. Slavíˇcek, A. Dreuw. *Chem. Phys. Chem.,* 2011, 12, 3180-3191.

95. J. Liu and W. Liang. *J. Chem. Phys.,* 2011, 135, 014113.

96. J. Liu and W. Liang. *J. Chem. Phys.,* 2011, 135, 184111.

97. J. Liu and W. Liang. *J. Chem. Phys.,* 2013, 138, 024101.

98. J. B. Foresman, M. Head-Gordon, J. A. Pople, and M. J. Frisch. *J. Phys. Chem.* 1992, 96, 135-149.

99. R. Reuter, N. Hostettler, M. Neuburger, and H. A. Wegner. *Eur. J. Org. Chem.,* 2009, 32, 5647-5652.

100. M. Olivucci. *Computational Photochemistry.* Elsevier: Amsterdam, 2005, Vol . 16.

101. F. Jensen. Introduction to Computational Chemistry, 2nd Edition, *John Wiley & Sons. 2007.*

102. A. Szabo and N. S. Ostlund. *Modern Quantum Chemistry.* Mineola, New York: Dover Publications, 1996.

103. C. J. Cramer. *Essentials of Computational Chemistry*, John Wiley & Sons, Lt d, 2004.

104. R. K. Nesbet. *Proc. R. Soc. A,* 1955, 230, 312-321.

105. P.-O. Löwdin. Adv. *Chem. Phys.* 1959, 2, 207-322.

106. L. H. Thomas. *Math. Proc.,* Cambridge 1927, 23, 542-548.

107. E. Fermi. *Atti Accad. Naz. Lincei.,* 1927, 6, 602-607.

108. P. A. M. Dirac. *Math. Proc.* Cambridge 1930, 26, 376-385.

109. J. C. Slater. *Phys. Rev.,* 1951, 81, 385-390.

110. P. Hohenberg. W. Kohn. *Phys. Rev.,* 1964, 136, B864-B871.

111. W. Kohn, L. J Sham. *Phys. Rev.,* 140, A1133-A1138.

112. E. Schrödinger. *Phys. Rev.,* 1926, 28, 1049-1070.

113. M. Born, R. Oppenheimer. *Ann. Phys.,* 1927, 389, 457-484.

114. C. Møller, M. S. Plesset. *Phys. Rev.,* 1934, 46, 618-622.

115. R. J. Bartlett and and M. Musial. *Rev. Mod. Phys*., 2007, 79, 291-352.

116. F. A. Berazin. *The Method of Second Quantization.* Academic Press: New York, 1966.

117. S. J. Gustafson, I. M. Sigal. *In Mathematical Concepts of Quantum Mechanics.* Springer Berlin Heidelberg: Berlin, Heidelberg, 2011, p 209-226.

118. Wormit, M. Development and Application of Reliable Methods for the Calculation of Excited States: From Light-Harvesting Complexes to Medium-Sized Molecules. Ph.D. Thesis, Johann Wolfgang Goethe-Universität, January 2009.

119. T. Helgaker, P. Jørgensen and J. Olsen. *Molecular Electronic-Structure Theory.* John Wiley & Sons Ltd, Chichester, West Sussex, 2000.

120. Ritz, W. J. Reine. *Angew. Math.* 1909, 135, 1-61.

121. Ramana, B. V. *Higher Engineering Mathematics*. Tata McGraw-Hill: New Delhi, 2008.

122. R. J. Harrison and N. C. Handy. *Chem. Phys. Lett.,* 1983, 95, 386

123. J. B. Foresman, M. Head-Gordon, J. A. Pople, M. J. Frisch. *J. Phys. Chem.,* 1992, 96, 135-149.

124. J. E. Del Bene, R. Ditchfield, and J. A. Pople. *J. Chem. Phys.* 1971, 55, 2236.

125. M. Head-Gordon, D. Maurice, and M. Oumi. *Chem. Phys. Lett.,* 1995, 246, 114.

126. R. J. Bartlett. *Ann. Rev. Phys. Chem.,* 1981, 32, 359-401.

127. R. J. Bartlett. *Wiley Interdisciplinary Reviews: Computational Molecular Science*, 2012, 2, 126-138.

128. J. D. Watts, J. Gauss and R. J. Bartlett. *J. Chem. Phys.*, 1993, 98, 8718-8733.

129. O. Christiansen, H. Koch, P. Jørgensen. *Chem. Phys. Lett.,* 1995, 243, 409-418.

130. A.Hellweg, S. A. Grün, C. Hättig. *Phys. Chem. Chem. Phys.,* 2008, 10, 4119-4127.

131. O. Christiansen, A. Halkier, H. Koch, P. Jørgensen, T. Helgaker. *J. Chem. Phys.,* 1998, 108, 2801-2816.

132. O. Christiansen, J. Gauss, J. F. Stanton, P. Jørgensen. *J. Chem. Phys.,* 1999, 111, 525-537.

133. J. Schirmer and A. B. Trofimov. *J. Chem. Phys.*, 2004, 120,11449-11464.

134. F. Mertins and J. Schirmer. *Phys. Rev. A,* 1996, 53, 2140-2152.

135. G. C. Wick. *Phys. Rev.,* 1950, 80, 268-272.

136. A. D. Becke. *J. Chem. Phys.*, 2014,140, 8A301.

137. R. G. Parr and W. Yang. *Density-functional theory of atoms and molecules.* Oxford Science Publication, New York, 1989.

138. J. P. Perdew, K. Burke, Y. Wang. *Phys. Rev.B,* 1996, 54, 16533.

139. A. D. Becke, *Phys. Rev. A,* 1988, 38, 3098-3100.

140. A. D. Becke. *J. Chem. Phys.*, 1993, 98, 5648-5652.

141. A. D. Becke. *J. Chem. Phys.*, 1993, 98, 1372-1377.

142. P. Elliott, K. Burke, F. Furche. *Reviews in Computational Chemistry.* Eds. K. B. Lipkoitz and T. R. Cundari, Wiley, Hoboken, 2009, 26.

143. K. Yabana, G. F. Bertsch. *Phys. Rev. B,* 1996, 54, 4484-4487.

144. M. A. L. Marques, A. Castro, G. F. Bertsch, A. Rubio. *Comput. Phys. Commun.,* 2003, 151, 60.

145. F. Furche. *J. Chem. Phys.* 2001, 114, 5982.

146. M. E. Casida and M. Huix-Rotllant. *Ann. Rev. Phys. Chem.*, 2012, 63, 287-323.

147. S. Hirata, M. Head-Gordon. *Chem. Phys. Lett.,* 1999, 314, 291-299.

148. C. Lee, W. Yang and R. G. Parr. *Phys. Rew. B, 1988, 37, 785-789.*

149. *A.* Görling. *Phys. Rev. Lett.,* 1999, 83, 5459.

150. S. Ivanov, S. Hirata, R. J. Bartlett. *Phys. Rev. Lett.,* 1999, 83, 5455.

151. A. Dreuw, J. L. Weisman and M. Head-Gordon. *J. Chem. Phys.,* 2003, 119, 2943-2946.

152. Z.-L. Cai, K. Sendt and J. R. Reimers. *J. Chem. Phys.,* 2002, 117, 5543-5549.

153. R. J. Magyar, S. Tretiak. *J. Chem. Theo. Comput.,* 2007, 3, 976-987.

154. C. Reichardt. *Solvents and Solvent Effects in Organic Chemistry.* 2nd ed. Wiley- VCH: Weinheim, 1988.

155. J. Tomasi, B. Mennucci, R. Cammi. *Chem. Rev.,* 2005, 105, 2999-3093

156. V. Barone and M. Cossi. *J. Phys. Chem. A,* 1998, 102, 1995-2001.

157. M. Cossi, N. Rega, G. Scalmani, V. Barone. *J. Comput. Chem.,* 2003, 24, 669-681.

158. R. A. Friesner, ; V. Guallar, V. *Annu. Rev. Phys. Chem.,* 2005, 56, 389-427.

159. H. Lin, D. G.Truhlar. *Theor. Chem. Acc.,* 2007, 117, 185-99.

160. C. J. Cramer, D. G. Truhlar. *Chem. Rev.,* 1999, 99, 2161-2200.

161. J. Tomasi, M. Persico. *Chem. Rev.,* 1994, 94, 2027-2094.

162. J. Li, T. Zhu, C. J. Cramer, D. G. Truhlar. *J. Phys. Chem. A,* 2000, 104, 2178-2182.

163. B. Mennucci, *WIREs Comput. Mol. Sci.,* 2012, 2, 386-404.

164. D. M. Dolney, G. D. Hawkins, P. Winget, D. A. Liotard, C. J. Cramer, D. G.

Truhlar. *J. Comput. Chem.,* 2000, 21, 340-366.

165. S. Miertuŝ, E. Scrocco, J. Tomasi. *Chem. Phys.,* 1981, 55, 117-129.

166. A. Klamt. G. Schüü rmann. *J. Chem. Soc., Perkin Trans. 2,* 1993, 799-805.

167. A. Klamt. *WIREs Comput. Mol. Sci.,* 2011, 1, 699-709.

168. S. Miertuŝ, J. Tomasi. *Chem. Phys.,* 1982, 65, 239-245.

169. M. Cossi, V. Barone, R. Cammi, J. Tomasi. *Chem. Phys. Lett.,* 1996, 255, 327-335.

170. V. Barone, M. Cossi, J. Tomasi. *J. Chem. Phys.,* 1997, 107, 3210-3221.

171. B. Mennucci, J. Tomasi. *J. Chem. Phys.,* 1997, 106, 5151-5158.

172. R. Cammi, B. Mennucci, J. Tomasi. *J. Phys. Chem. A,* 2000, 104, 5631-5637.

173. M. Cossi,V. Barone. *J. Chem. Phys.,* 2000, 112, 2427-2435.

174. M. Cossi,V. Barone. *J. Chem. Phys.,* 2001, 115, 4708-4717.

175. M. Cossi, G. Scalmani, N. Rega, V. Barone. *J. Chem. Phys.,* 2002, 117, 43-54.

176. F. Neese. *The ORCA Program System*. *Wiley Interdiscip. Rev.:Comput. Mol. Sci.,* 2012, 2, 73-78.

177. Y. Shao, *et al. Mol. Phys.,* 2015, 113, 184-215.

178. N. Tamai, H. Miyasaka. *Chem Rev.,* 2000, 100, 1875-1890.

179. D. Jacquemin, *et al. Int*. *J*. *Quant*. *Chem.*, 2011, 111, 4224-4240.

180. I. K. Lednev, T. Q. Ye, R. E. Hester, J. N. Moore. *J. Phys. Chem.*, 1996, 100, 13338-13341

181. J. Liu, Z.-R. Chen, and S.-F. Yuan. *J. Zhejiang. Univ. Sci. B,* 2005, 6, 584-589.

182. H. Sekino and R. J. Bartlett. *J. Chem. Phys.*, 1986, 85, 976-989.

183. S. P. Karna, M. Dupuis, E. Perrin and P. N. Prasad. *J. Chem. Phys.*, 1990, 92, 7418-7425.

184. S. Hirata, M Head-Gordon and R. J. Bartlett. *J. Chem. Phys.,* 1999, 111, 10774-10786.

185. W. J. Hehre, R. Ditchfield and J. A. Pople. *J. Chem. Phys.,* 1972, 56, 2257-2261.

186. R. Krishnan, J. S. Binkley, R.Seeger, J. A. Pople. *J. Chem. Phys.*, 1980, 72, 650-654.

187. P. J. Stephens, F. J. Devlin, C. F. Chabalowski and M. J. Frisch. *J. Phys. Chem.,* 1994, 98, 11623-11627.

188. M. Kasha, H. R. Rawls and M. A. El-Bayoumi. *Pure Appl. Chem.*, 1965, 11, 3 71-392.

189. T. Cusati, G. Granucci, M. Persico and G. Spighi. *J. Chem. Phys.,* 2008, 128, 194312.

190. M. Utecht, T. Klamroth and P. Saalfrank. *Phys. Chem. Chem. Phys.,* 2011, 13, 21608-21614.

191. C. Gahl, R. Schmidt, D. Brete, E. R. McNellis, W. Freyer, R. Carley, K. Reuter, and M. Weinelt. *J. Am. Chem. Soc.*, 2010, 132, 1831-1838.

192. P. Bortolus and S. Monti, *J. Phys. Chem.*, 1979, 83, 648-652.

193. D. J. Willock. *Molecular Symmetry.* John Wiley and Sons, Ltd: West Sussex, 2009.

194. P.W. Atkins, J. de Paula. *Physical Chemistry.* 9th ed, *Oxford University Press.* 2010.

195. F. Plasser, S. A.Bäppler, M. Wormit and A. Dreuw. *J. Chem. Phys.,* 2014, 141, 024107.

196. F. Plasser, M. Wormit and A. Dreuw. *J. Chem. Phys.,* 2014, 141, 024106.

197. T. D. Bouman and A. E. Hansen. *Int. J. Quantum Chem. Symp*., 1989, 23, 381.

198. A. E. Hansen, B. Voight, and S. Rettrup. *Int. J. Quantum Chem.,* 1983, 23, 595.

199. R. Reuter, H. A. Wegner. *Org. Lett.* 2011, 13, 5908-5911.

200. R. Reuter, H. A. Wegner. *Chem. Eur. J.* 2011, 17, 2987-2995.

201. E. Merino. *Chem. Soc. Rev.,* 2011, 40, 3835-3853

202. V. Botan, *et al. Proc. Natl. Acad. Sci.,* 2007, 104, 12749-12754.

203. H. M. Muller-Werkmeister and J. Bredenbeck. *Phys. Chem. Chem. Phys.*, 2014, 16, 3261-3266.

204. S. Buchenberg, D. M. Leitner and G. Stock. *J. Phys. Chem. Lett.*, 2016, 7, 25-30.

205. C. Slavov, C. Yang, L. Schweighauser, H. A. Wegner, A. Dreuw, and J. Wachtveitl. *Chem. Commun.,* 2017, Submission for publication.

206. T. Yanai, D. P. Tew, N. C. Handy. *Chem. Phys.Lett.,* 2004, 393, 51-57.

207. H. Koch, J. J. Aa. Jensen, P. Jørgensen, T. Helgaker. *J. Chem. Phys.,* 1990, 93, 3345.

208. W. Möller, C. Nager and P. Rosmus. *Chem. Phys.,* 1980, 51, 43-48

209. U. Wahlgren and L. Pettersson. *Chem. Phys.,* 1982, 69, 185.

210. M. Pelissier and E. R. Davidson. *Int. J. Quant. Chem.,* 1984, 25, 483-491.

211. M. Hada, H. Yokono, and H. Nakatsuji. *Chem. Phys. Lett.*, 1987, 141, 339-345.

212. C. Sosa, J. Geertsen, G.W. Trucks, R.J. Bartlett and J. A. Franz. *Chem. Phys. Lett.,* 1989, 159,148-154.

213. K. K. Baeck , J. D. Watts, R. J. Bartlett. *J. Chem. Phys.,* 1997, 107, 3853 .

214. R.B. Murphy, D.M. Philipp, R.A. Friesner. *Chem. Phys. Lett.,* 2000, 321, 113.

215. Plasser et al. *Angew. Chem.-Int. Ed*, 2013, 52, 2581.

216. K. K. Baeck and S.Il Jeon. *Bull. Korean Chem. Soc.,* 2000, 21, 720.

217. A. I. Krylov, C. D. Sherrill, E. F. C. Byrd, and M. Head-Gordo. *J. Chem. Phys.,* 1998, 109, 10668.

218. A. I. Krylov, C. D. Sherrill, M. Head-Gordon. *J. Chem. Phys.* 2000, 113,6052 .

219. H. Nakai, H. Morita, P. Tomasello, H. Nakatsuji. *J. Phys. Chem. A,* 2003, 102, 2033.

220. R. Send, V. R. I. Kaila, D. Sundholm, *J. Chem. Phys.,* 2011. 134, 214114.

221. R. Send, C. M. Suomivuori, V. R. I. Kaila, D. Sundholm. *J. Phys. Chem. B,* 2015, 119, 2933-2945.

222. A. P. Gamiz-Hernandez, I. N. Angelova, R. Send, D. Sundholm, V. R. I. Kaila. *Angew. Chem. Int. Ed.* 2015, 54, 11564-11566.

223. L. Adamowicz and R. J. Bartlettand. *J. Chem. Phys.,* 1987, 86, 6314.

224. L. Adamowicz, R. J. Bartlett and A. J. Sadlej. *J. Chem. Phys.,* 1988, 88, 5749.

225. A. G. Taube and R. J. Bartlett. *Collect. Czech. Chem. Commun*., 2005, 70, 837-850.

226. A. G. Taube and R. J. Bartlett. *J. Chem. Phys.,* 2008, 128, 164101.

227. M. Sulka, M. Pitonak, P. Neogrady, M. Urban. *Int. J. Quant. Chem.,* 2008, 108, 2159.

228. L. Adamowicz. *Mol.Phys.,* 2010, 108, 3105-3112.

229. M. Sulka, M. Pitonak, I. Cernusak, M. Urban, P. Neogrady. *Int. J. Quant. Chem.,* 2012, 112, 948.

230. D. Feller and E.R. Davidson, *J. Chem. Phys.,* 1981, 74, 3977.

231. F. Aquilante, T. K. Todorova, L. Gagliardi, T. B. Pedersen, B. O. Roos. *J. Chem. Phys.,* 2009, 131, 034113

232. A . Landau, K. Khistyaev, S. Dolgikh, A. I. Krylov. *J. Chem. Phys.,* 2010, 132, 014109.

233. A. E. DePrince III and C. D. Sherrill. *J. Chem. Theo. Comput.*, 2013, 9, 293-299.

234. J. Wenzel, M. Wormit, A. Dreuw. *J. Comp. Chem.,* 2014, 35, 1900-1915.

235. M. Wormit, D. R. Rehn, P. H. P. Harbach, J. Wenzel, C. M. Krauter, E. Epifanovsky, A. Dreuw. *Mol. Phys.*, 2014, 112, 774-784.

236. J. Wenzel, A. Holzer, M. Wormit and A. Dreuw. *J. Chem. Phys.,* 2015, 142, 214104.

237. P. H. P. Harbach, M. Wormit and A. Dreuw. *J. Chem. Phys.,* 2014, 141, 064113

238. C. Hättig. *Adv. Quant. Chem.,* 2005, 50, 37.

239. S. Knippenberg, D. R. Rehn, M. Wormit, J. H. Starcke, I. L. Rusakova, A. B. Trofimov, A. Dreuw, *J. Chem. Phys.,* 2012, 136, 064107.

240. A. B. Trofimov, I. L. Krivdina, J. Weller, J. Schirmer. *Chem. Phys.,* 2006, 328, 1-10.

241. I. L. Krivdina, L. B. Krivdin, Y. Y. Rusakov, A. B. Trofimov. *J. Chem. Phys.,* 2012, 137, 044119.

242. T. H. Dunning. *J. Chem. Phys.,* 1989, 90, 1007.

243. R. A. Kendall, Jr., T. H. Dunning, and R. J. Harrison. *J. Chem. Phys.,* 1992, 96, 6796.

244. W. J. Hehre, R. Ditchfield, and J. A. Pople. *J. Chem. Phys.,* 1972, 56, 2257.

245. R. Krishnan, J. S. Binkley, R. Seeger, and J. A. Pople. *J. Chem. Phys.,* 1980,

72, 650.

246. F. Weigend, F. Furche, and R. Ahlrichs. *J. Chem. Phys.*, 2003, 119, 12753.

247. F. Weigend and R. Ahlrichs. *Phys. Chem. Chem. Phys.*, 2005, 7, 3297.

248. F. Weigend. *Phys. Chem. Chem. Phys.*, 2006, 8,1057-1065.

249. F. Weigend, A. Köhn, C. Hättig. *J. Chem. Phys.,* 2002, 116, 3175-3183.

List of Tables

List of Figures

Eidesstattliche Versicherung gemäß §8 der Promotionsordnung der Naturwissenschaftlich-Mathematischen Gesamtfakultät der Universität Heidelberg

1. Bei der eingereichten Dissertation zu dem Thema

   "**Quantum Chemical Study of coupled molecular photoswitches**"

   handelt es sich um meine eigenständig erbrachte Leistung.

2. Ich habe nur die angegebenen Quellen und Hilfsmittel benutzt und mich keiner unzulässigen Hilfe Dritter bedient. Insbesondere habe ich wörtlich oder sinngemäß aus anderen Werken u bernommene Inhalte als solche kenntlich gemacht.

3. Die Arbeit oder Teile davon habe ich bislang nicht an einer Hochschule des In- oder Auslands als Bestandteil einer Prüfungs- oder Qualifikationsleistung vorgelegt.

4. Die Richtigkeit der vorstehenden Erklärungen bestätige ich.

5. Die Bedeutung der eidesstattlichen Versicherung und die strafrechtlichen Folgen einer unrichtigen oder unvollständigen eidesstattlichen Versicherung sind mir bekannt.

Ich versichere an Eides statt, dass ich nach bestem Wissen die reine Wahrheit erklärt und nichts verschwiegen habe.

Ort/Datum Unterschrift